



Universiteit  
Leiden  
The Netherlands

**Magnetism and magnetization dynamics in thin film ferromagnets**  
Verhagen, T.G.A.

**Citation**

Verhagen, T. G. A. (2014, February 26). *Magnetism and magnetization dynamics in thin film ferromagnets*. *Casimir PhD Series*. Retrieved from <https://hdl.handle.net/1887/24306>

Version: Not Applicable (or Unknown)

License: [Leiden University Non-exclusive license](#)

Downloaded from: <https://hdl.handle.net/1887/24306>

**Note:** To cite this publication please use the final published version (if applicable).

Cover Page



Universiteit Leiden



The handle <http://hdl.handle.net/1887/24306> holds various files of this Leiden University dissertation

**Author:** Verhagen, T.G.A.

**Title:** Magnetism and magnetization dynamics in thin film ferromagnets

**Issue Date:** 2014-02-26

**Magnetism and magnetization dynamics  
in thin film ferromagnets**



# **Magnetism and magnetization dynamics in thin film ferromagnets**

Proefschrift

ter verkrijging van  
de graad van Doctor aan de Universiteit Leiden,  
op gezag van Rector Magnificus prof. mr. C.J.J.M. Stolker,  
volgens besluit van het College voor Promoties  
te verdedigen op woensdag 26 februari 2014  
klokke 15.00 uur

door

Timotheus Guillaume Albertus Verhagen

geboren te Roosendaal en Nispen  
in 1985

Promotiecommissie:

Promotores:	prof. dr. J. Aarts	Universiteit Leiden
	prof. dr. J. M. van Ruitenbeek	Universiteit Leiden
Overige leden:	prof. dr. G. E. W. Bauer	Technische Universiteit Delft & Tohoku University
	prof. dr. E. H. Brück	Technische Universiteit Delft
	dr. T. Pietsch	Universität Konstanz
	prof. dr. E. R. Eliel	Universiteit Leiden
	prof. dr. E. J. J. Groenen	Universiteit Leiden
	prof. dr. ir. T. H. Oosterkamp	Universiteit Leiden
	dr. M. J. A. de Dood	Universiteit Leiden

©2014 Tim Verhagen, 

This work is licensed under a

Creative Commons Attribution – NonCommercial – ShareAlike 3.0

Unported license. Visit [http://creativecommons.org/licenses/by-](http://creativecommons.org/licenses/by-sa/3.0/)

[sa/3.0/](http://creativecommons.org/licenses/by-sa/3.0/) to view a copy of this license.

ISBN: 978-90-8593-177-5

Casimir PhD series, Leiden-Delft 2013 – 37

Printed by Proefschriftmaken.nl

An electronic version of this dissertation is available at

<https://openaccess.leidenuniv.nl>







# Contents

<b>Contents</b>	<b>vii</b>
<b>1 Radiation &amp; Spins</b>	<b>1</b>
1.1 Light-emitting diodes . . . . .	2
1.2 Semiconductor laser . . . . .	5
1.3 THz gap . . . . .	6
1.4 Spintronics . . . . .	6
1.5 Outlook . . . . .	6
<b>2 Theory</b>	<b>9</b>
2.1 Magnetism . . . . .	10
2.2 Spin current . . . . .	12
2.3 Ferromagnetic heterostructures . . . . .	13
2.4 Magnetization dynamics . . . . .	16
2.5 Spin-flip laser . . . . .	24
<b>3 Point contact spectroscopy</b>	<b>29</b>
3.1 Point contact spectroscopy - theoretical . . . . .	29
3.2 Point contact spectroscopy - experimental . . . . .	32
3.3 Spin-flip laser . . . . .	36
3.4 Discussion . . . . .	39
3.5 Outlook . . . . .	41
<b>4 Sm-Co thin films</b>	<b>43</b>
4.1 Sm-Co based magnetic materials . . . . .	43
4.2 Experiment . . . . .	49
4.3 Magnetic properties of Sm-Co thin films grown on MgO(100) deposited from a single alloy target . . . . .	51
4.4 Sm-Co thin films grown by cosputtering Sm and Co . . . . .	64

<b>5</b>	<b>Temperature dependence of the Gilbert damping in thin Co/Pt bilayers</b>	<b>75</b>
5.1	Introduction . . . . .	75
5.2	Ferromagnetic resonance in thin magnetic films . . . . .	76
5.3	Damping in thin magnetic films . . . . .	80
5.4	Experimental . . . . .	86
5.5	FMR measurements . . . . .	88
5.6	Spin pumping detected by the inverse spin Hall effect . . . . .	92
5.7	Low temperature electrical characterisation . . . . .	99
5.8	Low temperature spin pumping . . . . .	99
5.9	Discussion . . . . .	104
5.10	Summary . . . . .	110
<b>6</b>	<b>Spin-orbit torque in SiO<sub>x</sub>/Co/Cu bilayers</b>	<b>111</b>
6.1	Experiment . . . . .	113
6.2	Results . . . . .	113
6.3	$\delta$ -doping with magnetic impurities . . . . .	118
6.4	Evaluation of the FMR measurements . . . . .	121
6.5	Electric manipulation of the magnetization precession using the SHE . . . . .	123
6.6	Substrate . . . . .	123
6.7	Discussion . . . . .	125
<b>A</b>	<b>Hall measurements</b>	<b>129</b>
A.1	Discussion . . . . .	132
	<b>Bibliography</b>	<b>135</b>
	<b>Summary</b>	<b>147</b>
	<b>Samenvatting</b>	<b>151</b>
	<b>Curriculum Vitae</b>	<b>155</b>
	<b>Publications</b>	<b>157</b>
	<b>Acknowledgments</b>	<b>159</b>

# Radiation & Spins

From the end of the 19th century, the light bulb that was (re-)invented by many scientist during the 19th century, started slowly to replace the traditional lightning where fossil fuels, oil, fat and wood where burnt. The light that a light bulb generates is controlled by the temperature of the filament inside the bulb. The intensity  $I$  of the emitted radiation at a wavelength  $\lambda$  can be described by Planck's law

$$I(\lambda, T) = \frac{2\pi hc^2}{\lambda^5} \frac{1}{\exp\left(\frac{hc}{\lambda kT}\right) - 1}, \quad (1.1)$$

where  $T$  is the temperature of the blackbody,  $h$  is Plancks constant,  $c$  is the speed of light and  $k$  is Boltzmann's constant. In Figure 1.1, the intensity of the emission of a black body with a temperature of 2800 K, a 60 W incandescent light bulb and a white light emitting diode (LED) are shown. Clearly visible is that the maximum intensity of the spectrum is at approximately 1000 nm and only a small fraction (approximately 10 %) of the intensity is emitted at the visible spectrum (390 - 700 nm). To increase the efficiency of a light bulb, a much higher temperature is needed.

During the introduction of the light bulbs, also the first observations of what we now know as a light emitting diode (LED) were reported [2].

Round, one of Marconi's assistants, in 1907 published a short note in 'Electrical world' [3] (see Figure 1.2.a) where he described a 'bright glow' from a SiC crystal. In 1928, Losev published the current-voltage

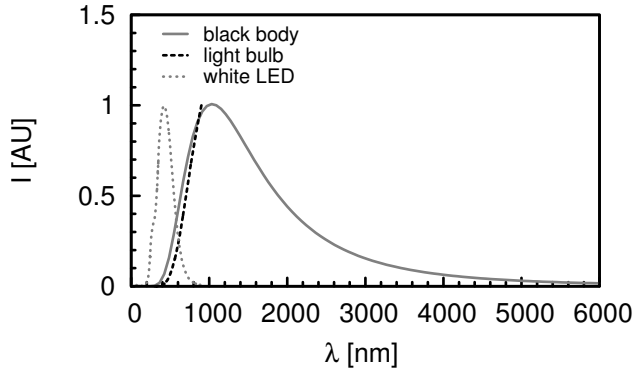
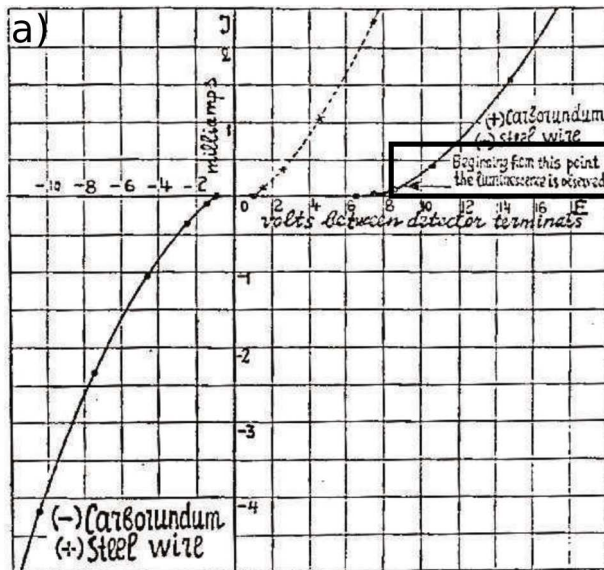


Figure 1.1: Emission spectra of an incandescent light bulb (Airam, long-life 60 W, 2800 K [1]), a white LED (Hewlett Packard HLMP-CW31 [1]) and a black body at 2800 K.

characteristic of SiC and also observed light emission, as is indicated in the current-voltage characteristic in Figure 1.2.b [4]. Unfortunately, this research was forgotten. In 1962, four research groups published papers where they showed a LED laser based on electron-hole recombination in the direct semiconductors GaAs [5–7] and GaAsP [8].

## 1.1 Light-emitting diodes

Depending on the type of the semiconductor, the electron-hole recombination can happen in a direct or indirect transition. In an direct band gap semiconductor (see Figure 1.3.a) the momentum of the electrons in the conduction band and the holes in the valence band is the same, whereas in a indirect band gap semiconductor (see Figure 1.3.b) these momenta are not the same. When an electron-hole recombination happens, the momentum and energy need to be conserved. In a direct band gap semiconductor, the momentum is conserved and the energy is conserved by emitting a photon with the energy equal to the band gap. In an indirect semiconductor, a photon can also be emitted if the momentum is conserved by the creation or annihilation of a phonon. However, in an indirect semiconductor these radiative recombinations are only a very small fraction of the total amount of recombinations.



b) A Note on Carborundum.

To the Editors of *Electrical World*:

STKS:—During an investigation of the unsymmetrical passage of current through a contact of carborundum and other substances a curious phenomenon was noted. On applying a potential of 10 volts between two points on a crystal of carborundum, the crystal gave out a yellowish light. Only one or two specimens could be found which gave a bright glow on such a low voltage, but with 110 volts a large number could be found to glow. In some crystals only edges gave the light and others gave instead of a yellow light green, orange or blue. In all cases tested the glow appears to come from the negative pole, a bright blue-green spark appearing at the positive pole. In a single crystal, if contact is made near the center with the negative pole, and the positive pole is put in contact at any other place, only one section of the crystal will glow and that the same section wherever the positive pole is placed.

There seems to be some connection between the above effect and the e.m.f. produced by a junction of carborundum and another conductor when heated by a direct or alternating current; but the connection may be only secondary as an obvious explanation of the e.m.f. effect is the thermoelectric one. The writer would be glad of references to any published account of an investigation of this or any allied phenomena.

NEW YORK, N. Y.

H. J. ROUND.

Figure 1.2: a) The current-voltage characteristics of a carborundum (SiC) detector. The arrow (in the black rectangle) indicates the voltage where light emission was observed. b) A note from 1907 from the Marconi lab, mentioning that a curious phenomenon happens when 10 V was applied between two points on a carborundum crystal: the emission of a yellowish light. Images adapted by permission from Macmillan Publishers Ltd [2], © (2007).

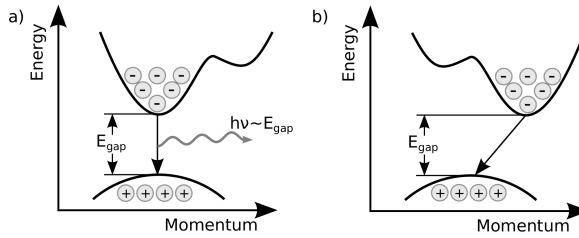


Figure 1.3: The energy of a direct (a) and an indirect (b) band gap semiconductor as a function of the momentum. In a direct band gap semiconductor, an electron can be moved from the lowest state in the conduction band to the highest state in the valence band without a change in momentum. The energy is conserved by the emission of a photon with the energy of the band gap. In an indirect band gap semiconductor, also a change in momentum is needed to move between the lowest state of the conduction band and the highest state of the valence band.

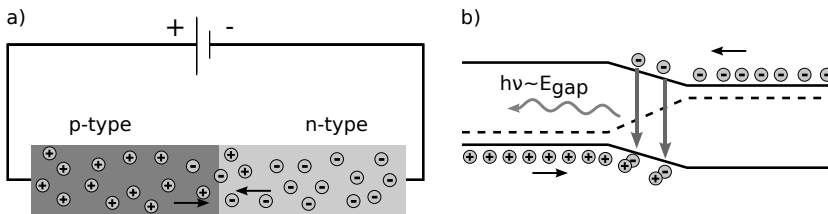


Figure 1.4: a) A p-n junction with an applied bias. When the p-n junction is forward biased (b), electrons from the n-doped region and holes from the p-doped region flow to the depletion layer, where the electrons and holes will recombine and emit a photon. Adapted from [9].

Furthermore, the conductivity of a semiconductor can be modified to create an excess of electrons (becoming an n-type semiconductor) or a deficiency of electrons (becoming a p-type semiconductor) by various techniques (for example doping or gating).

In a forward biased p-n junction (see Figure 1.4), electrons from the n-doped region flow in the p-doped region and holes from the p-doped region flow into the n-doped region. Within a characteristic diffusion length from the depletion layer, the carriers recombine. If this process happens in a direct semiconductor, the electron in the conduction band will fall into the valence band and emits a photon to conserve energy.

When the p-n junction is very heavily doped, the bottom of the n-

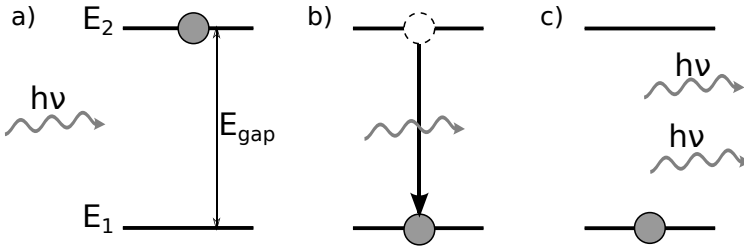


Figure 1.5: a) An electron is in the excited state  $E_2$  and can relax to the ground state by emitting a photon. This relaxation can be induced by another photon (b), which results in two coherent photons (c). Adapted from [10].

side conduction band overlaps the top of the p-side valence band. Applying a forward bias cancels the thermal equilibrium potential difference causing the injecting of electrons from the conduction band on the n-side into the conduction band on the p-side. The injection from electrons into the conduction band on the p-side creates a situation where there are more electrons in the conduction band than in the valence band; a population inversion.

## 1.2 Semiconductor laser

An electron in the excited state will finally relax to the ground state by emitting a photon. If this happens in the absence of any external field, this is called a spontaneous emission, where the generated photons are non-coherent.

However, the relaxation can also be induced by a photon, as is shown in Figure 1.5. This process is called stimulated emission and the emitted photons are coherent. Whenever more electrons are in the excited state than in the ground state, one incident photon can trigger an avalanche of photons: light amplification by stimulated emission or laser. This avalanche continues as long as the population inversion can be maintained. Typically frequencies of the emitted radiation are of the order of the bandgap, which is typically 1 – 5 eV. This corresponds to 250 – 1250 THz.

### 1.3 THz gap

The electromagnetic frequency range used nowadays is large, from the Hertz via the kilohertz, megahertz, gigahertz up to the terahertz. Semiconductor devices are enabling components for almost the whole frequency range. For the low frequency range, semiconductor transistors and other devices based on electron transport produce the radiation, whereas semiconductor lasers generate coherent light at very high frequencies.

As shown in Figure 1.6, there is no continuous transition from the low frequency to the high frequency region and between these two regimes lies the so-called THz gap. On the one hand, transistors and other devices based on electron transport are limited to about 300 GHz. On the other hand, the wavelength of semiconductor lasers can be extended down to only 30 THz. In the lab, many different THz sources are explored, that are shown as ovals in Figure 1.6. Unfortunately, most of these devices work well at (very) low temperatures, but at room temperature the output power reduces considerably.

### 1.4 Spintronics

During the last 30 years, another property of the electron became more and more popular in electronics: the spin. Spin transport electronics, or spintronics, can nowadays be found in many electronic devices. In particular, spintronics found its way in data storage and manipulation devices such as the read/write head of a harddisk, magnetoresistive random-access memory (MRAM) and spin-transfer torque random-access memory (STT-RAM). The wish to increase the speed, the storage capacity and decrease the power consumption leads to a constant flow of new spintronic phenomena like the spin transfer torque [12, 13], spin-orbit torques [14] ('Spin-Orbitronics'), the spin Hall effect [15], the spin Seebeck effect [16] and 'plasmonic spintronics' [17].

### 1.5 Outlook

In 2004 Kadigrobov [18, 19] proposed the idea that electromagnetic radiation might be created when a LED and the spin of the electron are combined: a spin-flip laser. In a spin-flip laser, a photon is created when a spin-flip process takes place in a normal metal or ferromagnet. A very promising feature of the spin-flip laser is the prediction that the laser emits light in the terahertz range. In **Chapter 2**, an introduction



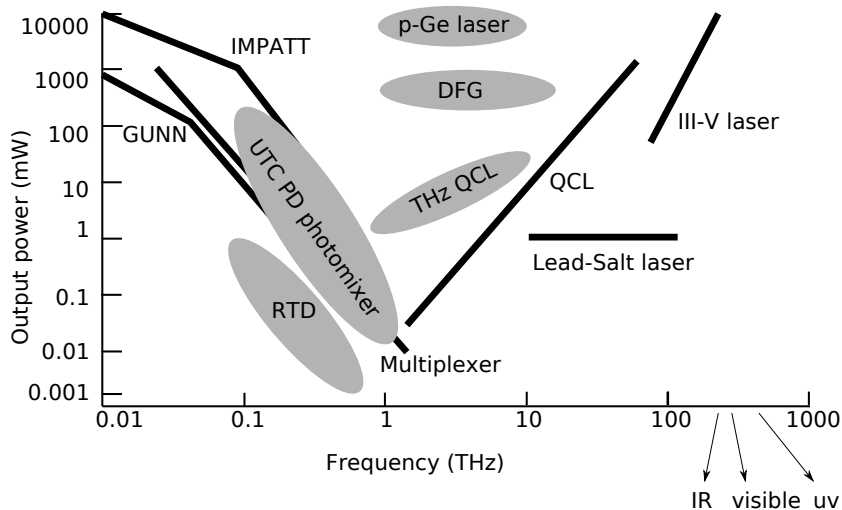


Figure 1.6: THz ( $10^{12}$  Hz) emission power as a function of frequency. The solid lines indicate conventional THz sources; IMPATT stands for impact ionization avalanche transit-time diode, multiplexer is a Schottky barrier diode frequency multiplier, QCL is a quantum cascade laser and III-V laser is a semiconductor laser diode. The ovals denote recent THz sources, where RTD stands for resonant tunnelling diodes, UTC-PD photomixer stands for uni-travelling-carrier photodiode photomixer and DFG stands for difference-frequency generation. Images adapted by permission from Macmillan Publishers Ltd [11], © (2007).

to spintronics is given, which will lead to the introduction of the spin-flip laser. One way to build and characterize a spin-flip laser is via the point contact spectroscopy technique. In **Chapter 3**, this technique will be introduced and we will discuss the possibilities and limitations of this approach. Another requirement for spin-flip lasers are hard magnetic materials. **Chapter 4** describes the growth and characterization of thin films of the hard ferromagnet Sm-Co.

In **Chapter 5**, we study how the transport of spin happens at a ferromagnet/normal metal interface using ferromagnetic resonance and the spin pumping technique. Especially, we are interested in the low temperature behaviour of spin currents flowing from the ferromagnet into the normal metal. In **Chapter 6** we show what happens with the magnetization dynamics of a very thin ferromagnetic layer that has asymmetric interfaces.

# Theory

Many physical phenomena in condensed matter physics, such as the Hall effect and the quantized conductance, can be explained well considering electrons as spinless particles with a charge  $-e$ . However, there are effects that cannot be described without taking the spin of the electron into account, such as magnetism [20, 21], the Kondo effect [22] and the spin Hall effect [23].

Spin is the intrinsic angular momentum of an electron, which is characterized with the spin quantum number  $s$ , which is  $\frac{1}{2}$  for an electron. The spin angular momentum operator  $\mathbf{S}$  is given by

$$\mathbf{S} = \frac{1}{2}\hbar\boldsymbol{\sigma}, \quad (2.1)$$

where  $\hbar$  is the reduced Planck constant and  $\boldsymbol{\sigma}$  are the Pauli spin matrices

$$\sigma_x = \begin{pmatrix} 0 & 1 \\ 1 & 0 \end{pmatrix}, \quad \sigma_y = \begin{pmatrix} 0 & -i \\ i & 0 \end{pmatrix}, \quad \sigma_z = \begin{pmatrix} 1 & 0 \\ 0 & -1 \end{pmatrix}. \quad (2.2)$$

In particular, when the spin is pointing along the z-axis, the corresponding eigenstates are  $|\uparrow\rangle = \begin{pmatrix} 1 \\ 0 \end{pmatrix}$  and  $|\downarrow\rangle = \begin{pmatrix} 0 \\ 1 \end{pmatrix}$  and the spin points either parallel (spin-up) or antiparallel (spin-down) to the z-axis.

The electron spin also possesses a magnetic moment  $\boldsymbol{\mu}_s$

$$\boldsymbol{\mu}_s = -\frac{g\mu_B}{\hbar}\mathbf{S}, \quad (2.3)$$

where  $g$  is the g-factor equalling 2 for a free electron and  $\mu_B$  is the Bohr magneton.

## 2.1 Magnetism

Magnetic properties are closely related to the electronic structure of the solid. Three different forms of magnetic states can be distinguished: diamagnetic, paramagnetic and magnetically ordered systems (e.g. ferromagnets or antiferromagnets) [20, 21]. While a (weak) diamagnetic contribution to the total magnetic susceptibility is present in all materials, paramagnetism or magnetic ordering can be observed only in materials with incomplete electron shells.

### Diamagnetism

In a diamagnet, the action of an external magnetic field on the electrons moving in the orbitals induces a magnetic moment, which opposes the applied magnetic field (Lenz's law). Another contribution, Landau diamagnetism, originates from the Lorentz force acting on conduction electrons, which is, however, overshadowed by stronger Pauli paramagnetic contribution. Diamagnetism is in general a very weak phenomenon.

### Paramagnetism

In atoms (ions) with incomplete atomic shells, the magnetic moment  $\mu$  is proportional to the total angular momentum  $\mathbf{L} + \mathbf{S}$ . Without an applied magnetic field, the magnetic moments point in a random direction if the interaction between the moments is negligible. In that case, the magnetic susceptibility  $\chi$  is strongly temperature dependent and follows the Curie law  $\chi = C/T$ .

In itinerant electron systems, the state of the electrons can be described as a non-interacting gas of free electrons characterized by the momentum  $\mathbf{k}$  and the spin  $\sigma$  of the valence electrons. When a magnetic field  $H$  is applied, the electron band is split into two spin subbands, where the energy of an electron is raised or lowered by  $\frac{1}{2}g\mu_B H$  depending on the orientation of the spin, as is shown in Figure 2.1.a. The Pauli magnetic susceptibility  $\chi_P$  of this non-interacting gas of free electrons is then equal to [24]

$$\chi_P = \frac{M}{H} = 2\mu_B^2 N(E_F), \quad (2.4)$$

with  $M$  is the magnetization and  $N(E_F)$  the density of states (DOS) at the Fermi energy.

## Magnetically ordered systems - ferromagnetism

When the interaction between the moments is strong enough, the material exhibits magnetic ordering below a characteristic temperature, the Curie temperature  $T_C$  in ferromagnets or the Néel temperature  $T_N$  in antiferromagnets. In ferromagnets, the exchange interactions lead to parallel ordering of magnetic moments giving rise to non-zero magnetization already in zero magnetic field.

In the Stoner model for itinerant ferromagnets, the exchange interaction is treated in simplified form as a molecular field term with the Stoner exchange factor  $I$  as a measure for the interaction. All the spins feel an identical exchange field, which causes a splitting of the electron band into two spin subbands. The energy of the  $n = n_\uparrow + n_\downarrow$  electrons is raised or lowered by  $I \frac{n_\uparrow(\downarrow)}{n}$ .

In the new state, the kinetic energy is increased as electrons originally occupying states with  $k < k_F$  now occupy states with  $k > k_F$ . The increase in kinetic energy is compensated by a decrease in the Coulomb energy, as more spins are aligned and the total spatial overlap of electron states is reduced.

The susceptibility  $\chi$  is then equal to

$$\chi_s = \frac{2\mu_B^2 N(E_F)}{1 - IN(E_F)}, \quad (2.5)$$

with  $I$  the Stoner exchange factor. When  $IN(E_F)$  becomes larger than one, the susceptibility becomes negative, indicating that the interacting electron gas forms a spontaneous moment. For the transition metals, the Stoner exchange constants  $I$  are of comparable order (approximately 1 eV) and the transition to a ferromagnetic state depends mostly on the density of states at the Fermi energy. This implicates that narrow bands at the Fermi energy are needed that can give rise to a large DOS.

In a ferromagnetic material, the total energy is built up from (short range) exchange interactions and (long range) dipole fields, including shape and demagnetization effects. It is therefore usually energetically favourable to form magnetic domains to keep the magnetization inside the material and minimize the demagnetization fields. Each domain has a single orientation of the magnetization vector. In the absence of a magnetic field, the magnetization of a ferromagnet is close to zero.

With an increasing magnetic field, the amount of domains with a magnetization that is aligned with the applied field increases. When

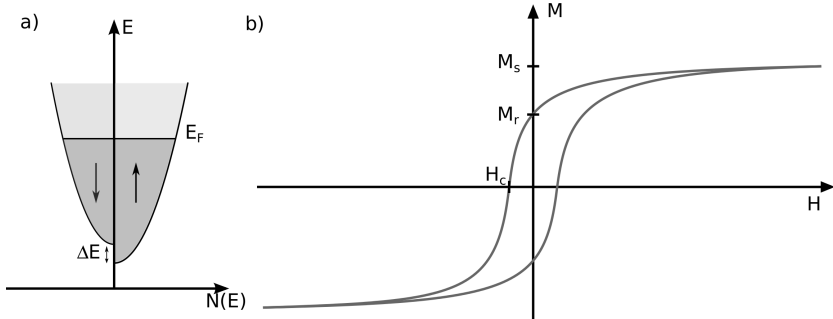


Figure 2.1: a) Density of states of an itinerant electron gas showing the splitting of the energy bands. b) The magnetization hysteresis loop for a ferromagnet. The saturation magnetization  $M_s$  is the maximum magnetization that can be obtained when all the magnetic moments are aligned, while the remanence or remanent magnetization  $M_r$  shows the magnetization of a ferromagnet when no external field is applied. The coercive field  $H_c$  is the opposite field needed to obtain zero magnetization.

the magnetization of all domains is aligned in the same direction, the maximum magnetization of the material is obtained: the saturation magnetization  $M_s$ . When the magnetic field is decreased to zero, the magnetization direction of the domains are not aligned all in the same direction and the remaining magnetization without an applied magnetic field is called the remanence or remanent magnetization  $M_r$ . The opposite magnetic field needed to drive the magnetization to zero is the coercive field  $H_c$ . Figure 2.1.b. shows an example of a magnetization hysteresis loop. Such a loop shows the magnetization of a ferromagnet as a function of an applied field.

## 2.2 Spin current

A key ingredient to describe spin transport properties are spin currents. A charge current  $\mathbf{I}_c$  and spin current  $\mathbf{I}_s$  are described as [25, 26]

$$\mathbf{I}_c = e \sum_{\mathbf{k}} \mathbf{v}_{\mathbf{k}\uparrow} f_{\mathbf{k}\uparrow} + \mathbf{v}_{\mathbf{k}\downarrow} f_{\mathbf{k}\downarrow}, \quad \mathbf{I}_s = e \sum_{\mathbf{k}} \mathbf{v}_{\mathbf{k}\uparrow} f_{\mathbf{k}\uparrow} - \mathbf{v}_{\mathbf{k}\downarrow} f_{\mathbf{k}\downarrow}, \quad (2.6)$$

where  $\mathbf{v}_{\mathbf{k}\sigma}$  is the velocity of an electron with momentum  $\mathbf{k}$  and spin  $\sigma$  and  $f_{\mathbf{k}\sigma}$  is the distribution function for electrons with momentum  $\mathbf{k}$  and spin  $\sigma$ .

The distribution function  $f_{\mathbf{k}\sigma}$  can be calculated using the Boltzmann transport equation [25, 26]

$$\mathbf{v}_{\mathbf{k}} \cdot \frac{f_{\mathbf{k}\sigma}}{\partial \mathbf{r}} + \frac{e}{\hbar} \mathbf{E} \cdot \frac{f_{\mathbf{k}\sigma}}{\partial \mathbf{k}} = \left( \frac{\partial f_{\mathbf{k}\sigma}}{\partial t} \right)_{\text{scattering}}, \quad (2.7)$$

where  $\mathbf{E}$  is an external electric field. In many situations, the external fields produce only a small change  $g_{\mathbf{k}\sigma}$  in the equilibrium distribution function  $f_{\mathbf{k}\sigma}^0$ . The scattering term can then be rewritten using the relaxation time approximation [25] as

$$\left( \frac{\partial f_{\mathbf{k}\sigma}}{\partial t} \right)_{\text{scattering}} = -\frac{g_{\mathbf{k}\sigma}}{\tau_{\sigma}} - \frac{f_{\mathbf{k}\sigma} - f_{\mathbf{k}-\sigma}}{\tau_{\text{sf}}}, \quad (2.8)$$

where  $\tau_{\sigma}$  is the relaxation time for electrons with spin  $\sigma$  and  $\tau_{\text{sf}}$  is the spin-flip time, that defines the time between two elastic collisions or two spin-flip collisions, respectively. The distance an electron ballistically travels between two collisions is the electron mean free path  $\ell$ , which is equal to  $\ell = v_F \tau_{\sigma}$ , with  $v_F$  the Fermi velocity and the distance an electron ballistically travels between spin-flips is the spin-flip length  $\ell_{\text{sf}}$ , which is equal to  $\ell_{\text{sf}} = v_F \tau_{\text{sf}}$ . A third length scale is the spin diffusion length  $\ell_{\text{SD}} = \sqrt{D \tau_{\text{sf}}}$ , with  $D$  the diffusion constant. The spin diffusion length is the distance the electron diffuses through the material between spin-flip collisions [27].

Using equation 2.6, three different types of current can be distinguished. When  $\mathbf{v}_{\mathbf{k}\uparrow} f_{\mathbf{k}\uparrow} = \mathbf{v}_{\mathbf{k}\downarrow} f_{\mathbf{k}\downarrow}$ , there is a pure charge current and no spin current is present. When  $\mathbf{v}_{\mathbf{k}\uparrow} f_{\mathbf{k}\uparrow} = -\mathbf{v}_{\mathbf{k}\downarrow} f_{\mathbf{k}\downarrow}$ , there exists a pure spin current and no charge current. In other cases, a spin polarized current with polarization  $P$  is present. The creation and the control of pure spin currents is a very attractive feature of spintronics, as it was argued by Murakami et al. [28] that pure spin currents have even time-reversal-symmetry. So, when time is reversed, both the direction of the current and spin are reversed and the spin current remains unchanged. In theory, devices can be constructed which carry pure and dissipationless spin currents, and which could thus overcome the major bottleneck when scaling down normal silicon based technology: heating.

## 2.3 Ferromagnetic heterostructures

During the last 30 years, the number of studies of heterostructures of ferromagnets (F) with normal metals (N), semiconductors (Sc) and superconductors (S) has grown impressively. Due to the discovery of

the Giant Magnetoresistance (GMR) effect at the end of the eighties by Baibich et al. [29] and Binasch et al. [30], the study between ferromagnets and normal metals became an area of intense fundamental and applied research. Nowadays the GMR effect is used in many products, ranging from magnetic sensors to magnetoresistive random-access memories (MRAM).

The GMR effect appears in thin films composed of alternating ferromagnetic and non-magnetic layers. The relative orientation of the magnetization direction of the ferromagnetic layers determines the resistance in the multilayer. Figure 2.2 shows a ferromagnet ( $F_1$ )/normal metal (N)/ferromagnet ( $F_2$ ) trilayer, where the coercive field  $H_{c1}$  of layer  $F_1$  is larger than the coercive field  $H_{c2}$  of layer  $F_2$ . A current that flows through layer  $F_1$  becomes spin polarized. When the thickness of the N layer is smaller than the spin diffusion length, the spin polarized current will reach layer  $F_2$ . For simplicity, we assume that both layers are 100% spin polarized and all the electrons are either transmitted or reflected at the interface of layer  $F_2$ . When the magnetization of layer  $F_2$  is parallel to  $F_1$ , all electrons can be transmitted (Figure 2.2.a) through  $F_2$  and a current will flow through the trilayer. When the magnetization of layer  $F_2$  is antiparallel to layer  $F_1$ , all electrons are reflected off  $F_2$  (Figure 2.2.b) and no current will flow through the trilayer. The resulting resistance as a function of the applied external field  $H$ , the magnetoresistance, is plotted in Figure 2.2.c. The fixed  $F_1$  layer and free  $F_2$  layer behave different to the applied external magnetic field and the magnetization direction switches at a different applied field,  $H_{c1}$  and  $H_{c2}$  respectively.

The transport properties through GMR devices with ferromagnets with spin polarization  $P$  and where both ferromagnetic layers have a collinear magnetization, where the magnetization is aligned with the spin quantization axis, can be described using the two-channel series resistor model that was introduced by Valet and Fert [31]. In the Valet-Fert model, the total current is modelled as two individual currents for the spin-up and spin-down channel, limited by a channel dependent resistances that represent the bulk and interface scattering.

The attraction of the interaction between ferromagnets and normal metals lies in the fact that already at room temperature large effects can be observed. Theoretically, they can be explained well using the framework of static magneto-electronic circuit theory [32]. This theory describes the charge and spin transport in multilayers by dividing the device in a circuit with reservoirs, resistors and nodes. An important contribution here comes from the interface. For a collinear magnetization, the spin dependent interface conductance,  $G^{\uparrow(\downarrow)}$ , is given by the



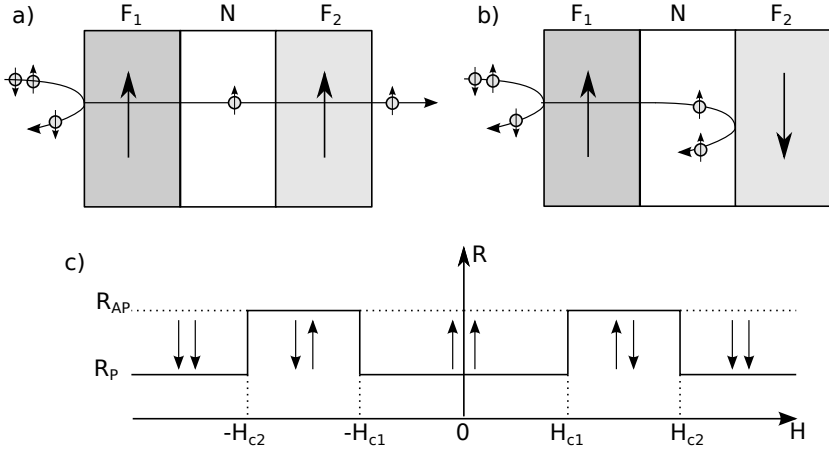


Figure 2.2: Giant magnetoresistance in a ferromagnet ( $F_1$ )/normal metal (N)/ferromagnet ( $F_2$ ) trilayer. The incoming unpolarized electrons from the left side are polarized by the  $F_1$  layer. Depending on the orientation of the magnetization of the  $F_2$  layer with respect to  $F_1$ , the electrons are either fully transmitted (a) or reflected (b). In (c), the resistance of the  $F_1$ /N/ $F_2$  trilayer is shown as a function of the applied field  $H$ . The magnetization direction of the  $F_1$  and  $F_2$ -layer switches at different applied field ( $H_{c1}$  and  $H_{c2}$ ). A higher resistance,  $R_{AP}$ , occurs when the magnetization in the ferromagnetic layers is in the antiparallel ( $\uparrow\downarrow$  or  $\downarrow\uparrow$ ) state and a lower resistance,  $R_P$ , occurs when the magnetization in  $F_1$  and  $F_2$  is in a parallel ( $\uparrow\uparrow$  or  $\downarrow\downarrow$ ) state.

Landauer-Büttiker formula in a two-spin channel model and is equal to

$$G^{\uparrow(\downarrow)} = \frac{e^2}{h} \sum_{nm} \left| t_{nm}^{\uparrow(\downarrow)} \right|^2, \quad (2.9)$$

where  $\left| t_{nm}^{\uparrow(\downarrow)} \right|^2$  is the probability that a spin-up (spin-down) electron in mode  $n$  is transmitted at the interface as a spin-up (spin-down) electron in mode  $m$ . For transport between non-collinear ferromagnets, also the spin-mixing conductance  $G^{\uparrow\downarrow}$  should be taken into account [33]. It is equal to

$$G^{\uparrow\downarrow} = \frac{e^2}{h} \left[ M - \sum_{nm} r_{nm}^{\uparrow} (r_{nm}^{\downarrow})^* \right], \quad (2.10)$$

where  $M$  is the total number of transport channels and  $r_{nm}^{\uparrow(\downarrow)}$  are the reflection coefficients between transport channels  $n$  and  $m$ . The spin-mixing conductance is a complex quantity, where the product  $r_{nm}^{\uparrow} (r_{nm}^{\downarrow})^*$  describes the angle between the incoming spin-up electron and reflected spin-down electron at a normal metal/ferromagnet interface [34].

## 2.4 Magnetization dynamics

A shift from studying the static to the dynamical properties of ferromagnetic-normal metal multilayers was initiated by Berger [12] and Slonczewski [13] in 1996, who proposed that electric currents can induce a reorientation of the magnetization direction in multilayer structures, by the spin transfer torque (STT) mechanism. Already two years later, Tsoi et al. [35] demonstrated that when injecting a very high current density, order of  $10^{12}$  A/m<sup>2</sup>, using a point contact into (Co/Cu)<sub>N</sub> multilayers, magnetization precession can be induced. In 1999, Myers et al. [36] showed that when injecting a very high current density via a lithographic point contact into a Co/Cu/Co multilayer, the orientation of a magnetic domain in the Co layer can be switched. The subsequent discovery of Kiselev et al. [37] that the STT leads to a persistent oscillation at the gigahertz range in a Cu/Co/Cu/Co/Cu/Pt nanopillar opened the field of high frequency detection and manipulation of dynamical STT effects.

### 2.4.1 Landau-Lifshitz-Gilbert equation of motion

In ferromagnets, the magnetic moments are coupled via the exchange interaction. Therefore, the whole spin system with magnetization  $\mathbf{M}$  can be considered as one macrospin. The dynamics of this macrospin is usually described by the phenomenological Landau-Lifshitz-Gilbert (LLG) equation of motion [38–41]

$$\frac{d\mathbf{m}}{dt} = -\gamma \mathbf{m} \times \mathbf{H}_{\text{eff}} + \alpha \mathbf{m} \times \frac{d\mathbf{m}}{dt} + \boldsymbol{\tau}, \quad (2.11)$$

where  $\mathbf{m} = \frac{\mathbf{M}}{|\mathbf{M}|}$  is the unit direction vector of the magnetization  $\mathbf{M}$ ,  $\gamma$  the gyromagnetic ratio, which is defined as  $\gamma = g\mu_B/\hbar > 0$ ,  $\mathbf{H}_{\text{eff}}$  is the local effective magnetic field including the external, demagnetization and crystal anisotropy fields,  $\alpha$  the dimensionless Gilbert damping, with a typical intrinsic value of  $\alpha_0 \approx 10^{-3} - 10^{-2}$  for transition-metal ferromagnets [42] and  $\boldsymbol{\tau}$  accounts for the extra torques present in the system that are induced due to either current and/or spin orbit effects.

The parameter  $\alpha$  is sometimes also encountered as the Gilbert parameter  $G = \alpha\gamma M_s$ . Note that, since  $\mathbf{m}$  is a unit direction vector, the LLG equation describes transverse magnetization dynamics. The first term on the right side of equation 2.11 describes how the magnetization precesses around the local effective field  $\mathbf{H}_{\text{eff}}$  at the Larmor frequency  $\omega_L = \gamma\mathbf{H}_{\text{eff}}$ . The second term describes how the magnetization spirals down on a time scale  $(\alpha\omega)^{-1}$  to this local effective field.

## 2.4.2 Spin-transfer torque

A more general description for the GMR effect described in section 2.3 takes into account that the magnetization direction of both magnetic layers does not need to be collinear. In Figure 2.3.a, a  $F_1/N/F_2$  trilayer is shown where the angle between the magnetization of the  $F_2$  and  $F_1$  layer is equal to  $\theta$  and the magnetization in  $F_2$  is aligned with the spin quantization axis. The resistance is used to monitor the orientation of the magnetization between the two ferromagnetic layers of the trilayer.

When an electron flows through layer  $F_1$ , where the magnetization is not aligned with the spin quantization axis, the state of the electron is a superposition of the spin-up  $|\uparrow\rangle$  and spin-down  $|\downarrow\rangle$  state. The  $|\uparrow\rangle$ -state can cross the interface between N and  $F_2$  and the  $|\downarrow\rangle$  state is reflected. Comparing the angular momentum of the electron before and after the scattering process shows that angular momentum is absorbed by the magnetization of the ferromagnet  $F_2$  within the transverse magnetic coherence length [43]

$$\lambda_c = \frac{\pi}{|k_{\uparrow}^F - k_{\downarrow}^F|}, \quad (2.12)$$

where  $k_{\uparrow(\downarrow)}^F$  are the spin-up and spin-down Fermi wave vectors. In the transition metal ferromagnets Co, Fe and Ni, the transverse magnetic coherence length is in the order of a few Ångström (a tenth of a nm).

A non-collinear spin current can be decomposed in three polarization components: parallel to the magnetization; perpendicular to the magnetization and spin-current,  $\mathbf{I}_s \times \mathbf{M}$ , the so-called field-like torque  $\tau_{\text{FLT}}$ ; or parallel to the spin-current,  $\mathbf{M} \times (\mathbf{I}_s \times \mathbf{M})$ , the spin-transfer torque  $\tau_{\text{STT}}$ . The total torque  $\boldsymbol{\tau}$  that acts on the magnetization is then [32]

$$\begin{aligned} \boldsymbol{\tau} &= \tau_{\text{STT}} + \tau_{\text{FLT}} \\ &= -\frac{\hbar}{e}\text{Re}(G^{\uparrow\downarrow})\mathbf{m} \times (\boldsymbol{\mu} \times \mathbf{m}) - \frac{\hbar}{e}\text{Im}(G^{\uparrow\downarrow})\boldsymbol{\mu} \times \mathbf{m}, \end{aligned} \quad (2.13)$$

with  $\boldsymbol{\mu}$  the total spin-accumulation in the adjacent normal metal. It should be no surprise that both  $\tau_{\text{STT}}$  and  $\tau_{\text{FLT}}$  are determined by the

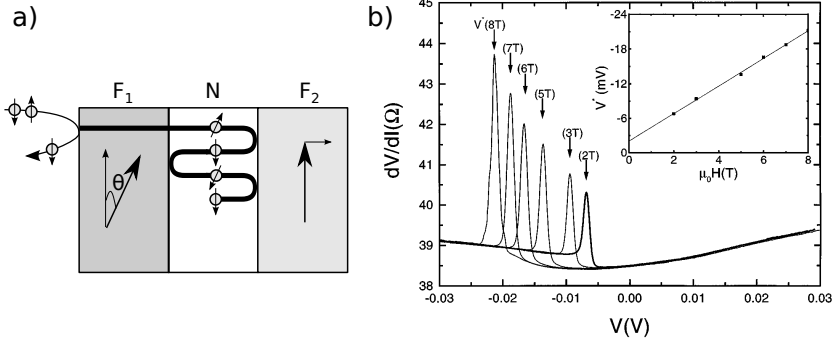


Figure 2.3: a) Spin transfer torque in a  $F_1/N/F_2$  trilayer. The angle between the magnetization direction of layers  $F_1$  and  $F_2$  is equal to  $\theta$ . The right moving electrons are polarized in the  $F_1$  layer and will exert a torque on the magnetization in  $F_2$ . The reflected electron, whose polarization is antiparallel to  $F_2$ , will exert a torque on  $F_1$ . During each reflection, the electron exerts a torque on either  $F_1$  or  $F_2$ , but the influence of higher order scatterings is small as the electron flux decreases with each scattering. b) Differential resistance as a function of the voltage bias for a mechanical point contact to a  $(\text{Co}/\text{Cu})_N$  multilayer, for different out-of-plane applied magnetic fields. The peaks in the differential resistance indicate the onset of the STT. The inset shows that the threshold current is a linear function of the applied magnetic field. Figure b) adapted from [35].

interface spin mixing parameter  $G^{\uparrow\downarrow}$ , given the smallness of the transverse coherence length  $\lambda_c$ .

For metallic systems, the STT is the dominant torque, as  $\text{Re}(G^{\uparrow\downarrow}) \gg \text{Im}(G^{\uparrow\downarrow})$  [44], and the field-like torque can be disregarded in many practical situations.

The change in magnetization due to the transfer of angular momentum of only one spin is very small, but when the current density  $J_c > 10^{10} \text{ A/m}^2$ , the induced STT becomes of the same order as the magnetization.

In Figure 2.4, trajectories are plotted of the magnetization  $M$  in a free magnetic layer without anisotropies, that are a solution of the Landau-Lifshitz-Gilbert equation of motion. As shown in Figure 2.4.a, without damping and spin-transfer torque, the magnetization precesses in a circle due to the torque of the applied magnetic field. If there is also damping present in the system, after the magnetization is perturbed away

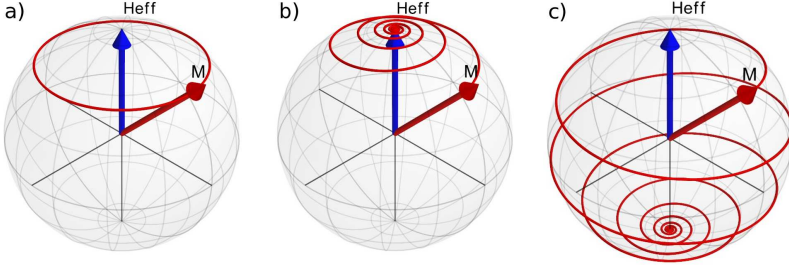


Figure 2.4: Precession of the magnetization in a free magnetic layer without anisotropy. In a), no Gilbert damping and STT is present and the magnetization precesses in a constant trajectory. When damping is introduced, the magnetization precesses slowly back until it is aligned with  $H_{\text{eff}}$  as shown in b). In c) a large STT is introduced that can switch the magnetization. Images adapted from [45]

from the equilibrium state, it will slowly spiral back until the magnetization is aligned with the local effective magnetic field as is shown in Figure 2.4.b. For a spin polarized current below some critical current, the STT acting on the magnetization is not large enough to change the magnetization direction. After the magnetization is perturbed, the magnetization will spiral back, until it is aligned with the local effective magnetic field. When the spin polarized current is larger than the critical current, the STT is large enough to change the magnetization direction and the magnetization spirals away to an equilibrium situation where the damping and the STT are in equilibrium, or the STT can even switch the magnetization direction as shown in Figure 2.4.c.

### 2.4.3 Spin-orbit torque

When an electron with momentum  $\mathbf{k}$  is orbiting the nucleus, in the laboratory frame at rest it feels an electric field  $\mathbf{E}$  from the nucleus. This electric field gives rise to a magnetic field  $\mathbf{B}$  in the reference frame of the electron [46]. This magnetic field interacts with the spin of the electron and gives rise to the spin-orbit Hamiltonian  $\mathcal{H}_{\text{SO}}$

$$\mathcal{H}_{\text{SO}} = -\frac{\hbar}{4m^2c^2} \boldsymbol{\sigma} \cdot (\hbar\mathbf{k} \times \nabla\tilde{V}), \quad (2.14)$$

where  $m$  is the electron mass,  $c$  is the speed of light and  $\tilde{V}$  is the total potential. The total potential consist of a periodic crystal potential and a

potential due to local impurities, confinement, boundaries and external electrical fields [47].

Recently, van der Bijl and Duine [48] showed using linear-response matrix theory that when also the spin-orbit coupling is taken into account, a whole zoo of new current induced torques appear. As with the field-like-torque and the spin-transfer torque, these torques appear in pairs and have the form  $\boldsymbol{\tau}^\perp = \mathbf{m} \times \boldsymbol{\tau}$ . Some of these torques can be attributed to known physical effects like the inhomogeneous magnetization, the anisotropic magnetoresistance and the anomalous or spin Hall effect, but not all derived torques have a straightforward physical interpretation.

Spin-orbit torques can also be related to either structure inversion or bulk inversion asymmetry of the underlying structure, resulting in a Rashba or a Dresselhaus spin-orbit coupling, respectively. Well known systems where such a lack of bulk inversion symmetry can be found are semiconductors with the zinc blende structure such as (Ga,Mn)As [49–51] or crystals from the B20 space group such as FeGe [52] and MnSi [53] which shows a chiral spin-orbit interaction.

Recently, experiments and theory indicated that also in ultrathin metallic multilayers, Rashba spin-orbit coupling might be present. A static electric field  $\mathbf{E} = E_0 e_z$  in the laboratory rest frame, where  $e_z$  points normal to the surface of the multilayers, produces a magnetic field  $\mathbf{B} \propto k_x e_y - k_y e_x$  in the frame of the moving object, where  $k_x e_y - k_y e_x$  is known as the Rashba spin-orbit coupling.

Experimentally, there is not yet agreement about the observations of a Rashba spin-orbit torque, that was measured by Miron et al. [14] and follow up experiments [54, 55]. In these experiments, magnetization switching of a very thin ferromagnetic layer is studied, driven by the current through the layer in the presence of spin-orbit torques. In all studies performed to date, the ferromagnetic layer has either been asymmetrically sandwiched between a heavy metal layer and an oxide layer, e.g. Pt/Co/AlO<sub>x</sub> or Ta/CoFeB/MgO [14, 54–57] or in periodic crystals that lack inversion symmetry like (Ga,Mn)As [49–51].

Two different torques are found in these experiments; one torque is an even function of the direction of the magnetization  $\mathbf{m}$  and the other is an odd function of the direction of the magnetization. The even torque,

$\mathbf{T}^{\text{even}} = T^{\text{even}} \mathbf{m} \times [(\hat{e}_z \times \mathbf{E}) \times \mathbf{m}]$ , where  $\mathbf{E}$  is the applied electric field and  $\hat{e}_z$  is a unit vector perpendicular to the interface of the ferromagnetic heterostructure, is expected to be driven by the spin current due to the spin Hall effect (SHE), see below, in the heavy-metal layer [58, 59]. The odd torque,

$\mathbf{T}^{\text{odd}} = T^{\text{odd}}(\hat{\mathbf{e}}_z \times \mathbf{E}) \times \mathbf{m}$ , is expected to originate from the effective magnetic field due to spin dependent scattering in combination with the Rashba interaction, which originates from the broken inversion symmetry in the ferromagnetic heterostructures.

#### 2.4.4 Spin Hall effect

When a current is sent through a crystal or thin film and a magnetic field is applied normal to the current, a Hall voltage can be measured perpendicular to both the current and magnetic field [60]. In ferromagnetic materials, the Hall voltage consists of a contribution of the normal Hall effect and the anomalous Hall effect (AHE). When a current flows through a ferromagnet, the spin-orbit interaction gives rise to asymmetric scattering of the electrons. So, if the spin-up electrons have a larger probability to scatter to the left then the spin-down electrons have a larger probability to scatter to the right.

In 1971, Dyakonov and Perel [61, 62] predicted that the same mechanism responsible for the AHE, could cause a spin imbalance in a non-magnetic material. The work was rediscovered in 1999 by Hirsch [15], who labelled this phenomenon as spin Hall effect (SHE).

In the SHE, a spin current  $\mathbf{I}_s$  is generated transverse to a charge current  $\mathbf{I}_c$ , because the spin-orbit interaction causes an asymmetric scattering of the spin-up and -down electrons as shown in Figure 2.5. The spin current  $\mathbf{I}_s$  is equal to

$$\mathbf{I}_s = \alpha_{\text{SHE}} \boldsymbol{\sigma} \times \mathbf{I}_c, \quad (2.15)$$

where  $\alpha_{\text{SHE}}$  is a material dependent parameter characterizing the efficiency of the SHE. The spin-orbit interaction causing the SHE is also able to convert a spin current into a charge current by the inverse spin Hall effect (ISHE), where the charge current is equal to

$$\mathbf{I}_c = \alpha_{\text{SHE}} \mathbf{I}_s \times \boldsymbol{\sigma}. \quad (2.16)$$

The SHE and ISHE make a full-electric manipulation of spin possible, even without the use of magnetic materials. To obtain a large spin current, a large  $\alpha_{\text{SHE}}$  is needed. Up to now, most experiments use heavy paramagnetic materials such as Pt and Pd, because the strength of the spin-orbit coupling and thus also  $\alpha_{\text{SHE}}$  scales with  $Z^4$ ,  $Z$  being the atomic number. Recently, it has been shown that a large SHE can also be obtained when Cu is doped with Bi impurities [63, 64] or when heavy transition metals are grown in a high resistive phases as  $\beta$ -Ta [57] and  $\beta$ -W [65]. Wang et al. [66] proposed that the SHE can also be induced into

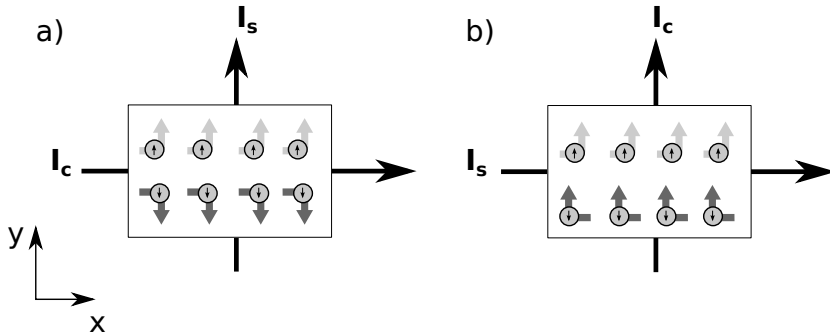


Figure 2.5: a) A spin current is induced by the spin Hall effect in a paramagnetic material. When sending a charge current in the  $x$ -direction, a spin current is generated in the  $y$ -direction due to the spin-orbit interaction. b) The inverse spin Hall effect induces a charge current in the  $y$ -direction when a spin current flows in the  $x$ -direction.

a thin normal metal when it is sandwiched between dissimilar insulators. The asymmetric interfaces break the inversion symmetry, which leads to a Rashba-type spin-orbit interaction. This spin-orbit interaction gives rise to a giant spin Hall conductivity.

### 2.4.5 Spin pumping

Where the spin transfer torque transfers angular momentum from a spin current to the magnetization of a ferromagnet, also the inverse process is possible. A precessing magnetization can emit an alternating spin current into an adjacent layer; a process called spin pumping, proposed by Berger [12] and Tserkovnyak [43, 67].

In Figure 2.6, spin pumping is schematically illustrated. In Figure 2.6.a, a ferromagnet in equilibrium is shown, where the density of states consists of a spin-up and spin-down band that are both filled up to the Fermi energy. If the magnetization of the ferromagnet is brought into a non-equilibrium state, the magnetization will relax by a spin-flip process of an electron above the Fermi energy into an empty state in the lower energy band. This process is called intrinsic damping [68, 69]. When there is an adjacent layer present, an additional relaxation process can occur. For ferromagnets that are thicker than the transverse coherence length, Tserkovnyak et al. [67] showed that the precessing



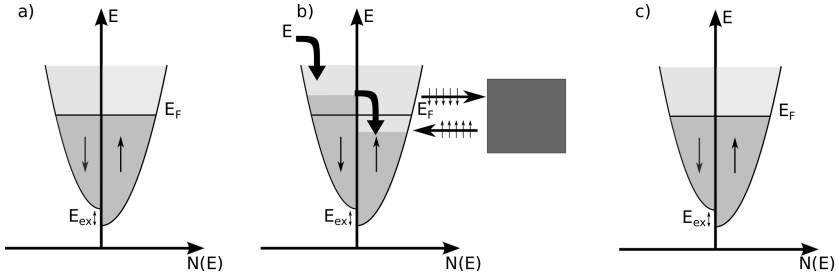


Figure 2.6: a) shows the Stoner model of a ferromagnet in equilibrium. Both the spin-up and -down band are filled up to the Fermi level  $E_F$ . They are shifted with respect to each other by the exchange energy  $E_{ex}$ . When the magnetization is brought into a non-equilibrium state (b), intrinsic relaxation can bring the ferromagnet back into equilibrium (c). When an adjacent layers is present, a spin current can be emitted into this layer to accelerate the relaxation (b). Adapted from [70].

magnetization emits a pure spin current

$$\mathbf{I}_s = \frac{\hbar}{4\pi} \left[ \text{Re}(G^{\uparrow\downarrow}) \mathbf{m} \times \frac{d\mathbf{m}}{dt} + \text{Im}(G^{\uparrow\downarrow}) \frac{d\mathbf{m}}{dt} \right] \quad (2.17)$$

into the adjacent layer with a spin-flip probability  $\epsilon$ . If the adjacent layer is a good spin sink,  $\epsilon > 10^{-2}$ , the spin current is efficiently absorbed, causing a decrease in the relaxation time. If the adjacent layer is a bad spin sink,  $\epsilon < 10^{-2}$ , no change in the magnetization dynamics will be observed. A bad spin sink can be turned into a good spin sink by doping it with spin-flip scatterers like heavy or magnetic impurities.

The spin-flip probability of a normal metals is mostly determined by the spin-orbit scattering. In normal metals, the spin-flip probability  $\epsilon$  is equal to the ratio between the elastic and spin-orbit relaxation time,  $\frac{\tau_{el}}{\tau_{so}}$ .  $\tau_{so}$  rapidly decreases with increasing  $Z$  and the spin sink effect becomes much more dominant with heavier elements such as Pt and Pd.

Furthermore, when the thickness  $d$  of the adjacent layer is smaller than the spin diffusion length  $l_{SD}$ , a spin accumulation is built up in the adjacent layer. Because the spins in the adjacent layer accumulate transverse to the magnetization of the ferromagnetic layer, the spin accumulation driven transport is described using the spin mixing conductance. Taking into account the spin accumulation, the spin mixing conductance  $G^{\uparrow\downarrow}$  in equation 2.17 is replaced by an effective spin pump-

ing efficiency  $A_{\text{eff}}^{\uparrow\downarrow}$  [43]

$$\frac{1}{A_{\text{eff}}^{\uparrow\downarrow}} = \frac{1}{G^{\uparrow\downarrow}} + \frac{R_{\text{sd}}}{\tanh(d/\lambda_{\text{SD}})}, \quad (2.18)$$

with  $R_{\text{sd}}$  is the resistance of the adjacent layer.

The extra damping  $\alpha'$  and the possible modification of the gyromagnetic ratio  $\gamma$  due to spin pumping is equal to [43]

$$\alpha' = \frac{\gamma_{\text{eff}}}{\gamma} \left[ \alpha + \frac{\hbar\gamma}{4\pi M_s A d_f} \text{Re} \left( A_{\text{eff}}^{\uparrow\downarrow} \right) \right], \quad (2.19)$$

where  $A$  is the area,  $d_f$  the thickness of the ferromagnet and  $\gamma_{\text{eff}}$  is the modified gyromagnetic ratio equal to [43]

$$\frac{\gamma}{\gamma_{\text{eff}}} = 1 - \frac{\hbar\gamma}{4\pi M_s A d_f} \text{Im} \left( A_{\text{eff}}^{\uparrow\downarrow} \right). \quad (2.20)$$

These two equations show that the spin pumping effect scales with  $1/d_f$ .

## 2.5 Spin-flip laser

In the previous sections we have seen what happens when a spin current flows from a normal metal into a ferromagnet. If the polarization of the spin current is non-collinear with the magnetization of the ferromagnet, the transverse component of the magnetization gives rise to a spin-transfer torque that can change the magnetization of the ferromagnet. Now, we will study what happens when a spin current is injected into a normal metal. Already in 1996, Berger [12] proposed that an injected current could excite spin waves in a ferromagnet. When injecting a spin current from a ferromagnet into a direct band semiconductor, it has been experimentally shown that circular polarized light can be emitted [71, 72]. In 2004, Kadigrobov [18, 19] proposed that when creating a non-equilibrium spin distribution in a normal metal or ferromagnet, there is a chance that this relaxes via a direct spin-flip transition and electromagnetic radiation is emitted. When it is possible to create a population inversion, even a spin-flip laser could be built. In 2006, Watts and van Wees [73] suggested that a MASER (Microwave Amplification by Stimulated Emission of Radiation) could be build when an external spin current is driven through a microwave created spin accumulation in a paramagnet.

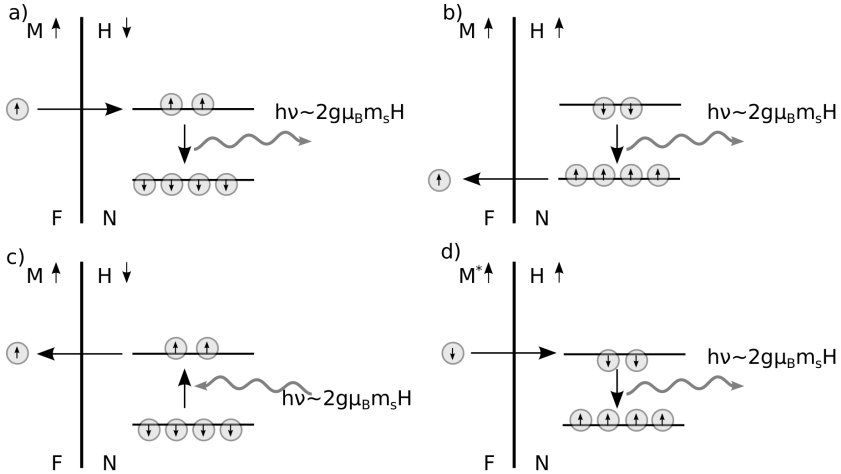


Figure 2.7: Four possible ferromagnet (F)/Normal metal (N) configurations, where a spin-flip process could generate a photon. In a), the magnetization  $M$  of F is antiparallel with the applied field  $H$ . Majority electrons are injected from F into N, leading to an inverse population of the Zeeman levels in N. A spontaneous or stimulated spin-flip process will emit a photon with the frequency proportional to the applied field  $H$ . b) When the magnetization  $M$  in F is parallel to the applied field  $H$ , electrons from the N layer are injected mostly in the majority band of F, resulting in an inversely populated Zeeman level in N. Again, a spontaneous or stimulated spin-flip process will emit a photon with the frequency proportional to the applied field  $H$ . In c), the magnetization  $M$  of F is antiparallel with the applied field  $H$ , but now the F/N bilayer is irradiated with photons with the energy equal to the Zeeman splitting. A spin-flip transition can be induced when a spin-down electron absorbs a photon. This will induce a photocurrent through the N into the F-layer. In d), the F layer is a minority type ferromagnet. When the magnetization  $M^*$  is parallel to the applied field, minority carriers will flow from the F into the N layer, creating an inversely populated Zeeman level. Again, a spontaneous or stimulated spin-flip process will emit a photon with the frequency proportional to the applied field  $H$ . Adopted from [74].

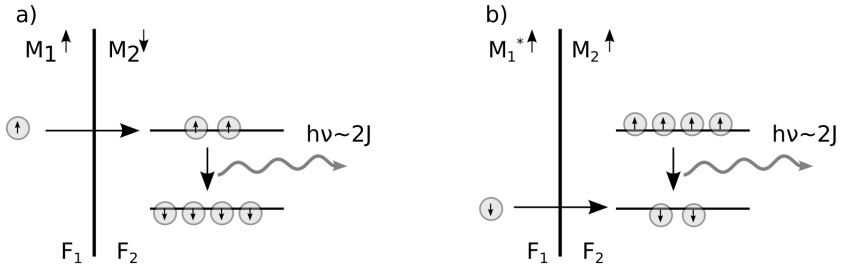


Figure 2.8: Two possible ferromagnet 1 ( $F_1$ )/ferromagnet 2 ( $F_2$ ) configurations, where a spin-flip process could generate a photon. The normal metal layer is replaced with a second majority type (a) or minority type (b) ferromagnet respectively. Photons are generated in a similar way as in the F/N bilayer, but instead of splitting the energy states in a normal metal with the Zeeman energy, now a ferromagnet is used and the energy splitting is caused by the exchange energy  $J$ . Adapted from [74].

In Figure 2.7, four different configurations are shown that can be used to build a spin-flip laser from a normal metal/ferromagnetic bilayer. When an external magnetic field  $H$  is applied to a normal metal, the energy eigenstates are Zeeman split. When injecting electrons into the highest energy level or removing electrons from the lowest energy level, a population inversion can be induced into the normal metal layer. The relaxation of the population inversion requires spin-flip processes. In the case the spin-flip relaxation mechanisms in the normal metal is slow, so the normal metal should be a bad spin sink, a spin-flip process accompanied with the emission of a photon with frequency

$$h\nu = 2g\mu_B m_s H, \quad (2.21)$$

can increase the relaxation rate. For a normal metal with a  $g$ -value of 2, the emitted frequency is equal to 28 GHz/T.

As predicted by Berger [75], a voltage can be generated in a magnetic multilayer undergoing ferromagnetic resonance when a magnon is created or annihilated by a spin-flip process. In Figure 2.7.c the inverse process is shown, where the ferromagnet/normal metal bilayer is irradiated with photons and a photocurrent is induced through the bilayer.

When replacing the normal metal with a weak ferromagnet, no external field is needed to split the energy levels. In Figure 2.8, two options are shown how a ferromagnet ( $F_1$ )/ferromagnet ( $F_2$ ) spin-flip

lasers can be built. Again, by injection or removing electrons, a population inversion can be created in  $F_2$ , that can relax using a spin-flip relaxation with the emission of a photon with frequency

$$h\nu = 2J, \quad (2.22)$$

where  $J$  is the exchange energy of  $F_2$ . For a ferromagnet, the exchange energy can be tuned from a few meV for weak ferromagnets up to a few eV for the strong ferromagnets. Since 1 eV would corresponds to 500 THz, a very broad frequency range can be obtained with a spin-flip laser.



# Point contact spectroscopy<sup>1</sup>

## 3.1 Point contact spectroscopy - theoretical

The electrical resistance of a contact with a size smaller than the electronic mean free path is only determined by the number of quantum channels and their transmission probability through this contact. These contacts, called Sharvin or point contacts (PC), were first used to determine the electron-phonon spectral function in normal metals.

Due to the size of the constriction, from a few nanometers up to hundreds of nanometers, it is possible to create very high current densities (of the order of  $10^{10}$  A/m<sup>2</sup>) without excessive heating effects. This allows to observe physical effects that cannot be seen with lower current densities like the spin-transfer torque.

The point contact geometry is also the preferred geometry to study the spin-flip laser, because the very high current density needed to obtain a non-equilibrium inverse population of the two spin-split levels. Furthermore, the point contact spectroscopy technique can be used to obtain information about the relaxation processes at the interface of the ferromagnet/normal metal.

The transport through such point contacts can be characterized by different transport regimes, depending on how the diameter  $d$  of the

---

<sup>1</sup>Parts of this chapter have been published in: E. Tartaglino, T.G.A. Verhagen, F. Galli, M.L. Trouwborst, R. Müller, T. Shiota, J. Aarts and J.M. van Ruitenbeek, *New directions in point-contact spectroscopy based on scanning tunneling microscopy techniques*, *Fizika Nizkikh Temperatur* **39** 249-260 (2013).

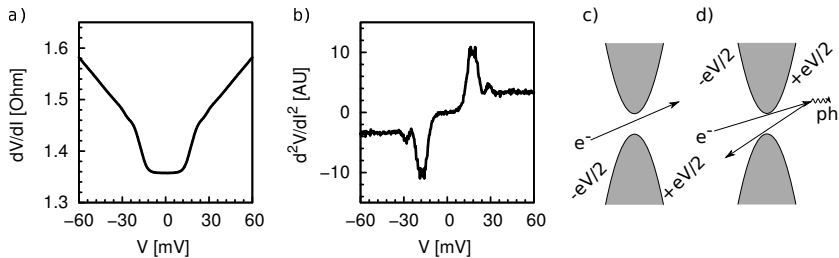


Figure 3.1: The in-house measured  $V - dV/dI$  and the numerically calculated  $V - d^2V/dI^2$  characteristics for a Cu-Cu point contact are plotted in a) and b) respectively. Due to the electron-phonon interaction, an increase in resistance can be observed around 16, 19 and 26 eV appearing as peaks in the  $d^2V/dI^2$ . Electrons travelling through a constriction gain an excess energy  $eV$  c). The electron-phonon interaction in a ballistic point contact can result in a backscatter event, d).

point contact scales to the elastic  $\ell_{el}$  and inelastic  $\ell_{in}$  electron mean free path and the Fermi wavelength  $\lambda_F$  of electrons. We can then distinguish the thermal regime, where  $d \gg \ell_{el}, \ell_{in}, \lambda_F$ , the diffusive regime  $\sqrt{\ell_{el}\ell_{in}} \gg d \gg \ell_{el}, \lambda_F$ , the ballistic regime  $\ell_{el}, \ell_{in} \gg d \gg \lambda_F$  and the quantum regime, where  $\ell_{el}, \ell_{in}, \lambda_F \gg d$ .

Below, we show and discuss a number of PC measurements which were meant as a first step to the final observation of radiation coming from the point contact. Inversely, it was attempted to observe spin flip processes due to irradiation, using a normal metal tip on a ferromagnetic film.

### 3.1.1 Electrical transport in a point contact

In 1965, Sharvin showed that the resistance of a ballistic point contact between two normal metals only depends on the diameter  $d$  of the point contact. The Sharvin resistance [76] is equal to

$$R_{Sh} = \frac{16\rho\ell_{el}}{3\pi d^2}, \quad (3.1)$$

where  $\rho$  is the resistivity of the material.

In Figure 3.1.a, the measured differential conductance  $dV/dI$  as a function of the applied voltage  $V$  and in Figure 3.1.b the numerically calculated  $d^2V/dI^2$  as a function of the applied voltage  $V$  are shown of a Cu-Cu point contact. A clear non-linearity can be observed that



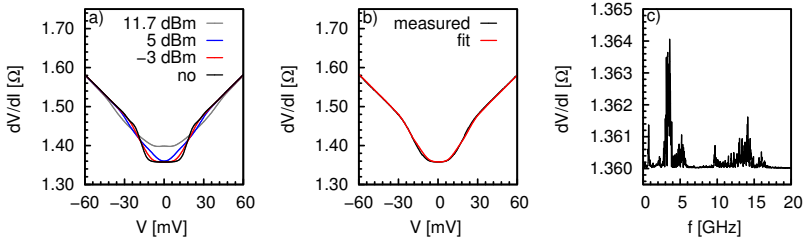


Figure 3.2: a) The resistance of a Cu-Cu point contact when it is irradiated with 4 GHz radiation at different power levels. In b), the influence of the radiation is modelled, assuming that the point contact works as a classical rectifier. c) shows the frequency dependence of the resistance of a point contact when it is biased at 15 mV.

can be attributed to electron-phonon scattering processes. As shown in Figure 3.1.c, for low applied biases, electrons passing through the constriction gain an excess energy  $eV$ . The electron can relax via an inelastic scattering event with a phonon. When this scattering takes place close to the constriction, the electron can be scattered back through the constriction (Figure 3.1.d) causing a backflow current.

The backflow current can be calculated, by assuming an energy dependent scattering length,  $l(eV) = v_F \tau_{e-ph}(eV)$ , with  $v_F$  the Fermi velocity and  $\tau_{e-ph}$  the energy dependent electron-phonon scattering time

$$\frac{1}{\tau_{e-ph}(eV)} = \frac{2\pi}{\hbar} \int_0^{eV} \alpha^2(\epsilon) F(\epsilon) d\epsilon, \quad (3.2)$$

with  $\alpha^2(\epsilon)F(\epsilon)$ , the electron-phonon interaction function. It follows straightforwardly that  $d^2V/dI^2$  is then equal to

$$\frac{dR}{dV} \propto \frac{d^2V}{dI^2} \quad (3.3)$$

$$\propto R_{Sh} \frac{3\pi^2 ed}{8\hbar v_F} \alpha^2(eV) F(eV). \quad (3.4)$$

So, by measuring the  $V - d^2V/dI^2$  of a ballistic point-contact, the electron-phonon interaction can be obtained.

Point contact spectroscopy (PCS) has developed into an ideal tool to probe a whole range of elementary excitations in all kinds of systems. In recent years, PCS became an important tool to probe the order parameter in superconducting materials like the cuprates [77] and

the pnictides [78], to measure the spin polarization of magnetic materials [79] and to measure transport properties of single atoms and molecules where the local vibration modes of the atoms or molecules can be detected [80]. Also, PCS helped to better understand the STT effect [35, 81]. The ability of PCS to distinguish between backscattering and impurity scattering clarified the role of impurities by the single-interface STT [81].

### 3.1.2 Irradiating point contacts

When irradiating a point contact with radiation with frequency  $\nu$ , the tip works as an effective antenna and the applied radiation induces oscillatory potentials  $V(t) = V_0 + V_{ac} \cos(2\pi\nu t)$  across the point contact. The response to the irradiation can be described as a classical detector where the induced oscillating potentials combine via a non-linearity into an ac-rectification, if the energy of the photons is smaller than the width of the non-linearity [82]. In Figure 3.2.a, the influence of irradiating a Cu-Cu point contact with 4 GHz radiation is shown. The current-voltage characteristic  $I(V)$  of an irradiated point contact can be modelled as

$$I(V) = \frac{1}{2\nu} \int_0^{1/2\nu} I_0(V_0 + V_{ac} \cos(2\pi\nu t)) dt, \quad (3.5)$$

where  $I_0(V_0)$  is the current-voltage characteristic in the absence of microwave radiation. In Figure 3.2.b, equation 3.5 is fitted to the 2 dBm curve of the measured spectra from Figure 3.2.a with a  $V_{ac}$  of 8 mV. If a constant bias voltage is applied to the point contact so that it is tuned to the non-linear part of the characteristic, the point contact will detect radiation by the amplitude of the rectified signal. In Figure 3.2.c, the frequency dependence of the signal detected by a point contact with a constant bias is shown. It shows that the coupling-efficiency of the point contact is strongly frequency dependent.

## 3.2 Point contact spectroscopy - experimental

In 1974 Yanson [83] used a metal-insulator-metal tunnel junction having a short, to measure energy resolved spectroscopy of the electronic scattering inside the metal, and could directly measure the energy dependence of the electron-phonon interaction. The introduction of the needle-anvil method by Jansen et al. [84] in 1976 was a further improvement. With this technique a sharply etched metal wire, the needle, was

pressed using a micrometer screw into a flat metal surface, the anvil, to form a point contact. The contact size can be adjusted by fine-tuning the pressure applied to the tip with the micrometer screw. Transport in such point contacts is ballistic since contact diameters are usually much smaller than the electron mean free path.

In the last 20 years also the development of STM, at or below liquid helium temperatures improved enormously [85]. One of the biggest problems in the design of low temperature STMs was the piezoelectric positioning system that often fails to work at these temperatures. The Beetle [86, 87] and the Pan-type [88] walker coarse positioner solved this problem and are now widely used in low temperature STMs. Nowadays, one can even buy commercial piezo positioners that reliably operate at low temperatures and at high magnetic fields [89].

### **3.2.1 Point contact spectroscopy measurement**

In a non-UHV environment, very thin native oxide layers, plus adsorbates of organic materials, are always present on both the tip and sample. A very important requirement is to make a clean metallic contact between the sample and the tip. For this purpose the tip is moved slowly with a micrometer screw or a piezo positioner to the sample, and when both parts are firmly pressed together, the greatest stress occurs at the point where the needle touches the sample. Here, the oxide layer breaks and forms a small direct metallic contact between the two parts: the point contact. Note that the presence of the oxide layer is not only a disadvantage: it can be helpful because it reduces the conducting electrical contact area between the tip and sample, while the mechanical contact area is much larger so that stable contact sizes between 4 and 100 nm can be made.

#### **3.2.1.1 Tip and sample preparation**

For various types of PCS experiments, different tip materials were used. We used Cu wires with a diameter of 125 and 500  $\mu\text{m}$ , Pb wires with a diameter of 500  $\mu\text{m}$  and Nb wires with a diameter of 250  $\mu\text{m}$  during the experiments. Although thick wires can produce good PCS spectra, the stiffness of the wire tends to damage the sample within a few cycles of breaking and making contacts. Using thinner wires and adding an extra loop with a diameter of approximately 2 mm into the wire, the force the tip can exert on the sample is reduced and the number of contacts that can be made and broken is increased.

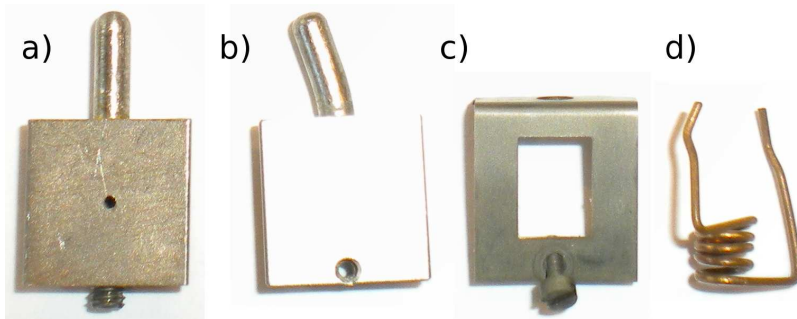


Figure 3.3: a)  $9 \times 9 \text{ mm}^2$  tip holder with on the bottom side the screw for tightening the mount of the tip wire. b)  $9 \times 9 \text{ mm}^2$  sampleholder onto which the substrate with the thin film or foil is glued. The hole in front of the sample holder is used to mount the Ti cap (c). For insulating substrates, a Ti cap (c) or Cu spring (d) are used to for making an electrical contact with the sampleholder.

In Figure 3.3.a, the titanium tip holder is shown where the tip is mounted in the hole and anchored with a titanium screw. After mounting the tip, the tip was etched to remove the thick native oxide layer. Cu tips were etched in a droplet of nitric acid, which resulted in a removal of the native oxide layer, which results in a rather flat apex. To obtain a conical apex, tips were electrochemically etched in a 25% HCl solution [90]. After etching, the tip has a typical conical apex of  $10 \mu\text{m}$  as can be seen in Figure 3.4 for a Cu tip.

Samples we used were either a thin film grown using sputter deposition or a thin sheet or foil. In Figure 3.3.c, the Ti sample holder is shown onto which the substrate or foil can be glued using silver paint. To make electrical contact to thin films grown on insulating substrates, the edges of the film were connected to the sample holder by means of a titanium cap (see Figure 3.3.b) or a copper spring (see Figure 3.3.d) to the sample holder.

Grown thin films were glued as quickly as possible onto the sample holder after the samples were removed from the deposition system to prevent the formation of a thick oxide layer. Foils and sheets were first glued onto the sample holder, whereafter the native oxide layer present on them was etched away using a nitric acid or 25% HCl solution until the surface looked shiny.

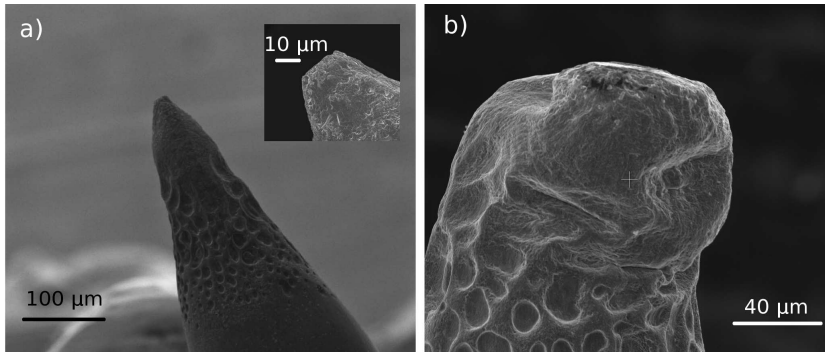


Figure 3.4: A scanning electron microscopy image of two different electrochemically etched Cu-tips before (a) and after (b) a point contact spectroscopy measurement with a piezo positioner.

### 3.2.1.2 Measurements

The point contact measurements were performed at 4.2 K in a liquid helium storage vessel, bath cryostat or in an optical cryostat with a variable temperature insert. The conductance and the phonon spectrum were measured using a current biased lock-in technique.

The point contact was made by carefully moving the tip with the piezo positioner or micrometer screw while simultaneously measuring the resistance between the tip and the sample. Before the contact was formed, a high constant resistance was observed, which is the result of combination of the native oxide and the vacuum gap between the tip and sample. When making the contact, the tip will first approach the oxide covered surface layer of the sample. When the tip touches the sample, it needs also to break the thin oxide layer to form a metallic contact. Unfortunately, we cannot distinguish these processes during the approach.

### 3.2.2 Scanning point contact spectroscopy

The measurements with the traditional micrometer-controlled needle anvil technique are often limited to a single position on the sample due to a lack of the ability to move the sample in a controllable way. A big improvement in PCS would be the ability to map the PCS data on the surface by such controlled motion of the sample. In Leiden, we started to explore the possibility to do scanning PCS. For this purpose, Simon

Kelly built a scanning PCS system, where he used a modified STM-insert [91] with an Attocube ANPz101 z-direction nanopositioner and a scantube to move the tip in the x- and y-direction, which is shown in Figure 3.5. For the first tests, only the z-direction was used.

We noticed that if we made our first contacts with a fresh tip and fresh sample, when we made a metallic contact and retracted the tip just far enough that we lose the metallic contact, the next approach takes much longer than expected from the retraction distance. The crack in the oxide layer forms at a different place than before and the piezo positioner needs a lot of steps to break the oxide layer. It is also possible that instead of breaking the oxide layer, a metallic contact is formed by deforming the tip, as can be seen in Figure 3.4.b, where the tip is imaged just after good ballistic contacts were measured.

The main drawback of the low-temperature piezo positioners is that they are designed for accurate positioning (several tens of a nm), but not to apply forces large enough to break oxide layers. In contrast, the micrometer screw can continuously apply the same force and break the oxide layer in a continuous way.

### 3.2.3 Micrometer screw point contact spectroscopy

To circumvent the problem of piezo positioners, also PCS inserts were built where the tip was connected via a drive shaft to a micrometer screw mechanism, which is capable of moving the tip with 1  $\mu\text{m}$  per revolution. This established method [92] results in a reliable way of making point contacts. In Figure 3.6, two PCS inserts that were built are shown. The insert in Figure 3.6.a is designed such that it fits in the variable temperature insert of an Oxford optical cryostat without blocking the optical path too much. Figure 3.6.b shows the vertical PCS insert for a bath cryostat with a solenoid superconducting magnet. By placing the sample- and tipholder vertically, the magnetic field is in-plane.

## 3.3 Spin-flip laser

One possible experimental realization to test the theoretical prediction of a metal based spin-flip laser as described in Section 2.5 is shown in Figure 3.7.a. Using the mechanical point contact geometry, an F/N contact is created. As the ferromagnet a thin  $\text{SmCo}_5$  film is used, which has the advantage that it has a large coercive field which results in a wide magnetic field and frequency domain to test the theory. In the

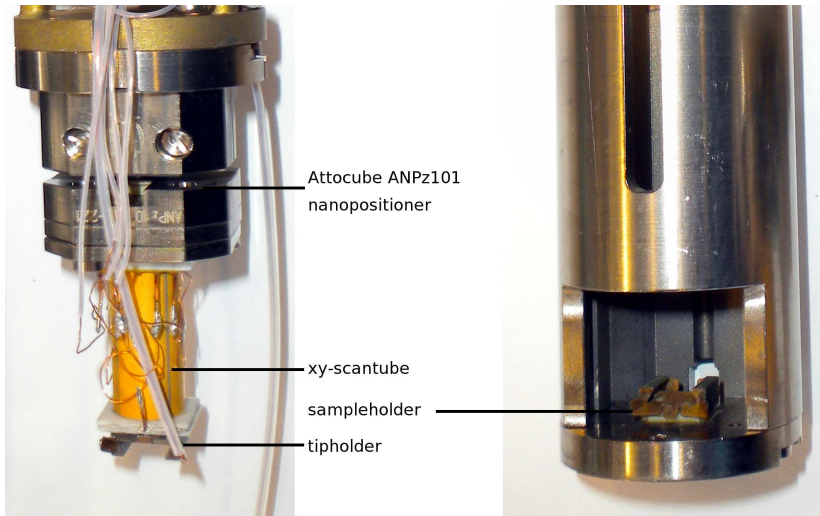


Figure 3.5: Point contact spectroscopy head based on the Attocube ANPz101 nanopositioner and a scan tube to scan in the  $x$ - and  $y$ -direction. The tipholder is mounted below the scan tube and the sample holder is mounted at the bottom of the protection cap, that is mounted around the piezo nanopositioners.

literature, many groups have shown that thin Sm-Co films with a large coercive field can be grown using sputter deposition [93–99]. The advantage of thin films is that different materials as a capping layers can be used, to protect the Sm-Co surface or to manipulate the properties of the spin-flip laser. As the normal metal part of the spin-flip laser, a Cu tip is used.

It is very difficult to detect the emission of a few photons that might be emitted from the F/N point contact. We therefore irradiate the point contact with microwave radiation, as is shown in the configuration of Figure 2.7.c and detect spectroscopically if spin-flip processes are happening. With a constant voltage bias, the resistance of the irradiated point contact is measured as a function of the applied magnetic field. When the resonance condition, equation 2.21, is fulfilled, a peak in the resistance as illustrated in Figure 3.7.b is expected. There must be a linear relation between the resonance field and the applied microwave radiation, as shown in Figure 3.7.c.

In Figure 3.8.a, typical PCS measurements are shown that were done

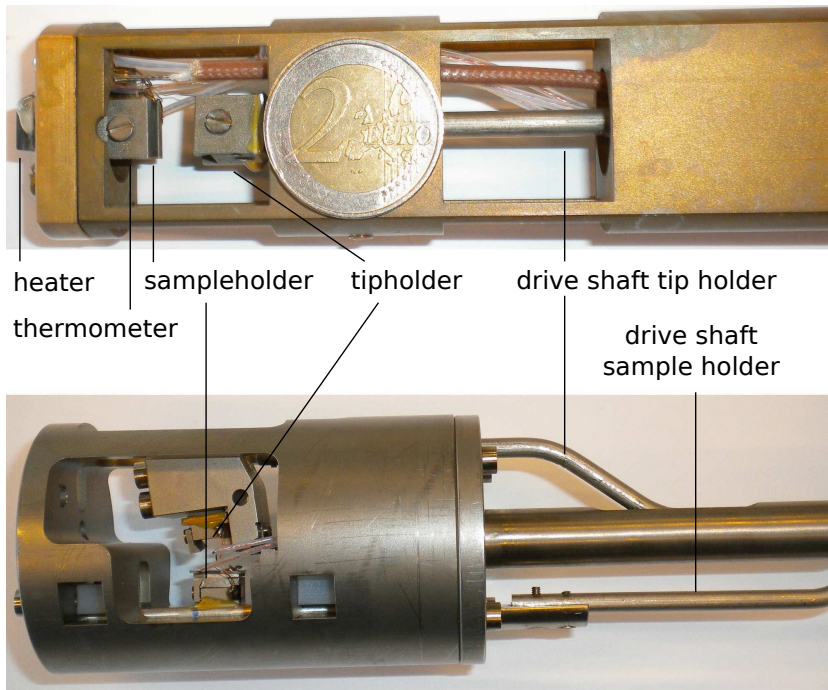


Figure 3.6: a) Micrometer screw based point contact spectroscopy insert. The sample- and tipholder can be mounted and secured with a screw. The tipholder is attached to a drive shaft, that is connected to a micrometer screw, which stays at room temperature (not shown). The temperature is measured using a thermometer that can be mounted just below the sample- or tipholder and at the bottom of the insert a heater is mounted to control the temperature. Also an open-ended coax cable is present to irradiate the sample. b) Micrometer screw based vertical point contact spectroscopy insert, that is also able to move the sample using another micrometer screw.



in Leiden on Sm-Co thin films deposited by sputtering (see Chapter 4) with a Cu capping layer. None of the measurements on the Sm-Co films has shown a signature of the spin-transfer-torque (STT) peaks or the Zeeman-resonances. However, measurements done at the B. Verkin Institute for Low Temperature Physics and Engineering of the National Academy of Sciences of Ukraine (ILT), showed for several films the STT effect, as shown in Figure 3.8.b and even an indication of the spin-flip laser effect, as shown in Figure 3.8.c. Unfortunately, also at ILT only a few of these measurements were successful and no studies could be done of the resonance field versus microwave frequency or the influence of the applied bias.

### 3.4 Discussion

Basically, there are two ingredients that might be responsible for the low reproducibility of the experiments. First, the surface quality of the Sm-Co is not well defined. From the growth of the Sm-Co thin films on MgO(100) and MgO(110) substrates, we learned that these films are generally not single crystalline. Furthermore, in Chapter 4 we show how different the crystallites can behave with small variations in the Sm-Co composition and the sputter gas pressure.

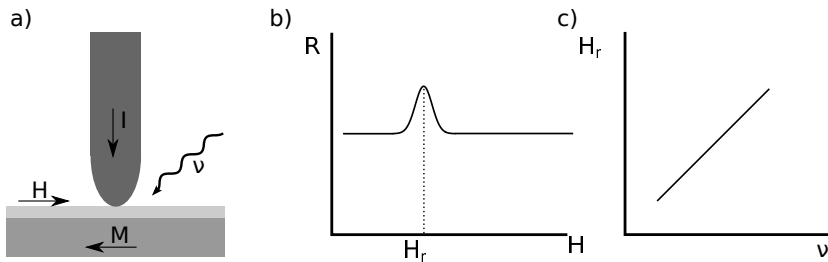


Figure 3.7: a) Experimental set-up for measuring the spin-flip laser using a mechanical point contact. b) The expected dependence of the resistance  $R$  of the point contact as a function of the applied magnetic field  $B$  for a point contact with a constant bias. When irradiating the point contact with microwave radiation with a frequency  $\nu$ , there is an increase in resistance when the resonance condition, equation 2.21, is fulfilled. c) The resonance magnetic field as a function of the irradiating frequency is expected to show a linear relation for the Zeeman-splitting based spin-flip laser.

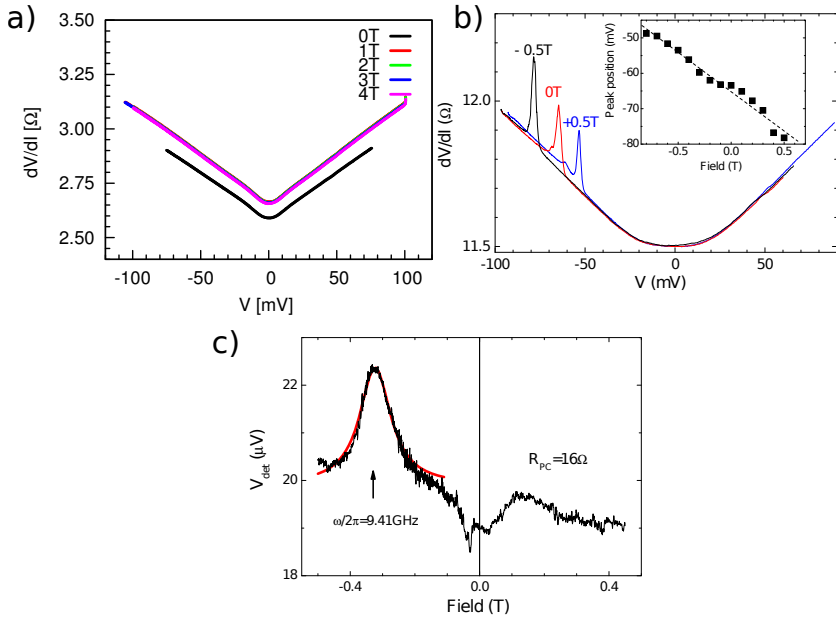


Figure 3.8: a) Typical Leiden point contacts measurements on a Sm-Co/Cu thin film with a Cu tip, with and without an applied in-plane magnetic field. The 1, 2, 3 and 4 T curves are overlaying each other. b) The differential resistance of a SmCo<sub>5</sub>/Cu point contact measured at the B. Verkin Institute for Low Temperature Physics and Engineering of the National Academy of Sciences of Ukraine as a function of the bias voltage at an applied field of -1.0, 0 and 0.5 T. A clear STT peak is visible. In the inset, the position of the STT peak versus the magnetic field is plotted. c) Detected voltage  $V_{det}$  as a function of the applied magnetic field for a SmCo<sub>5</sub>/Cu point contact under microwave irradiation at 4.2 K and biased with -20 mV. The arrow indicates the resonant magnetic field  $H_7$  for which the photon energy fulfills the resonance condition. Figure b) and c) taken from [74]

At ILT, SmCo<sub>5</sub> films capped with 3-5 nm thick Cu, Cr, Al, Fe or Co layers were investigated, that were grown at the Leibniz Institute for Solid State and Materials Research in Dresden. PCS on SmCo<sub>5</sub> films with a Cr capping layer and Cu or Ag tips showed non-metallic behaviour, likely due to forming of a dielectric layer on the surface (probably chromium oxide), which is good for protecting the ferromagnetic surface but makes it difficult to form stable metallic tip-surface point contacts. SmCo<sub>5</sub> films with an Al, Fe and Co capping layer showed metallic behaviour, but ILT did not succeed to observe resistance features associated with resonant photon emission or absorption [100]. Films capped with a thin Cu layer resulted in the observation of the expected features. In Figure 3.8.b, the observed STT is shown for different applied magnetic fields. The observation of the STT tells, that the SmCo<sub>5</sub>/Cu interface is spin polarized. Multiple measurements on the SmCo<sub>5</sub>/Cu samples showed the degradation of the surface properties, which potentially has been the cause for poor reproducibility of the results.

The other ingredient where we have little control over is the exact orientation of the magnetization direction in the SmCo<sub>5</sub> domain in the point contact and the direction of the magnetic field component of the applied microwave radiation.

Although in some of the point contacts the STT effect is observed, the orientation of the magnetization in the SmCo<sub>5</sub> domain where the Cu tip is touching is unknown. When the contact with the Cu tip is made, some pressure is applied to the SmCo<sub>5</sub> film. The pressure to the film can induce locally stress to the film, which can rotate the in-plane magnetization into a slightly different direction. This is supported by the observation of the STT, which needs a non-collinear magnetization to convert a spin current to a torque.

### 3.5 Outlook

To obtain more control over the formation of the point contacts, lithographic point contacts can be used instead of the point contacts that were made using the traditional needle-anvil method. When growing the different layers in-situ, there is a clean interface between the different materials. Furthermore, no extra stress to the contact with the needle is induced in the Sm-Co film which might change the (magnetic) properties of the Sm-Co.

We also sought for a different way to characterize the F<sub>1</sub>/N, F<sub>1</sub>/N/F<sub>2</sub> and F<sub>1</sub>/f/F<sub>2</sub> configurations with respect to the behaviour of spin. In

particular, it would be useful to know whether spin can be transferred to and from the Sm-Co layer. We therefore initiated a set of experiments in which ferromagnetic resonance (FMR) is used to pump spin out of an F layer and study which properties play a crucial role in the spin torque and spin pumping phenomena. Co films were used for these measurements (see Chapters 5 and 6).

Furthermore, the combination of a lithographic point contact with the spin Hall effect might be an interesting route to create a spin-flip laser. The spin Hall effect makes it possible to inject a fully polarized spin current into an adjacent layer, which helps to circumvent the usage of traditional ferromagnets that possess low coercive fields or hard ferromagnets that are complicated to grow (see Chapter 4).

# Sm-Co thin films

In this Chapter, we study the growth of Sm-Co thin films. They are of use as the strong ferromagnet in the ferromagnet/normal metal and ferromagnet/weak ferromagnet spin-flip laser. Sm-Co ferromagnets have the advantage that they have a large coercive field, which results in a wide magnetic field and frequency domain to test the spin-flip laser theory. In the literature, many groups have shown that thin Sm-Co films with a large coercive field can be grown using sputter deposition [93–99]. Furthermore, Sm-Co films have the advantage over bulk crystals that on top of the film in-situ an additional thin layer can be grown that can act for example as a protection layer against oxidation or as a spin-filter.

## 4.1 Sm-Co based magnetic materials

Modern permanent magnetic materials, like  $\text{SmCo}_5$  or  $\text{Nd}_2\text{Fe}_{14}\text{B}$ , are based on intermetallic compounds of some rare-earth (RE) and 3d transition metals (TM). The materials are distinguished by high coercive fields caused by a high magnetocrystalline anisotropy with the easy magnetization direction along the c-axis of their hexagonal ( $\text{SmCo}_5$ ) or tetragonal ( $\text{Nd}_2\text{Fe}_{14}\text{B}$ ) structure.

The magnetic structure of Sm-Co binary systems is formed by Sm and Co sublattices that are both ferromagnetic [101, 102]. The magnetism in the Sm sublattice originates from the incompletely filled 4f electron shell of the  $\text{Sm}^{3+}$  ion (three electrons in 5d and 6s shells).

The 4f states are located deep in the atom, shielded by 5d and 6s electrons and therefore keep their localized character; the magnetism can be well described by the atomic characteristics of a free RE<sup>3+</sup> ion using Hund's rules. The Co sublattice keeps its itinerant character with magnetic moment originating from the electron spin of the unpaired 3d electrons [103] of its 3d<sup>6</sup> configuration.

In the RE-TM compounds, the spin moments of RE and TM are always aligned antiparallel. According to Hund's third rule, for electron shells that are filled less than half, the total angular momentum  $J$  forms as  $J = L - S$ , while for the shells filled more than half the total angular momentum forms as  $J = L + S$ . As a Sm<sup>3+</sup> ion has 5 electrons in the 4f shell, the orbital angular momentum ( $L = 5$ ) and spin angular momentum ( $S = \frac{5}{2}$ ) are oriented opposite to each other ( $J = \frac{5}{2}$ ). The total angular momentum for the Sm-sublattice is thus opposite to the spin angular momentum. The total magnetic momentum of the Sm-Co is the sum of the total magnetic moments of the Sm- and Co-sublattices, which are parallel aligned to each other and results in ferromagnetic behaviour.

The high uniaxial anisotropy is the result of the combined individual anisotropies of the Co and Sm sublattices, the Co-sublattice favors an uniaxial c-axis alignment, which is strengthened by the Sm sublattice that also favours c-axis alignment [103].

#### 4.1.1 Phase diagram

The Sm-Co binary compounds have been intensively investigated since the 1970s, mainly for their exceptional magnetic properties [103]. Buschow [104] and Khan [105] systematically investigated the Sm-Co binary system when searching for new, improved permanent magnets. The phase diagram of the Sm-Co system is shown in Figure 4.1. In Table 4.1, crystal structure data and Curie temperatures are presented for all the reported compounds. One can see that the compounds with a high Curie temperature, important for making permanent magnets, are at the Co-rich side of the phase diagram: Sm<sub>2</sub>Co<sub>17</sub> (89.5 at % Co), SmCo<sub>5</sub> (83.3 at % Co), Sm<sub>5</sub>Co<sub>19</sub> (79.2 at % Co), Sm<sub>2</sub>Co<sub>7</sub> (77.8 at % Co) and SmCo<sub>3</sub> (75.0 at % Co). All these compounds are incongruently melting materials structurally related to each other. Moreover, SmCo<sub>5</sub> is a metastable compound and Sm<sub>2</sub>Co<sub>17</sub> has two polymorphs. This brings difficulties with it in both single crystal and thin film growth of desired single-phase materials, as discussed later. From the structural point of view, the different Sm-Co phases can be derived from the SmCo<sub>5</sub>-phase

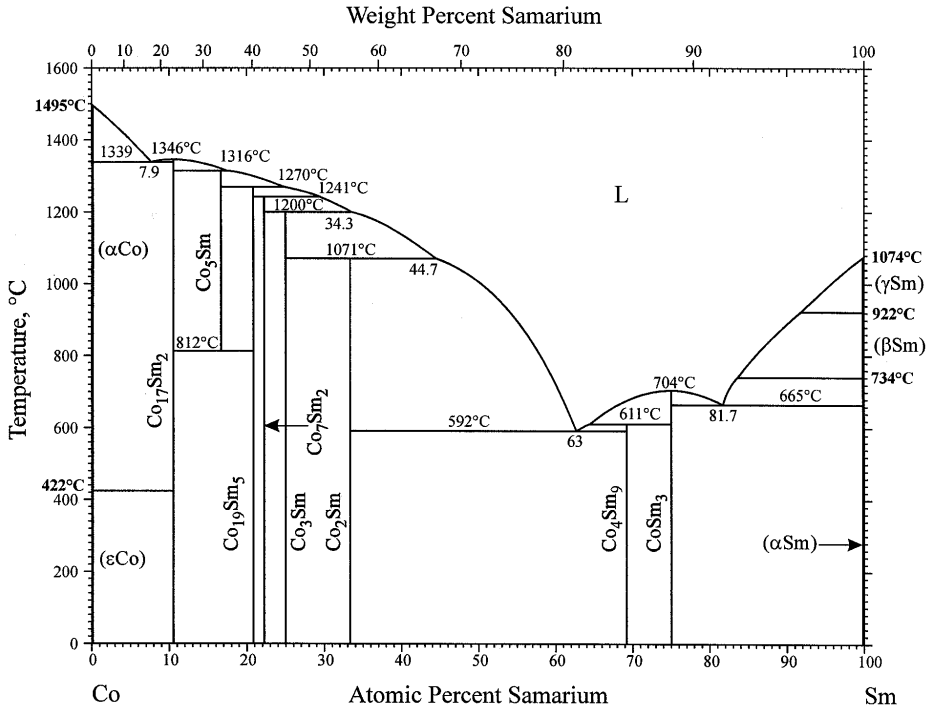


Figure 4.1: Sm-Co binary phase diagram [106]. Reprinted with kind permission from Springer Science and Business Media.

by substitution of a Co-atom by a Sm-atom or vice versa, followed by appropriate shifts of neighboring layers of atoms.

The unit cell of  $\text{SmCo}_5$  is shown in Figure 4.2. In that cell, the Sm-atom is located at position  $(0, 0, 0)$  and the Co atoms are located at  $(\frac{1}{3}, \frac{2}{3}, 0)$ ,  $(\frac{2}{3}, \frac{1}{3}, 0)$ ,  $(\frac{1}{2}, 0, \frac{1}{2})$ ,  $(0, \frac{1}{2}, \frac{1}{2})$  and  $(\frac{1}{2}, \frac{1}{2}, \frac{1}{2})$ . Figure 4.3 shows how the  $\text{Sm}_2\text{Co}_7$ -unit cell can be obtained starting from the  $\text{SmCo}_5$  lattice structure. In Figure 4.3.a several  $\text{SmCo}_5$  unit cells are drawn, seen along the crystallographic  $b$ -direction. The first step to obtain  $\text{Sm}_2\text{Co}_7$ , is to replace in each third layer the Co-atom at position  $(\frac{2}{3}, \frac{1}{3}, 0)$  with a Sm-atom, as shown in Figure 4.3.b. The unit cell consists now of two  $\text{SmCo}_5$  unit cells sandwiched between  $\text{SmCo}_2$  unit cells, which makes the total unit cell three times as big. The substitution is followed by a shift of alternating unit cells by  $[\frac{2}{3}, \frac{1}{3}, 0]$  and a relaxation of the Sm-atoms that are too close to each other. This results in the  $\text{Sm}_2\text{Co}_7$  unit cell, shown

Table 4.1: Crystal structure data [104, 108, 109] and Curie temperatures [110] for the different Sm-Co phases.

Compound	Space group	Crystal symmetry	Structure type	Lattice constants [Å]	T <sub>Curie</sub> [°C]
$\alpha$ -Sm <sub>2</sub> Co <sub>17</sub>	R $\bar{3}m$	rhombohedral	Th <sub>2</sub> Zn <sub>17</sub>	a = 8.395 c = 12.216	> 400
$\beta$ -Sm <sub>2</sub> Co <sub>17</sub>	P6 <sub>3</sub> /mmc	hexagonal	Th <sub>2</sub> Ni <sub>17</sub>	a = 8.360 c = 8.515	> 400
SmCo <sub>7</sub>	R $\bar{3}m$	rhombohedral	Th <sub>2</sub> Zn <sub>17</sub>	a = 4.856 c = 4.081	> 400
SmCo <sub>5</sub>	P6/mmm	hexagonal	CaCu <sub>5</sub>	a = 4.982 c = 3.964	> 400
Sm <sub>5</sub> Co <sub>19</sub>	R $\bar{3}m$	rhombohedral	Co <sub>19</sub> Ce <sub>5</sub>	a = 5.031 c = 32.265	
Sm <sub>2</sub> Co <sub>7</sub>	P6 <sub>3</sub> /mmc	hexagonal	Ce <sub>2</sub> Ni <sub>7</sub>	a = 5.041 c = 24.327	20 - 400
SmCo <sub>3</sub>	Pnma	rhombohedral	GdZn <sub>3</sub>	a = 5.050 c = 24.950	20 - 400
SmCo <sub>2</sub>	Fd3m	cubic	MgCu <sub>2</sub>	a = 7.260	< 20
Sm <sub>9</sub> Co <sub>4</sub>		orthorombic	-	a = 11.15 b = 9.461 c = 9.173	< 20
Sm <sub>3</sub> Co	Pnma	orthorombic	Fe <sub>3</sub> C	a = 7.090 b = 9.625 c = 6.342	< 20



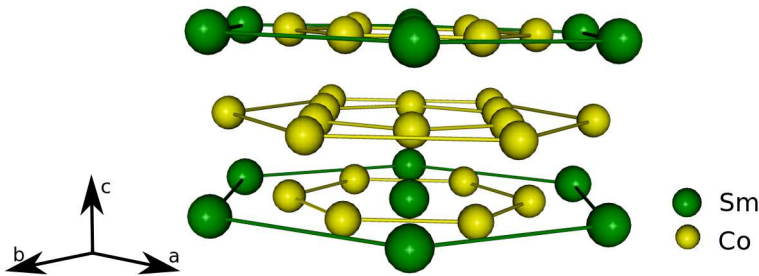


Figure 4.2: Lattice structure of  $\text{SmCo}_5$ . Image made with the program Molekel [107].

in Figure 4.2.c and d, which is six times as large as a  $\text{SmCo}_5$  unit cell.

When replacing a Co atom with a Sm atom in each second layer instead of each third layer of  $\text{SmCo}_5$ , followed by the appropriate shift of neighboring layers, the result is the  $\text{SmCo}_3$  phase. The substitution in each fourth layer would result in the  $\text{Sm}_5\text{Co}_{19}$  phase, with a hexagonal unit cell with a  $c$ -axis of  $32 \text{ \AA}$ , and the substitution in each fifth layer would result in the  $\text{SmCo}_4$ -phase, with a hexagonal unit cell and a  $c$ -axis of  $40 \text{ \AA}$ .

Another substitution scheme is the substitution of a Sm atom by pairs of Co atoms, which are usually called 'dumbbells'. In Figure 4.4.b, unit cells of  $\text{SmCo}_5$  seen along the  $c$ -axis, are drawn with black lines. The  $\text{Sm}_2\text{Co}_{17}$ -phase is obtained from the  $\text{SmCo}_5$ -phase by replacing each third Sm-atom with a pair of Co-atoms. The unit cell of  $\text{Sm}_2\text{Co}_{17}$  is drawn with gray dotted line, where the replaced Sm atom is located at position A or B. The two Co-atoms substituted for the Sm atom are situated just above or below the basal plane of the unit cell. If the adjacent layers are stacked with the replaced Sm atom alternating at the A and B position, the hexagonal  $\text{Sm}_2\text{Co}_{17}$  is formed.

The  $\text{SmCo}_7$  phase can be formed in a similar way, but now  $\frac{2}{9}$  of the Sm atoms is replaced with a Co-pair.

The different Sm-Co phases are clearly closely related to each other and a small variation in the Sm concentration can result in different stacking "faults" which result in a different Sm-Co phase.

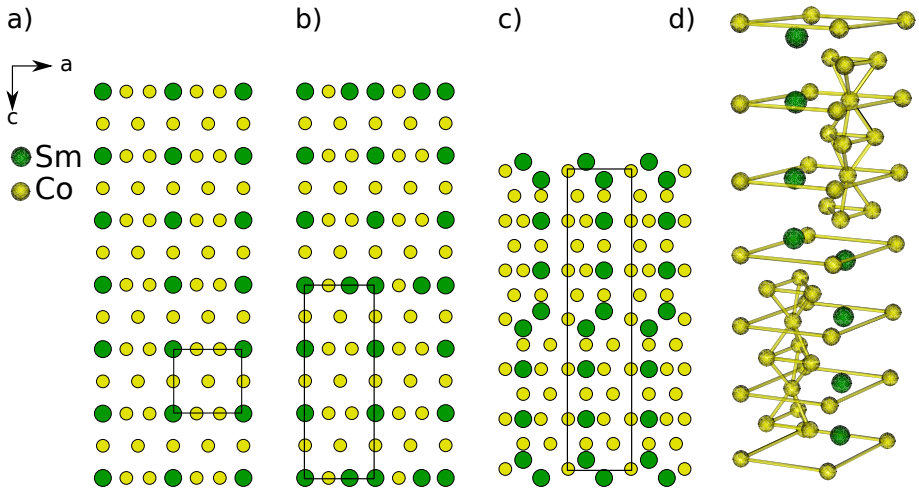


Figure 4.3: Construction of  $\text{Sm}_2\text{Co}_7$  from  $\text{SmCo}_5$ . In a), the  $\text{SmCo}_5$  structure is shown, projected along the  $b$ -axis. In every third unit cell, a Sm atom is substituted for a Co-atom, as shown in b), whereafter a block of two  $\text{SmCo}_5$  unit cells sandwiched between  $\text{SmCo}_2$  unit cells is shifted by  $(\frac{2}{3}, \frac{1}{3}, 0)$ , as can be seen in c). In d), the  $\text{Sm}_2\text{Co}_7$  unit cell is shown. Image d) made with the program Molekel [107].

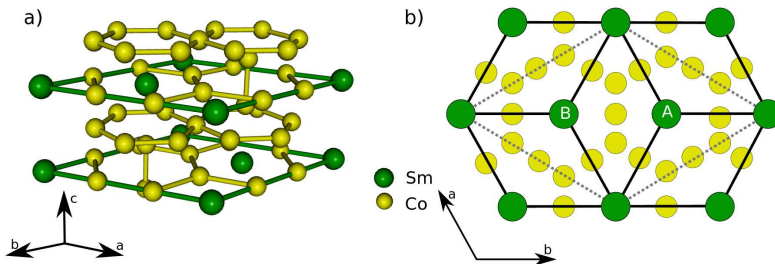


Figure 4.4: a) Structure of  $\text{Sm}_2\text{Co}_{17}$ , where in b) the atomic arrangement of a Sm sublattice in the basal plane is shown. The black lines indicate the  $\text{SmCo}_5$  unit cell, where the gray dotted line indicates the  $\text{Sm}_2\text{Co}_{17}$  unit cell. Depending on the layer, a pair of Co atoms is at A and a Sm atom at B or vice versa. Image b) made with [107].

### 4.1.2 Sm-Co thin films

In the last years, recipes have been developed to grow films with the desired hard magnetic properties. One way to obtain them is to grow epitaxial thin films. Epitaxial growth can be obtained by using MgO(100), MgO(110) and Si(100) single crystal substrates, commonly in combination with a chromium buffer layer.

Sm-Co films can also be deposited on a glass substrate. Growing on glass results in very small crystallites in a disordered structure, but still yields large coercive fields [99].

Singh et al. [111] showed that growing Sm-Co films on the four-fold symmetric MgO(100) substrates results in the epitaxial relation  $\text{Sm-Co}(11\bar{2}0)[0001] // \text{Cr}(001)[110] // \text{MgO}(001)[100]$  (schematic diagram shown in Figure 4.5.a), where the Sm-Co grains are equally distributed along the two in-plane directions and the c-axis lies in the plane. Singh et al. [112] also showed that growing Sm-Co films on MgO(110) substrates results in the epitaxial relation  $\text{Sm-Co}(10\bar{1}0)[0001] // \text{Cr}(211)[0\bar{1}1] // \text{MgO}(110)[001]$ . Figure 4.5.b shows a schematic diagram how the Cr seed layer and hexagonal Sm-Co grows on MgO(100) and MgO(110).

Thin Sm-Co films are mostly grown using pulsed-laser deposition (PLD) [114–116] or sputter deposition [97–99] from single elemental targets Sm and Co. By tuning the sputter power of both sources or the pulse ratio by PLD, it is possible to grow compositions in the desired range. Sm-Co films can also be grown using sputter deposition [93–96] or PLD [117] from commercial alloy targets of  $\text{SmCo}_5$ .

One of the underlying problems of growing thin Sm-Co films, is the complexity of the Sm-Co phase diagram [106] which just has been discussed. The connection between composition and magnetic properties is therefore not trivial. Fortunately, high coercive fields can be found over a wide range of compositions and a number of studies [95, 98, 99] has focused on this particular aspect.

## 4.2 Experiment

The Sm-Co films in our experiment were deposited in a UHV chamber (base pressure  $1 \times 10^{-9}$  mbar) using DC magnetron sputter deposition with argon as plasma. Films were deposited on 500  $\mu\text{m}$  thick MgO(100) and MgO(110) single crystal substrates on which a 100 nm thick Cr buffer layer was first deposited at 250°C in an Ar pressure of  $1.5 \times 10^{-3}$  mbar.

The Sm-Co films grown from a commercial  $\text{SmCo}_5$  (3N) alloy target were approximately 100 nm thick and were grown at 450°C with an

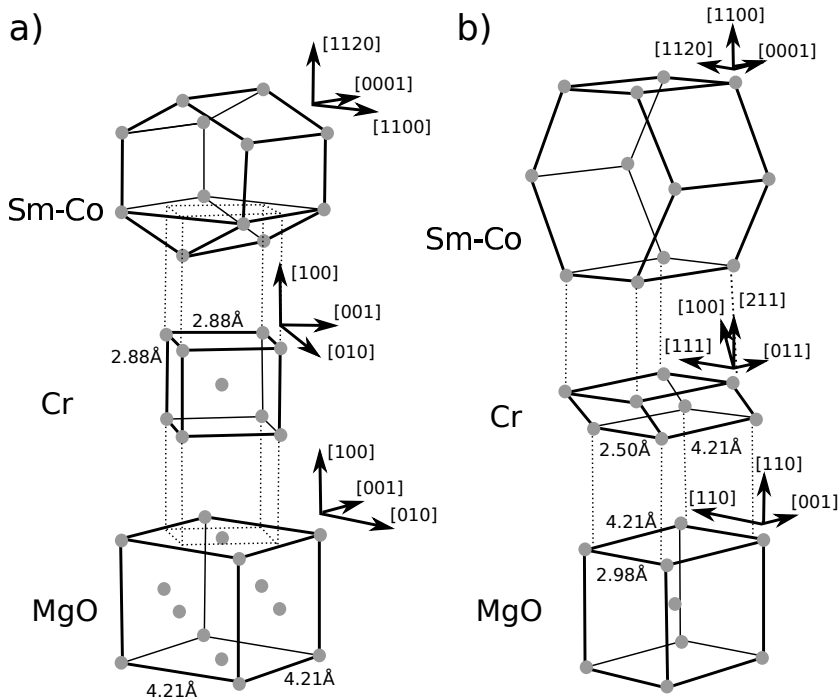


Figure 4.5: The unit cells (bold lines) and epitaxial relationships for the growth of a Cr buffer layer and a Sm-Co film on MgO(100) (a) and MgO(110) (b). Images adapted with permission from [113] © (1996), AIP Publishing LLC.

Ar pressure varying between  $1.5 \times 10^{-3}$  and  $12.5 \times 10^{-3}$  mbar and a deposition rate of approximately 4 nm/min. Afterwards, a 10 nm thick Cr layer was deposited at 450°C as a protection layer.

The Sm-Co films grown from single elemental Co (3N5) and Sm (3N) targets were approximately 100-140 nm thick and were grown with an argon pressure of  $3.8 \times 10^{-3}$  mbar at 450°C and a deposition rate of 3 nm/min. Afterwards, a 10 nm thick Cr or Cu layer was deposited at 100 °C as a protection layer. Different Sm-Co compositions were grown by varying the sputter power of the Co and Sm sources. The deposition rate is linear in the sputter current and 1 mA sputter current corresponds to approximately 0.2 Å/min for Co and 0.3 Å/min for Sm.

The deposition rate was measured by X-ray reflectivity (XRR) using Cu-K $\alpha$  radiation and a rotating sample holder was used to obtain an uniform composition in the film.

The actual film composition and thickness were determined using Rutherford Backscattering (RBS). The structural quality of the film was measured with  $\theta$ -2 $\theta$  X-ray diffractometry (XRD) using Cu-K $\alpha$  radiation, where the MgO substrate peak was measured as a reference for the angle, by using an extra Cu-absorber to decrease the intensity. The morphology of the films was characterized by Atomic Force Microscopy (AFM) in tapping mode. Magnetization measurements were performed in a SQUID-based magnetometer (MPMS 5S from Quantum Design) in fields up to 5 T. For the magnetization measurements, the substrates were cut in pieces of approximately  $10 \times 4 \text{ mm}^2$ . As a reference, MgO(100) and MgO(110) substrates were measured, and also an MgO(100) substrate with a 100 nm Cr film protected with 30 nm Cu. Electron paramagnetic resonance (EPR) spectra were measured at room temperature using a Bruker EMX plus X-band spectrometer in a TE<sub>011</sub> cavity with 100 kHz modulation frequency and 1 G modulation amplitude.

### **4.3 Magnetic properties of Sm-Co thin films grown on MgO(100) deposited from a single alloy target**

For various applications, growing Sm-Co thin films from alloy targets is a desirable option since only one deposition source is needed. Still, as far as we know, relatively few groups [93–96, 118–122] have reported on the growth of Sm-Co thin films from single alloy targets. The purpose of the next section is to show what the properties are of such films, grown on MgO(100), and in a range of pressures. In order to offer a reference frame for our results, we start with a paragraph outlining what has been achieved earlier in terms of coercive fields and saturation magnetization or remanence. We then present experimental details of our work, results of the measurements, and a discussion.

#### **4.3.1 Single alloy targets; previous results**

It is useful to compare results from single target growth to typical results from multiple targets. Without being exhaustive, PLD growth using multiple targets on Cr-buffered MgO(100) and MgO(110) was discussed by Singh *et al.* [114, 123]. In the first case, the more or less equal distribution of grain axes along the two in-plane directions leads to a remanent field  $\mu_0 M_r$  of about 0.5 T when measuring along MgO(100),

as can be expected from the saturation magnetization  $\mu_0 M_s$ , which is about 1.1 T for  $\text{SmCo}_5$ . The room temperature coercive field  $\mu_0 H_c$  was 2.4 T in this case. For growth on  $\text{MgO}(110)$  these numbers are  $\mu_0 M_r = 0.9$  T (due to a highly uniaxial grain distribution) and  $\mu_0 H_c = 3$  T, respectively. Sputter growth on Cr-buffered  $\text{MgO}(100)$  from multiple targets was performed, among others, by Fullerton et al. [124]. Using a pressure of  $5 \times 10^{-3}$  mbar, they reported square magnetization loops with  $\mu_0 H_c = 3.4$  T for a 30 nm film (decreasing to 1.2 T at 450 nm) but they did not give values for  $\mu_0 M_s$  or  $\mu_0 M_r$ .

For single alloy targets, somewhat surprisingly, no work has been reported using  $\text{MgO}$  substrates, probably since coercive fields of the order of a Tesla do not require such a substrate. Also, a mixture of Co, Fe, Cu, and Zr was often used rather than pure Co in order to enhance coercivity. One parameter which did vary in the different studies is the sputtering pressure, which will be noted in units  $10^{-3}$  mbar for easy comparison. A summary of the results, where we confine ourself to processes without post-annealing, is as follows.

Cadiou [93] reported on sputtering thin films using  $\text{Sm}_2(\text{Co,Fe,Zr,Cu})_{17}$  and  $\text{SmCo}_5$  targets on  $\text{Al}_2\text{O}_3$  substrates with a high sputter background pressure ( $80 \times 10^{-3}$  mbar), so that the sputtered atoms were thermalized when they arrive onto the substrate and support the growth of large crystallites. For  $\text{SmCo}_5$  he found  $\mu_0 H_c = 2.4$  T and  $\mu_0 M_r = 0.9$  T for a 3  $\mu\text{m}$  thick film with a (110) texture. In a different publication [122] he showed that with a varying sputter gas pressure (between  $20 \times 10^{-3}$  mbar and  $170 \times 10^{-3}$  mbar) and different sputter gasses (Ar, Xe and ArXe), it is possible to vary the Sm concentration of the film from a Sm atomic percentage of about 12 atomic % to 16 atomic %. These films have a typical coercive field of 0.7 T and a remanent magnetization of 0.8 T.

Neu [94] et al. studied the Co-rich part of the Sm-Co phase diagram.  $\text{Sm}(\text{CoFeCuZr})$  films were grown by cosputtering  $\text{Sm}(\text{Co,Fe,Cu,Zr})_7$  and  $\text{SmCo}_5$  targets on  $\text{Al}_2\text{O}_3$  substrates. They varied the sputter background pressure in the range of  $80 - 130 \times 10^{-3}$  mbar. The magnetic properties of these Sm-Co films grown at a constant pressure show a smooth increase in the coercive field when the Sm concentration is increased from 15 atomic % to 18.5 atomic % (with 16.7 atomic % corresponding to  $\text{SmCo}_5$ ). The remanent magnetization shows a smooth decrease, connected to the reduced amount of (Co,Fe). When the sputter background pressure is decreased from  $110 \times 10^{-3}$  mbar to  $80 \times 10^{-3}$  mbar, a clear increase in the coercive field and decrease in the remanent magnetization was observed, connected to a higher amount of Cu. The  $\text{Sm}(\text{Co,Fe,Cu,Zr})$  film that contained 15.8 atomic % Sm and was grown at  $80 \times 10^{-3}$  mbar had a coercive

field of 0.7 T and a remanent magnetization of 0.8 T.

Speliotis and Niarchos [96] sputtered Sm-Co films on Si substrates from an alloy target with 18 atomic % Sm. They discussed the magnetic properties of the Sm-Co films, when the sputter background pressure was varied between  $24 \times 10^{-3}$  mbar and  $32 \times 10^{-3}$  mbar. Again, when increasing the Sm concentration from 11 atomic % to 17 atomic %, the remanent magnetization decreases and the coercive field increases. The Sm-Co film that contained 15 atomic % Sm had a coercive field of 1.5 T and a remanent magnetization of 0.7 T.

Summarizing, sputtering from single alloy targets has primarily been studied using Si or  $\text{Al}_2\text{O}_3$  substrates under various conditions of pressure. The films typically show coercive fields of the order 0.7 T (and a maximum reported value of 2.4 T), and remanent fields of the order of 0.7 T – 0.8 T, as can be expected from the texturing. In our work we use a  $\text{SmCo}_5$  alloy target and  $\text{MgO}(001)$  single crystal substrates with a Cr buffer layer, and grow films in an Ar pressure range between  $1.5 \times 10^{-3}$  and  $12.5 \times 10^{-3}$  mbar. We are able to vary the Sm content of the films with pressure between 15 atomic % Sm and 27 atomic % Sm. At room temperature we find typical values for  $\mu_0 M_r$  of 0.4 T, somewhat lower than the above results; and values for  $\mu_0 H_c$  up to 3.3 T, higher than reported until now.

## 4.3.2 Results

### 4.3.2.1 Composition and morphology

Figure 4.6.a shows the XRD scans of films grown at  $1.5 \times 10^{-3}$  mbar ( $\text{SmCo}_5$ -like) and  $6.0 \times 10^{-3}$  mbar ( $\text{Sm}_2\text{Co}_7$ -like) respectively. The observed peaks are labeled as reflections of Sm-Co, MgO and Cr. Due to the thickness and high crystallinity, also the  $K_\beta$  peak of the MgO substrate is visible. In Figure 4.6.b the region around the Sm-Co(11 $\bar{2}$ 0) peak is shown, for films grown with a sputter pressure of 1.5, 3.0, 6.0 and  $9.0 \times 10^{-3}$  mbar. Clearly visible is that, with decreasing pressure, the peaks shift to a higher angle. The measured lattice constant, determined from the Sm-Co(22 $\bar{4}$ 0) peak, and the Sm content, determined by RBS, are plotted in Figure 4.7 as a function of the sputter pressure. For films grown at a pressure above  $6.0 \times 10^{-3}$  mbar, the lattice parameter of the Sm-Co film is almost that of bulk  $\text{Sm}_2\text{Co}_7$  (0.5040 nm). Decreasing the pressure from  $6.0 \times 10^{-3}$  mbar shows a decreasing lattice parameter, and at the lowest pressure the lattice constant of the Sm-Co film almost reaches the  $\text{SmCo}_5$  bulk value (0.4982 nm). With re-

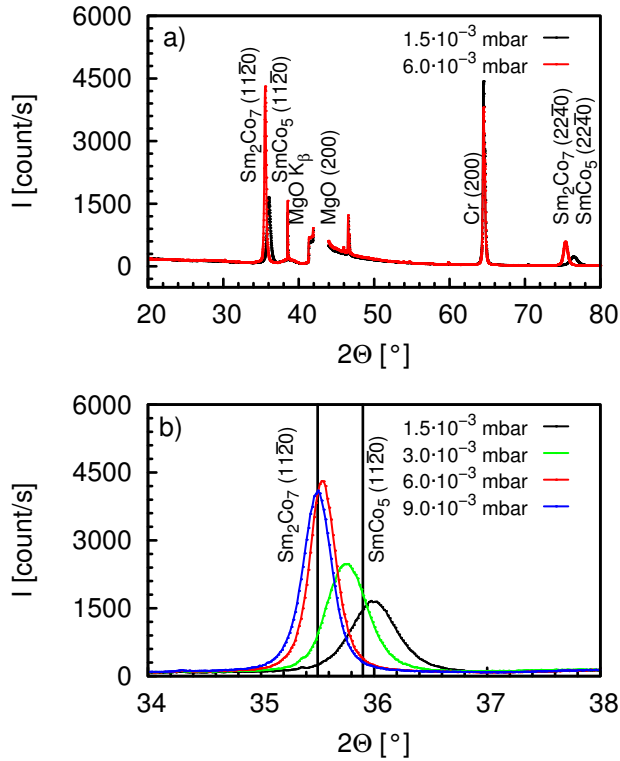


Figure 4.6: a) X-ray diffraction pattern ( $\theta$ - $2\theta$  scan) of Sm-Co films grown from an Sm-Co alloy target on a Cr/MgO(100) substrate with two different sputter gas pressures, as indicated. b) shows the region around the Sm-Co(11 $\bar{2}$ 0) peak, where the two vertical lines indicate the reflection of bulk crystalline  $\text{Sm}_2\text{Co}_7$  (left) and  $\text{SmCo}_5$  (right). Four samples are shown, grown at (from right to left), 1.5 (black), 3.0 (green), 6.0 (red) and  $9.0 \times 10^{-3}$  mbar (blue).



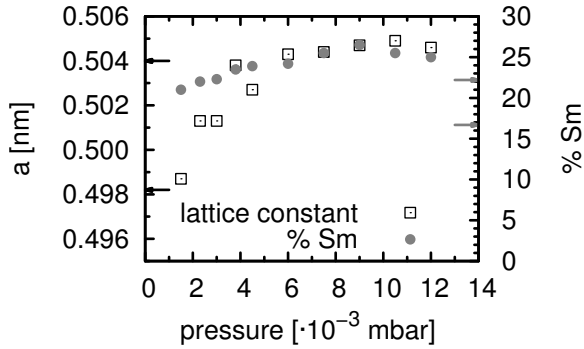


Figure 4.7: Lattice constant  $a$  of Sm-Co films and Sm concentration in the films as a function of the sputter background pressure, where the black ( $\leftarrow$ ) and gray ( $\rightarrow$ ) arrows indicate the lattice constant and Sm concentration of bulk  $\text{SmCo}_5$  and  $\text{Sm}_2\text{Co}_7$ . Clearly visible is the change of the lattice parameter  $a$  from the  $\text{Sm}_2\text{Co}_7$  phase ( $a = 0.5040$  nm) to the  $\text{SmCo}_5$  phase ( $a = 0.4982$  nm).

spect to the Sm concentration, we consistently find a somewhat higher number than the stoichiometric Sm-Co phases would yield. Above  $6.0 \times 10^{-3}$  mbar, the Sm concentration is around 25 - 27 atomic % (compared to 22 atomic % for  $\text{Sm}_2\text{Co}_7$ ). Below  $6.0 \times 10^{-3}$  mbar the Sm content gradually decreases to 21 atomic % (compared to 17 atomic % for  $\text{SmCo}_5$ ).

Figure 4.8.a - d show the morphology of the Sm-Co films grown at  $1.5$ ,  $3.0$ ,  $6.0$  and  $9.0 \times 10^{-3}$  mbar, respectively. The films grown at a high sputter background pressures consist of rectangular grains with an average size of  $70 \times 250 \text{ nm}^2$ , and with the long axis distributed over two orthogonal directions. Statistical analysis over an area of  $1 \times 1 \mu\text{m}^2$  on the Sm-Co film grown at  $6 \times 10^{-3}$  mbar indicates an average surface roughness of 8.1 nm and a peak to peak value of 57 nm. When decreasing the pressure below  $6 \times 10^{-3}$  mbar, the shape of the grains slowly transforms from rectangular to square-like. Sm-Co films grown at  $1.5 \times 10^{-3}$  mbar consist of square grains with an average size of  $75 \times 75 \text{ nm}^2$ . Statistical analysis over an area of  $1 \times 1 \mu\text{m}^2$  on the Sm-Co film grown at  $1.5 \times 10^{-3}$  mbar indicates an average surface roughness of 9.6 nm and a peak to peak value of 55 nm.

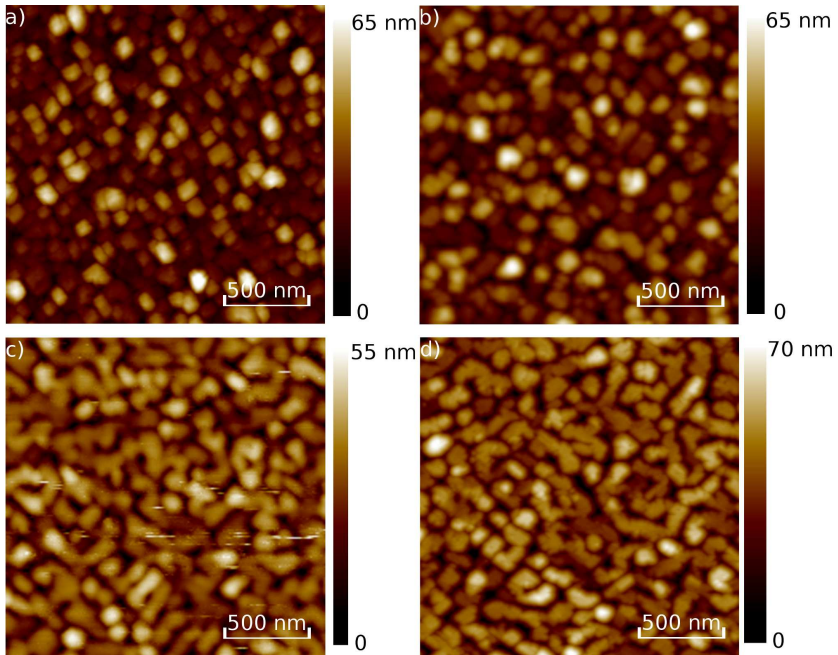


Figure 4.8: Morphology of Sm-Co films grown at a)  $1.5 \times 10^{-3}$ , b)  $3 \times 10^{-3}$ , c)  $6 \times 10^{-3}$  and d)  $9.0 \times 10^{-3}$  mbar measured with Atomic Force Microscopy.

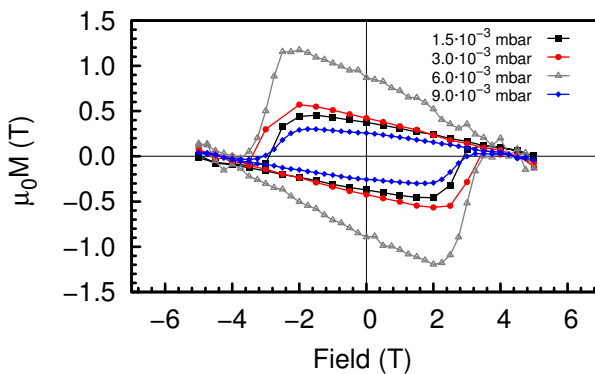


Figure 4.9: Magnetization  $\mu_0 M$  as function of magnetic field at 300 K for Sm-Co films on a Cr/MgO(100) substrate grown with different sputter gas pressures as indicated.

#### 4.3.2.2 Magnetic properties at room temperature

In Figure 4.9 the magnetization measurements are shown, taken at room temperature. The magnetization was calculated by dividing the measured magnetic moment by the measured volume of the Sm-Co films (typically  $10 \text{ mm} \times 4 \text{ mm} \times 100 \text{ nm}$ , where the Sm-Co thickness was determined using RBS). All samples show hysteretic behavior with a square-like loop and a large coercivity, of the order of 3 T, but also a substantial diamagnetic contribution. Separate measurements on an MgO(100) substrate and an MgO(100)/Cr(100 nm)/Cu(30 nm) film show that, at room temperature, the magnetic susceptibility  $\chi$  of MgO for substrates from different batches varied and the samples measured had a magnetic susceptibility of  $-2.4$  and  $-3.5 \times 10^{-7} \text{ emu/g}$ . These values are in agreement with  $\chi = -5.1 \times 10^{-7} \text{ emu/g}$  for a single crystal of MgO [125].

For the films grown at  $1.5$ ,  $3.0$  and  $9.0 \times 10^{-3} \text{ mbar}$ , the coercive fields  $\mu_0 H_c$  are 2.6, 3.0 and 2.6 T and the remanent magnetization  $\mu_0 M_{\text{rem}}$  are 0.4, 0.4 and 0.3 T. The film grown at  $6.0 \times 10^{-3} \text{ mbar}$  has a coercive field of 3.0 T and a significantly larger remanent magnetization of 0.87 T. Both  $\mu_0 H_c$  and  $\mu_0 M_{\text{rem}}$  as a function of sputter pressure are given in Figure 4.10. Again we find clear trends: with increasing pressure up to  $6 \times 10^{-3} \text{ mbar}$   $\mu_0 H_c$  slowly increases from 2.6 T to 3.3 T, but above  $6 \times 10^{-3} \text{ mbar}$  a rapid decrease sets in, down to 1.8 T at  $12 \times 10^{-3} \text{ mbar}$ . The remanent magnetization is 0.42 T - 0.25 T in the whole pressure range, with the single exception of one film grown at  $6.0 \times 10^{-3} \text{ mbar}$ , for which a value of 0.87 T is found. To characterize the magnetic texture, the ratio of the remanence of the in-plane and out-of-plane magnetization was determined for the films grown at 1.5 and  $6.0 \times 10^{-3} \text{ mbar}$  (not shown). These data show that both films have a preferred in-plane orientation of the easy axis.

#### 4.3.2.3 Target variability

One issue which came up during the research is target variability. We have grown Sm-Co films using a number of different commercially obtained targets with requested composition  $\text{SmCo}_5$ , which, according to the vendor, were fabricated from the same batch of alloy material. In Figure 4.11, the pressure dependence of the lattice constant of the Sm-Co films grown with three different targets is shown. The data discussed above were from films grown with target 1. Clearly visible is that the lattice parameters and therefore the exact film composition varies for the different targets. For target 2, the lattice parameters do not

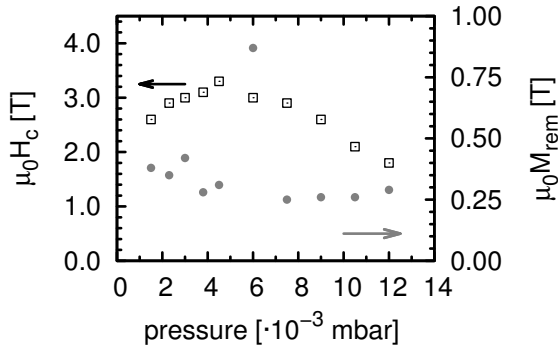


Figure 4.10: The coercive field  $\mu_0 H_c$  and the remanent magnetization  $\mu_0 M_{\text{rem}}$  at 300 K of the Sm-Co films as a function of the sputter background pressure.

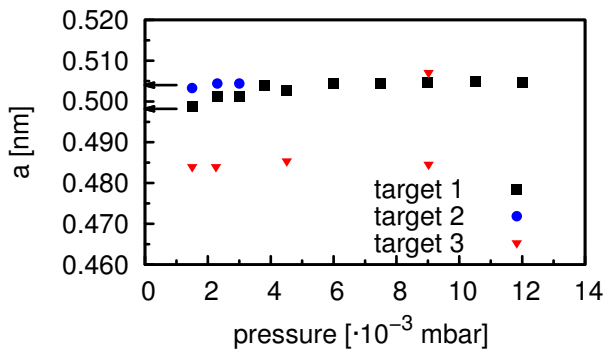


Figure 4.11: The lattice constant  $a$  of the Sm-Co films, grown with three different composite targets that were fabricated from the same batch of alloy material, as a function of the sputter background pressure. The black ( $\leftarrow$ ) arrows indicate the lattice constant of bulk  $\text{SmCo}_5$  and  $\text{Sm}_2\text{Co}_7$ . The two lattice constants at  $9.0 \times 10^{-3}$  mbar for target 3 indicates that there are two phases present in the film.

decrease when going to low pressure, which indicates a slight excess of Sm with respect to target 1. Films from target 3 show a considerably lower lattice parameter (typically 1 %) and apparently contain much more Co, although the lattice parameter is still lower than what is expected for the  $\text{Sm}_2\text{Co}_{17}$  compound (0.419 nm). The films grown with targets 2 and 3 showed coercive fields which were generally lower, between 1.0 and 2.0 T. We did not attempt to optimize the magnetic properties by varying the growth temperature.

#### 4.3.2.4 Magnetic properties at low temperatures

We also investigated the low temperature behavior of the Sm-Co films. In Figure 4.12, the uncorrected magnetization hysteresis loops for a Sm-Co film grown at  $10.5 \times 10^{-3}$  mbar are shown as a function of temperature. For temperatures down to 30 K, the coercive field and the remanent magnetization increase slowly. Also, the diamagnetic contribution of the substrate becomes smaller. When going to even lower temperatures, the hysteresis loop shows a clear paramagnetic behavior. Figure 4.13.a shows magnetization measurements for two MgO substrates from different batches at 4 K, which are clearly paramagnetic in character. Electron paramagnetic resonance (EPR) measurements were done to identify the paramagnetic impurities. Figure 4.13.b shows the room temperature EPR measurements of a MgO substrate. Clearly visible are the resonance lines of  $\text{Cr}^{3+}$ ,  $\text{V}^{2+}$  and  $\text{Mn}^{2+}$  impurities [126]. In Figure 4.14, the uncorrected and corrected magnetization hysteresis loops at 4.2 K for a Sm-Co film grown at  $2.3 \times 10^{-3}$  mbar are shown. For this measurement we added a Cu capping layer to the MgO/Cr film in order to preclude an unwanted contribution from oxidized Cr. Clearly visible is that the uncorrected loop is a minor loop, where the remanent magnetization for both the positive and negative field sweep has the same high and positive value. The magnetization hysteresis loop is corrected by subtracting the magnetization of the impurities. The corrected hysteresis loop is almost field independent, showing that the coercive field is larger than 5 T.

### 4.3.3 Discussion

Summarizing the experimental findings for target 1, we see that, when varying the sputter background pressure between  $1.5 \times 10^{-3}$  and  $12.5 \times 10^{-3}$  mbar, the Sm concentration in the films varies between 21 and 26.5 at%. In the whole pressure range, we find the Sm content of the films higher than expected from the stoichiometric ratio's of the line compounds. Appar-

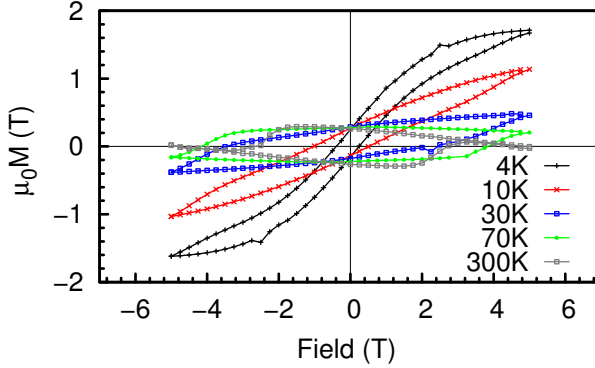


Figure 4.12: a) Magnetization  $\mu_0 M$  as function of magnetic field of the Sm-Co film grown at  $10.5 \times 10^{-3}$  mbar as a function of temperature. For the 10 K and 4 K loop, the 5 T magnet of the magnetometer is not strong enough to reach the coercive field of the Sm-Co film while the contribution of the MgO substrate increases significantly.

ently, the sputter process does not result in a well-defined composition. In particular, the films are not a mixture of the  $\text{SmCo}_5$  and  $\text{Sm}_2\text{Co}_7$  compounds, which would result in two lines with different weight in the X-ray data. Rather, the films consist of one main composition which is able to incorporate a varying amount of Co-atoms. This is in line with the picture of Kahn [105], who proposed that the crystal structure of the intermetallic compounds can be seen as a one-dimensional superstructure of the  $\text{CaCu}_5$ -type structure, where in each  $i$ -th  $\text{CaCu}_5$ -type structure a Co-atom is replaced by a Sm-atom. Khan described this structure with the general formula  $\text{SmCo}_y$ , where  $y$  is equal to  $(5n + 4)/(n + 2)$  (with  $n$  an integer). According to the XRD data, at the lowest pressure the films are close to the  $\text{SmCo}_5$  compound, going to  $\text{Sm}_2\text{Co}_7$  at higher pressures. With increasing sputter pressure, both the lattice constant and the value for  $\mu_0 H_c$  increases until the pressure of  $6.0 \times 10^{-3}$  mbar is reached, where the lattice parameter corresponds to the  $\text{Sm}_2\text{Co}_7$  alloy (although still with Sm excess). At the same time,  $\mu_0 M_{\text{rem}}$  slowly decreases from about 0.4 T to 0.3 T. Increasing the pressure further,  $\mu_0 H_c$  starts to decrease while  $\mu_0 M_{\text{rem}}$  becomes constant. The surface morphology in Figure 4.8 shows that the grain size and grain shape changes when the sputter pressure is changed. At high pressures, relatively large rectangular grains are grown. When reducing the pressure,

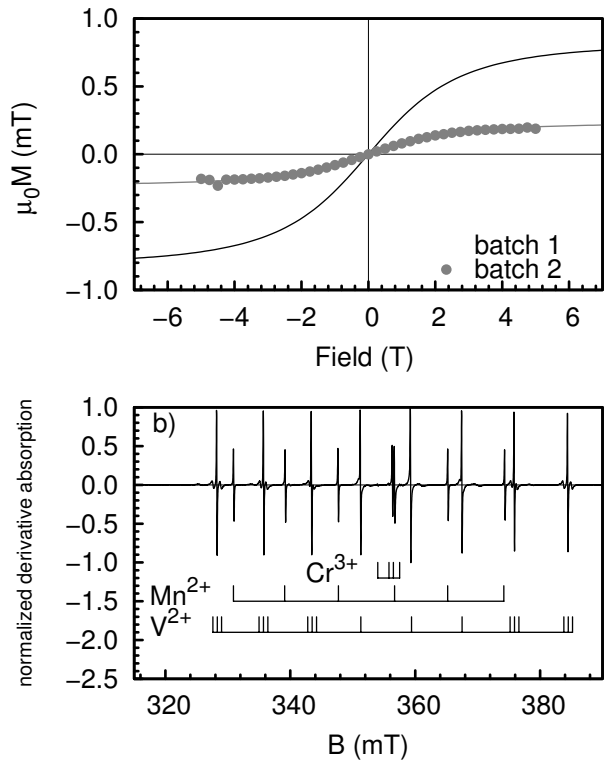


Figure 4.13: a) Magnetization  $\mu_0 M$  as function of magnetic field for two MgO substrates from different batches measured at 4 K. The solid lines are fits to a Brillouin function using  $\text{Cr}^{3+}$ ,  $\text{Mn}^{2+}$  and  $\text{V}^{2+}$  impurities. b) A typical room temperature EPR spectrum of a MgO single crystal substrate containing  $\text{Cr}^{3+}$ ,  $\text{Mn}^{2+}$  and  $\text{V}^{2+}$  impurities.

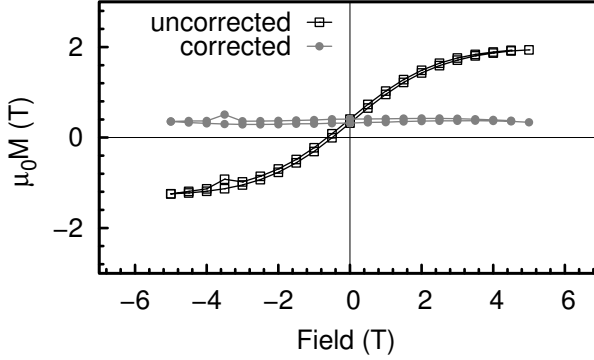


Figure 4.14: Magnetization  $\mu_0 M$  as function of magnetic field (black squares) of the Sm-Co film grown at  $2.3 \times 10^{-3}$  mbar measured at 4.2K. The gray dots are the values for  $\mu_0 M$  after correction for the substrate contribution. A small hysteresis characteristic of a minor loop is visible.

the grains become smaller and more square-like. We surmise this is due to the change in average energy of the atoms bombarding the substrate: at low pressure, this energy is higher and as a result, more defects are created during the growth of the first Sm-Co layers. When the number of defects becomes larger, also the number of preferred nucleation sites increases. The increase in the number of nucleation sites results in a reduced grain size and a more rough surface.

Connecting the structure/morphology data to the magnetization data, we see that in the range of pressures where the films change from  $\text{SmCo}_5$ -like to  $\text{Sm}_2\text{Co}_7$ -like, the values of  $\mu_0 H_c$  (2.6 T – 3.3 T) and  $\mu_0 M_{\text{rem}}$  (0.4 T – 0.3 T) are the highest, and in particular  $\mu_0 H_c$  is close to what has been achieved with cosputtering.  $\mu_0 M_{\text{rem}}$  is lower than optimal. For an equal distribution of two easy axes, the expected value is  $\mu_0 M_s / \sqrt{2}$ , or 0.78 T both for  $\text{SmCo}_5$  and for  $\text{Sm}_2\text{Co}_7$  [127]. This is in agreement with Ref. [115] where it was shown that excess of Sm leads to a significant decrease of  $\mu_0 M_{\text{rem}}$ . The films grown above  $6.0 \times 10^{-3}$  mbar show a decrease in coercive field, although the Sm concentration, lattice constant and remanent magnetization do not change significantly with respect to the films grown at lower pressures. We attribute the change in coercive field to the larger grain size of the grown Sm-Co film. In experiments with nanoparticles with a different size, it was found that the size has a significant influence on the coercive field and an optimum particle size is approximately 100 – 200 nm [128]. The large remanent



magnetization of 0.87 T for the film grown at  $6.0 \times 10^{-3}$  mbar is an anomaly which is difficult to explain. In principle, either a strongly uniaxial texture could yield such a value close to the saturation magnetization, or a small grain size with strong exchange coupling between spins in the grain boundary area [129] but the morphology of the film does not point in such directions.

At low temperatures, the picture is somewhat complicated by the paramagnetic behavior of the MgO substrates, which is due to transition metal impurities, in particular Mn, V, and Cr. Their amount varies from batch to batch. Up to now, not much attention has been paid to the influence of the transition metal impurities on the properties of the grown films. Recently, the influence of the transition metal impurities on the optical and magnetic properties of a bare MgO substrate were studied [130]. Since the low temperature magnetic hysteresis shows a clear paramagnetic behavior superimposed on it, we assume that the magnetization  $\mu_0 M_{\text{imp}}$  of these impurities can be described by the Brillouin function

$$\begin{aligned} \mu_0 M_{\text{imp}} = & N g J \mu_B \frac{2J+1}{2J} \coth \left( \frac{2J+1}{2J} \frac{g J \mu_B J B}{k_b T} \right) \\ & - N g J \mu_B \frac{1}{2J} \coth \left( \frac{1}{2J} \frac{g J \mu_B J B}{k_b T} \right) \end{aligned} \quad (4.1)$$

with  $N$  the number of atoms,  $g$  the  $g$ -factor,  $\mu_B$  the Bohr magneton,  $J$  the total angular momentum,  $k_B$  Boltzman constant and  $T$  the temperature. The total magnetization for the three different impurities is then modeled as the sum of the magnetization of each type of impurities. From fitting equation 4.1 to the low temperature magnetization of a bare MgO substrate, we estimate that in the MgO substrates in Figure 4.13(a), the concentration of the impurities is in the range of 15–60 ppm [130]. When the contribution of the impurities in the MgO substrate is subtracted using equation 4.1, the Sm-Co film shows an almost constant magnetization as shown in Figure 4.14. The measured magnetic hysteresis loop is not the hysteresis loop itself, but a minor loop, since the coercive field is larger than the 5 T which can be reached in the magnetometer.

#### 4.3.4 Conclusion sputtering single alloy target

When growing SmCo films from a single target with the nominal composition of SmCo<sub>5</sub> target on a Cr-buffered MgO(100) substrate, high

coercive fields can be reached, up to 3.3 T. In order to avoid low remanence, excess Sm has to be avoided. Although in principle the Sm content can be varied using the sputter pressure, the amount of control depends on the sputtering configuration. In the case described here, the lowest pressure at which we could grow films appears to be too high for this goal. A Co-rich target might be a solution for this problem. However, another difficulty we encountered was the high sensitivity of the film properties to different targets of nominally the same composition, which requires relatively costly optimization of the deposition conditions for each target separately. Targets with a composition closer to one of the line compounds in the phase diagram might be better suited to the purpose of single target sputtering, but this issue requires more research. At low temperatures we achieved the high coercive fields characteristic for these hard magnetic materials, but we also found that the data are strongly dominated by paramagnetic impurities in the MgO substrates.

#### 4.4 Sm-Co thin films grown by cosputtering Sm and Co

The growth of Sm-Co thin films by sputter deposition from an alloy Sm-Co target looks an attractive way to grow thin films with a high coercive field and saturation magnetization. The big problem encountered above is the exact target composition. Our experience shows that with a target with the right composition very good films can be grown, but that a slight offset of the right composition changes the film properties dramatically. To overcome this problem, we also have grown films using sputter deposition from the single elemental targets Sm and Co.

Furthermore, growing Sm-Co films on MgO(100) substrates results in the epitaxial relation  $\text{Sm-Co}(11\bar{2}0)[0001] \parallel \text{Cr}(001)[110] \parallel \text{MgO}(001)[100]$ , where in the film the Sm-Co grains are equally distributed along the two in-plane directions. This is not the ideal case for the fabrication of nanostructures, because it is unknown if the device is located at a grain where the magnetization is parallel or perpendicular to the grain. Therefore also the growth of Sm-Co thin films on MgO(110) substrates is studied. MgO(110) has the epitaxial relation  $\text{Sm-Co}(10\bar{1}0)[0001] \parallel \text{Cr}(211)[0\bar{1}1] \parallel \text{MgO}(110)[001]$ . In this way, all grains are oriented in the same direction.

In this section, it is shown that we can grow Sm-Co films by cosputtering from elemental Sm and Co targets. We also show that, when growing Sm-Co films on an MgO(100) substrate and varying the Sm concentration, we can grow films that can incorporate a varying amount

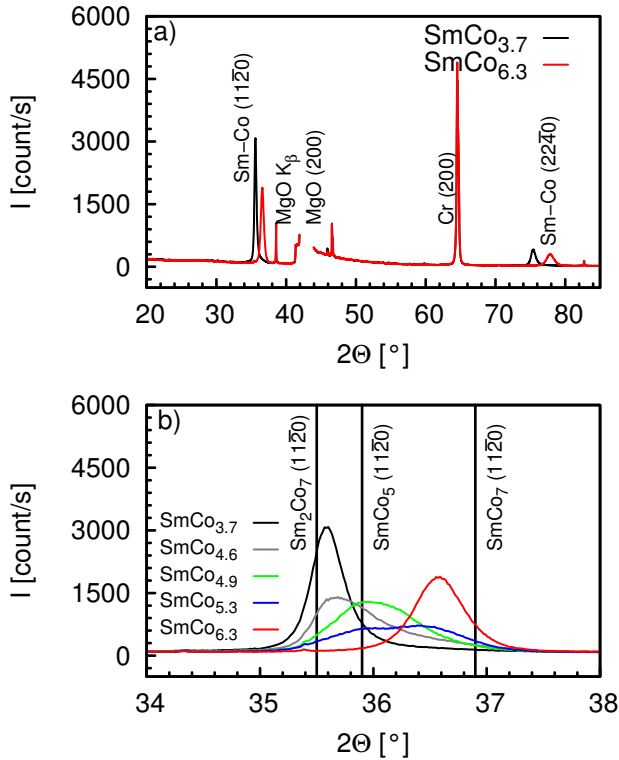


Figure 4.15: a)  $\theta$ - $2\theta$  XRD scans of Sm-Co films grown by cosputtering from single elemental Sm and Co targets on a Cr/MgO(100) substrate with different levels of Sm sputter power and constant Co sputter power (except SmCo<sub>5.3</sub>). b) shows the region around the Sm-Co(1120) peak, where the three vertical lines indicate the reflection of bulk crystalline Sm<sub>2</sub>Co<sub>7</sub> (left), SmCo<sub>5</sub> (middle) and SmCo<sub>7</sub> (right). The nominal Sm/Co ratios are indicated.

of Co atoms. However, on an MgO(110) substrate we always grow multiple well-defined phases, where the Sm<sub>2</sub>Co<sub>7</sub> and Sm<sub>2</sub>Co<sub>17</sub> phase are more easy to grow.

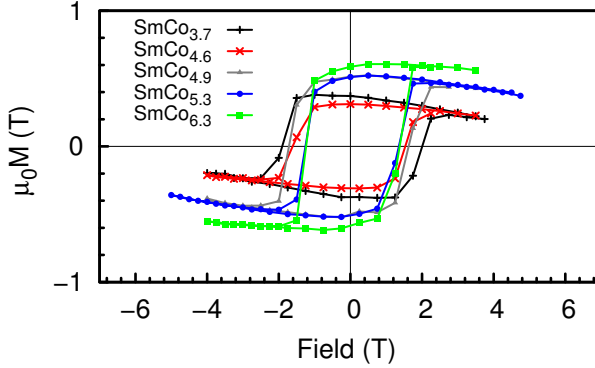


Figure 4.16: Uncorrected magnetic hysteresis of the Sm-Co films on a Cr/MgO(100) substrate grown with different Sm sputter powers at 300 K.

## 4.4.1 Results

### 4.4.1.1 Sm-Co films on MgO(100)

Figure 4.15.a shows the XRD scans of Sm-Co films grown on MgO(100) substrate with different compositions. The compositions have been changed by varying the Sm sputter power from 30 mA Sm ( $\text{SmCo}_{6.3}$ ) up to 50 mA Sm ( $\text{SmCo}_{3.7}$ ) and keeping the Co sputter power constant at 150 mA or 155 mA. The observed peaks are labeled as reflections of Sm-Co, Cr and MgO. Due to the thickness and high crystallinity, also the  $K_\beta$  peak of the MgO substrate is visible. In Figure 4.15.b, the region around the Sm-Co(11 $\bar{2}$ 0) peak is shown:  $\text{SmCo}_{6.3}$  (30 mA Sm, 150 mA Co),  $\text{SmCo}_{5.3}$  (37 mA Sm, 155 mA Co),  $\text{SmCo}_{4.9}$  (37 mA Sm, 150 mA Co),  $\text{SmCo}_{4.6}$  (40 mA Sm, 150 mA Co) and  $\text{SmCo}_{3.7}$  (50 mA Sm, 150 mA Co). Clearly visible is that with an increasing Sm sputter current, the peak shifts to a smaller angle. Furthermore, for films with a Sm concentrations around 16 – 17%, the shape of the peak changes from a sharp single peak to a broad double peak.

In Figure 4.16, the uncorrected magnetization measurements are shown. The  $\text{SmCo}_{3.7}$  and  $\text{SmCo}_{4.6}$ -films show a square-like loop with a coercive field  $\mu_0 H_c$  between 1.5 and 2.0 T and a remanent magnetization  $\mu_0 M_{\text{rem}}$  between 0.33 and 0.45 T. The  $\text{SmCo}_{4.9}$ ,  $\text{SmCo}_{5.3}$  and  $\text{SmCo}_{6.3}$  films have a more rounded hysteresis loop with lower coercive fields than the Sm-rich films, but  $\mu_0 M_{\text{rem}}$  is larger than the Sm-rich films. Both  $\mu_0 M_{\text{rem}}$  and  $\mu_0 H_c$  are plotted as a function of the Sm con-

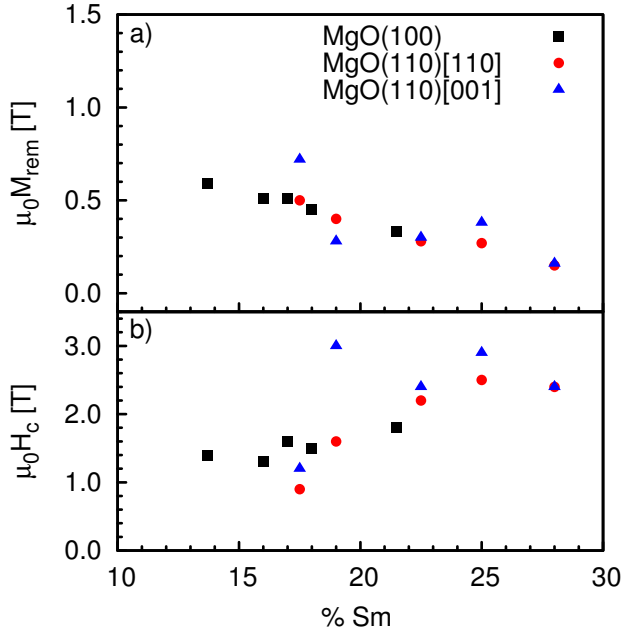


Figure 4.17: The remanent magnetization  $\mu_0 M_{rem}$  (a) and the coercive field  $\mu_0 H_c$  (b) of the Sm-Co films on MgO(100) (black ■) and MgO(110) substrates for different Sm concentrations. The field is oriented in the film plane in all cases, and along the [110]-direction (red ●) and [001]-direction (blue ▲) for the MgO(110) substrates.

centration in Figure 4.17. With increasing Sm content,  $\mu_0 H_c$  becomes larger, but  $\mu_0 M_{rem}$  decreases smoothly.

Figure 4.18 shows the morphology of the Sm-Co films. The  $\text{SmCo}_{4.6}$  (a) and  $\text{SmCo}_{4.9}$  (b) film consist of rectangular grains. When increasing the Sm concentration, the  $\text{SmCo}_{5.3}$  film consists of clusters of small round grains and the  $\text{SmCo}_6$ -film becomes a very smooth, roughness is 2 nm, almost closed film, where no grains are visible.

#### 4.4.1.2 Sm-Co films on MgO(110)

In Figure 4.19, the XRD scan of Sm-Co films grown on MgO(110)/Cr substrates with a different Sm concentration are shown. The compositions have been changed by varying the Co sputter rate from 115 mA ( $\text{SmCo}_{2.6}$ ) up to 190 mA Co ( $\text{SmCo}_{4.7}$ ) and keeping the Sm sputter

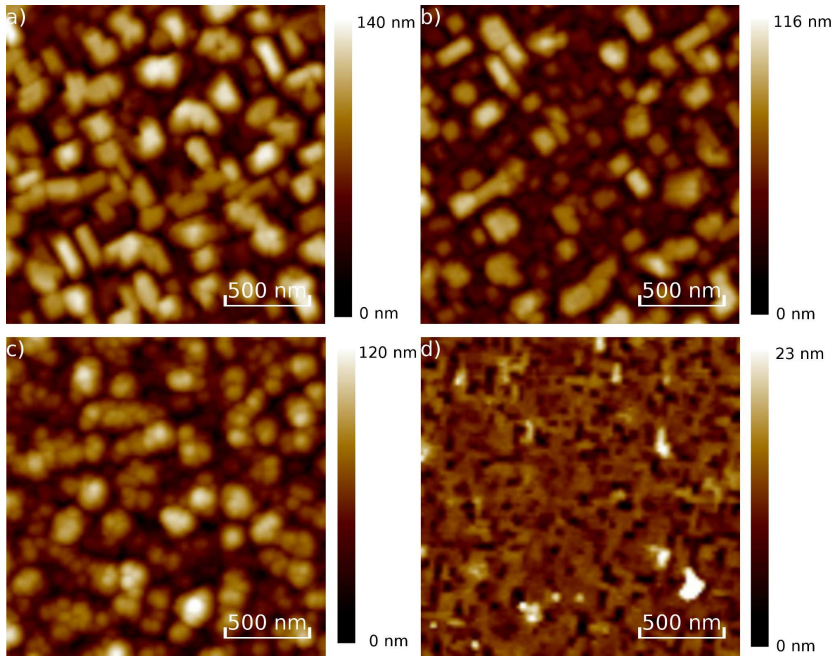


Figure 4.18: Morphology of the Sm-Co films grown on MgO(100) measured with atomic force microscopy, where a) is a  $\text{SmCo}_{4.6}$  film with a roughness of 19 nm, b) is a  $\text{SmCo}_{4.9}$  film with a roughness of 16 nm, c) is a  $\text{SmCo}_{5.3}$  film with a roughness of 13 nm and d) is a  $\text{SmCo}_{6.3}$  film with a roughness of 2 nm.

rate constant at 50 mA. The observed peaks are labeled as reflections of Sm-Co, Cr and MgO. Whereas the Cr layer on MgO(100) grows as the cubic (100) phase, on MgO(110) Cr grows as the monoclinic Cr(211) phase. Figure 4.19.b shows the region around the Sm-Co(200) peak, for Sm-Co films with a different composition:  $\text{SmCo}_{2.6}$  (115 mA Co),  $\text{SmCo}_{3.0}$  (130 mA Co),  $\text{SmCo}_{3.4}$  (145 mA Co),  $\text{SmCo}_{4.3}$  (175 mA Co) and  $\text{SmCo}_{4.7}$  (190 mA Co). Clearly visible, is that all the films show diffraction peaks at the  $\text{Sm}_2\text{Co}_7$ ,  $\text{SmCo}_5$  and  $\text{Sm}_2\text{Co}_{17}$  phases. The  $\text{SmCo}_{2.6}$  film consists mainly of the  $\text{Sm}_2\text{Co}_7$  phase and a small amount of the  $\text{SmCo}_5$  phase. When increasing the Co concentration, the  $\text{Sm}_2\text{Co}_7$  and the  $\text{SmCo}_5$  phase in the film diminishes and the  $\text{SmCo}_7$  or  $\text{Sm}_2\text{Co}_{17}$  phase becomes the dominant phase in the film.

In Figure 4.20, the uncorrected magnetization measurements of the

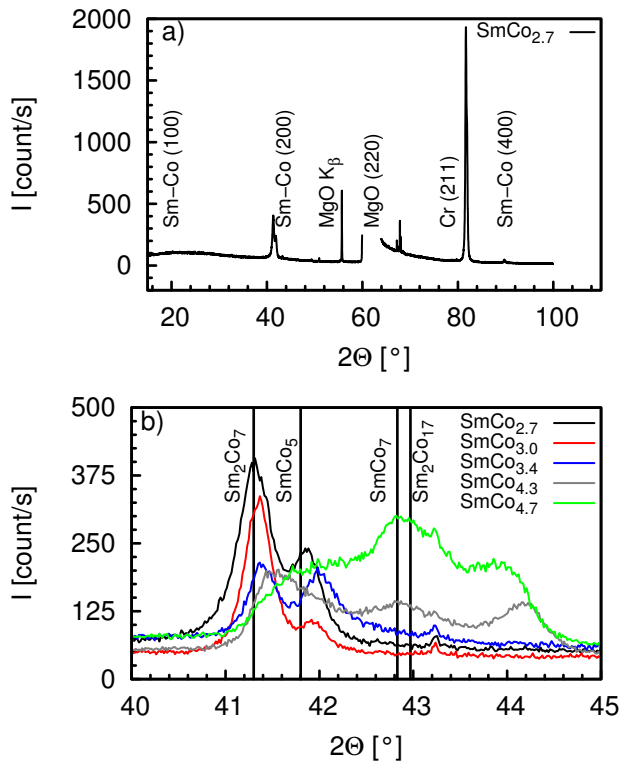


Figure 4.19:  $\theta$ - $2\theta$  XRD scans of Sm-Co films grown by cosputtering from single elemental Sm and Co targets on a Cr/MgO(110) substrate with different sputter power levels. b) shows the region around the Sm-Co(200) peak, where the three vertical lines indicate the reflections for bulk crystalline Sm<sub>2</sub>Co<sub>7</sub> (left), SmCo<sub>5</sub> (middle left), SmCo<sub>7</sub> (middle right) and Sm<sub>2</sub>Co<sub>17</sub> (right).

Sm-Co films on MgO(110) are shown. The  $\text{SmCo}_{4.7}$  film has a large remanent magnetization of 0.50 T in the MgO[110]-direction and a remanent magnetization of 0.72 T in the MgO[001]-direction. With an increasing Sm concentration, the remanent magnetization decreases in both the [110] and [001]-direction. The coercive field behaves in the opposite way. The  $\text{SmCo}_{4.7}$  film has a coercive field of 0.9 T in the MgO[110]-direction and 1.2 T in the MgO[001]-direction. With an increasing Sm concentration, the coercive field increases in both directions, as can be seen clearly in Figures 4.17 and 4.20.

The morphology of the Sm-Co films grown on MgO(110) is shown in Figure 4.21. The crystal structure looks quite different from the morphology of the Sm-Co films grown on MgO(100). While the films on MgO(100) grow as big crystallites for the Sm-rich films, on MgO(110) it looks as if the crystallites are grouped as rows of small grains, as is clearly visible in Figure 4.21.a. When increasing the Co concentration, the grains in the rows become larger and there are less grains in a row. For the  $\text{SmCo}_{4.7}$  film, the grains becomes smaller again and there are more grains in a row.

## 4.4.2 Discussion

### 4.4.2.1 Sm-Co films on MgO(100)

When varying the sputter current, the composition and phase of the Sm-Co thin films on MgO(100)/Cr can be controlled as is shown in Figure 4.15. The composition can be varied more or less continuously and the XRD scans show the high sensitivity to changes of the sputter rate. The optimum  $\text{SmCo}_5$  films are grown with a Sm source current of 37 mA, while a difference of 1 mA (0.05 nm/min or 2-3 % Sm) is already clearly visible. When increasing the Sm concentration by increasing the Sm source current, the  $\text{Sm}_2\text{Co}_7$  and  $\text{SmCo}_5$  phases are both grown, as can be seen from the two peaks in the XRD scan. This growth behaviour is different from the growth from an alloy target, which tends to form either the  $\text{Sm}_2\text{Co}_7$  or the  $\text{SmCo}_5$  phase, as was shown in Section 4.3. When increasing the Sm concentration even further, single phase  $\text{Sm}_2\text{Co}_7$  films can be grown at 50 mA Sm sputter current.

Still, the magnetic properties of the Sm-Co films on MgO(100) show the expected behaviour. Co-rich films have a smaller coercive field, but a larger remanent magnetization. When increasing the Sm concentration,  $\mu_0 M_{\text{rem}}$  becomes smaller and  $\mu_0 H_c$  becomes larger. However, the Sm-Co films do not show the really large coercive fields that can be expected for this type of films. The main difference between the films



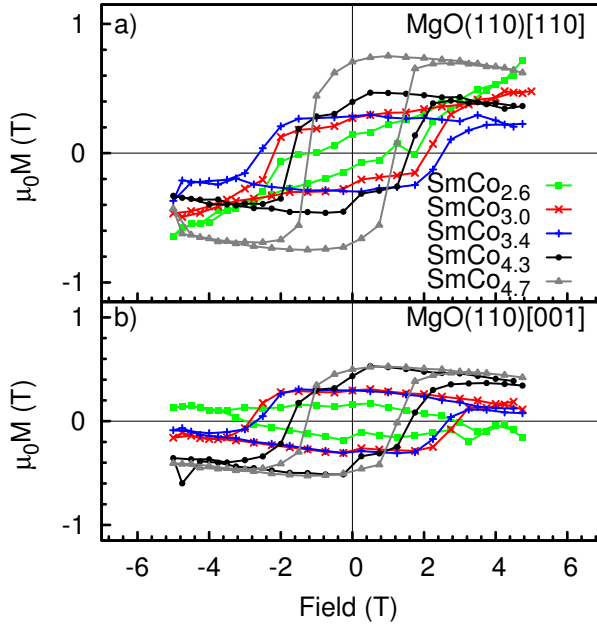


Figure 4.20: Uncorrected magnetic hysteresis of the Sm-Co films on a Cr/MgO(110) substrate with the field applied in the MgO(110)[110] (a) and MgO(110)[001] (b) direction, grown with different Co sputter powers levels at 300K.

grown using sputter deposition from an alloy target and cosputtering is the size of the Sm-Co grains. It has been recently shown that the grain size significantly affects the coercivity [128]. In Figure 4.8, atomic force microscopy images show that the grains of the Sm-Co films grown from the alloy target are much bigger than the grains from the Sm-Co films grown by cosputtering. Furthermore, a constant sputter gas pressure was used for the cosputter growth of the Sm-Co films, while the sputter gas pressure is an important parameter for the growth of Sm-Co films, as was shown in Section 4.3.

#### 4.4.2.2 Sm-Co films on MgO(110)

The XRD scans of the films on grown on MgO(110) are more complicated. Always a mixture of the  $\text{Sm}_2\text{Co}_7$ ,  $\text{Sm}_2\text{Co}_{17}$ ,  $\text{SmCo}_5$  and/or  $\text{SmCo}_7$  phases is grown. From the Sm-Co phase diagram, it is clear that

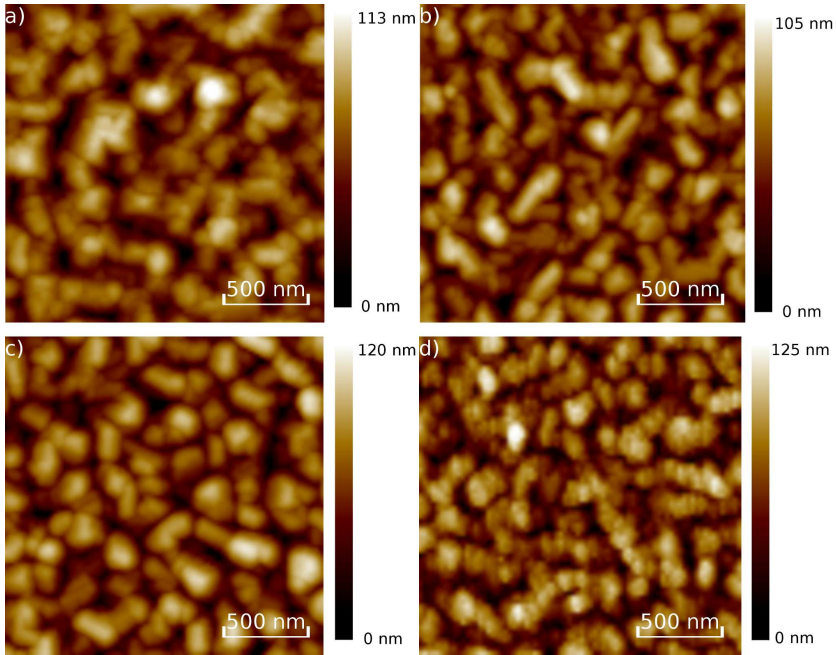


Figure 4.21: Morphology of the Sm-Co films grown on MgO(110) measured with atomic force microscopy, a) is a  $\text{SmCo}_{3.0}$  film with a roughness of 16 nm, b) is a  $\text{SmCo}_{3.4}$  film with a roughness of 18 nm, c) is a  $\text{SmCo}_{4.3}$  film with a roughness of 19 nm and d) is a  $\text{SmCo}_{4.7}$  film with a roughness of 19 nm.

$\text{SmCo}_5$  is not a stable line compound, and it lies close to two other alloys;  $\text{Sm}_2\text{Co}_7$  on the Sm-rich side and  $\text{SmCo}_7$  on the Sm-poor side. Apparently, the growth process on this surface is very delicate and does not easily result in a well-defined single phase; minor changes in composition change the growth significantly.

The magnetic properties of the grown Sm-Co films on MgO(110) show a large coercive field at room temperature. Values  $\mu_0 M_{\text{rem}}$  and  $\mu_0 H_c$  as a function of the Sm concentration, as shown in Figure 4.17, show the expected behaviour. However, the magnetization measurements along the MgO(110)[110], do not show the expected hard axis behaviour, which indicates that the film does not grow only along the expected MgO[001] axis. This is also visible in the surface morphology, as shown in Figure 4.21. The grains appear randomly distributed on

the surface and are not aligned in one direction.

For the growth of the Sm-Co films on the MgO(110) substrates, the same temperature and constant Ar background sputter pressures was used for the growth of the Sm-Co films on the MgO(100) substrates. We expect that the growth of a single phase Sm-Co film with an easy axis along the MgO[001] direction, would be very sensitive to the exact growth parameters like temperature and sputter gas pressure.

To conclude, by varying the sputter current of the Sm and/or Co target, we can change the phase for the Sm-Co alloy from a SmCo<sub>5</sub>-like to the Sm<sub>2</sub>Co<sub>7</sub>-like phase, when the film is grown on MgO(100). When the Sm-Co film is grown on MgO(110), the Sm-Co film consists of multiple phases where the amount of each phase depends on the sputter power. We find that the film composition is extremely sensitive to small variation in sputterpower levels. The films grown on MgO(100) and MgO(110) have good magnetic properties, but the crystal texture of the films on MgO(110) does not show the expected two-fold symmetry.



# Temperature dependence of the Gilbert damping in thin Co/Pt bilayers

## 5.1 Introduction

In this Chapter, we measure the spin transport between a ferromagnet (F) and a normal metal (N) using the spin pump technique, that was introduced in Chapter 2. When a ferromagnet is capped with an adjacent metal layer and brought into ferromagnetic resonance, the ferromagnet emits a spin current into that layer. From such spin pumping experiments, we can derive the spin mixing conductance  $G^{\uparrow\downarrow}$  which is an interface property, and which is a measure for the amount of injected spin current into the adjacent layer. Consequently, the experiment shows whether it is possible at all to inject a spin current.

Originally, we were interested to know whether spin can be transferred to and from a Sm-Co layer and study which properties plays a crucial role in the spin torque and spin pumping phenomena. However, we will use Co thin films which have been capped with the normal metals Pt or Cu to get around the growth related issues of the Sm-Co thin films, which were discussed in the previous Chapter. We are particularly interested in the temperature dependence of the spin transfer by spin pumping, which until now received little attention.

We measure spin pumping using the ferromagnet resonance (FMR) technique, which will be discussed in Section 5.2. Spin pumping can be seen as an extra contribution to the damping and thereby to the linewidth in an FMR experiment if the adjacent layer efficiently removes ('sinks') the spin. Pt is a good spin sink, because the high charge of the nucleus gives rise to strong spin-orbit scattering. This is much less for Cu, which is assumed to be a 'bad' spin sink and can serve as a reference. As discussed in Chapter 2, the basic signature of the spin pumping effect in F/N bilayers is that its contribution to the damping increases inversely proportional to the F-layer thickness. As will be shown below, this can be observed in particular for thicknesses below 10 nm. In our experiments, we typically used values for the thickness of the F-layer between 1 and 20 nm.

Besides the contribution of spin pumping, many other processes contribute to the damping. They can be intrinsic, due to the band-structure of the material; or extrinsic, caused by inhomogeneities. The first part of this Chapter is concerned with these various processes. Section 5.2 also shows how measurements of the dependence of the linewidth on the angle between the applied magnetic field and the film normal can be used to extract the damping contribution from inhomogeneities, such as the roughness or a spread in the directions of crystalline axes.

Section 5.3 is devoted to intrinsic contributions to the linewidth such as spin-orbit relaxation or inter- and intraband scattering. Section 5.4 gives the experimental details and in Section 5.5, the room temperature FMR characterization and analysis is presented. Spin pumping in the Pt layer can also be detected electrically by the spin Hall effect. This is shown and discussed in Section 5.6. Sections 5.7 and 5.8 present the low temperature conductance and FMR characterization of the Co/Pt bilayers. At low temperatures, we find the same thickness dependence as was observed at room temperature. In Section 5.9, the last section, a full discussion of the data is given.

One note should be made with respect to units. In order to connect better to the existing literature in this field, the choice has been made to present the data in cgs units, rather than in the SI units used in Chapter 4.

## 5.2 Ferromagnetic resonance in thin magnetic films

The dynamics of the precession of the magnetization can be studied using the ferromagnetic resonance (FMR) technique [131, 132]. From

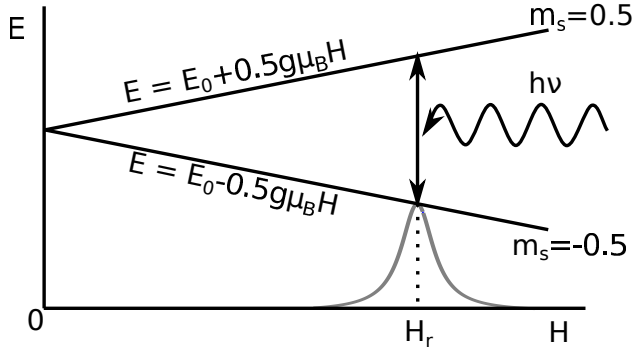


Figure 5.1: Basic principle of EPR and FMR. The degenerate states are split by an external static magnetic field. An applied radio frequency magnetic field can induce a transition between the two states when the resonance condition is fulfilled.

FMR spectra, static and dynamic properties of (ultra)thin magnetic layers can be obtained. From the value of the resonance field in the FMR spectra static magnetic properties such as the  $g$ -factor and the magnetic anisotropies can be found. From the FMR linewidth, the magnetic homogeneity and the damping parameter for the magnetization precession can be obtained.

### 5.2.1 The resonance field

The FMR technique is similar to the electron paramagnetic resonance (EPR) or the nuclear magnetic resonance (NMR) technique. Consider first a single ion with a magnetic dipole with a magnetic moment  $\mu$  equal to  $\mu = \gamma\hbar\mathbf{L}$ , where  $\gamma = g\mu_B/\hbar$  is the gyromagnetic ratio. When this magnetic dipole is placed in a static magnetic field  $\mathbf{H}$  the corresponding energy  $E$  is equal to

$E = -\mu \cdot \mathbf{H}$ . When  $\mathbf{H}$  points in the  $(0,0,H)$ -direction, the energy of the ion is equal to  $E = -\gamma\hbar m_s H_0$ , where  $m_s$  is the spin quantum number and equal to  $\pm 0.5$  for an electron.

When irradiating the dipole with a radio frequency (RF) magnetic field  $\mathbf{H}_1$  perpendicular to  $\mathbf{H}$ , the RF field with frequency  $\nu$  can induce a transition between both states if the resonance condition

$$h\nu = 2g\mu_B|m_s|H_r, \quad (5.1)$$

is fulfilled as shown in Figure 5.1.

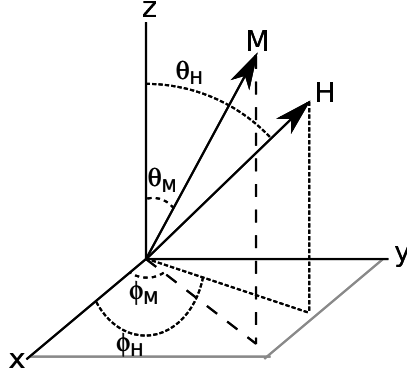


Figure 5.2: The coordinate system used for the analysis of the FMR data. The thin film lies in the  $xy$ -plane and the magnetization  $\mathbf{M}$  of the film points in the  $\mathbf{M}$ -direction. The applied DC magnetic field  $\mathbf{H}$  points in the  $\mathbf{H}$ -direction.

In a ferromagnet, the total magnetic moment of the sample can be considered as one macrospin  $\mathbf{M}$ , which precesses around the local static field  $\mathbf{H}$  at the Larmor frequency  $\omega_L = \gamma \mathbf{H}$ . The macrospin  $\mathbf{M}$  behaves in the same way as the single ion in a static magnetic field, when irradiated with a RF magnetic field, but the ferromagnetic resonance condition is now given by the Smit-Beljars-Suhl equation [133, 134]

$$\frac{\omega}{\gamma} = \frac{1}{M_s \sin \theta_M} \sqrt{\frac{\partial^2 F}{\partial \theta_M^2} \frac{\partial^2 F}{\partial \phi_M^2} - \left( \frac{\partial^2 F}{\partial \theta_M \phi_M} \right)^2}. \quad (5.2)$$

The angles  $\theta_{H/M}$  and  $\phi_{H/M}$  are the polar and azimuthal angles of the DC magnetic field  $\mathbf{H}$  and the magnetization  $\mathbf{M}$  with respect to the  $z$ - and  $x$ -axis, respectively. The coordinate system is shown in Figure 5.2.  $F$  is the total energy per unit volume of magnetization and is modeled for a thin film by

$$F = -\mathbf{M} \cdot \mathbf{H} + 2\pi(\mathbf{M} \cdot \mathbf{n})^2 - K\left(\mathbf{M} \cdot \frac{\mathbf{u}}{M_s}\right)^2. \quad (5.3)$$

Here the first term is the Zeeman energy, the second term the demagnetization energy and the third term the uniaxial anisotropy term, with  $K$  the magnetic anisotropy constant,  $M_s$  the saturation magnetization and  $\mathbf{n}$  and  $\mathbf{u}$  the unit vectors normal to the surface of the sample and oriented along the easy axis of the sample, respectively. The



applied magnetic field  $\mathbf{H}$  and the magnetization  $\mathbf{M}$  of the sample can then be written as

$$\mathbf{H} = H(\sin \theta_H \cos \phi_H, \sin \theta_H \sin \phi_H, \cos \theta_H) \quad (5.4)$$

$$\mathbf{M} = M_s(\sin \theta_M \cos \phi_M, \sin \theta_M \sin \phi_M, \cos \theta_M). \quad (5.5)$$

Combining equation (5.3) and (5.2) for the perpendicular anisotropy case ( $\mathbf{n} = \mathbf{u} = [001]$ ), the ferromagnetic resonance condition is

$$\left(\frac{\omega}{\gamma}\right)^2 = [H_r \cos(\theta_H - \theta_M) - 4\pi M_{\text{eff}} \cos^2 \theta_M] \times [H_r \cos(\theta_H - \theta_M) - 4\pi M_{\text{eff}} \cos 2\theta_M]. \quad (5.6)$$

Here  $4\pi M_{\text{eff}} = 4\pi M_s - H_{\perp}$  is the effective demagnetization field and  $H_{\perp} = 2K_{\perp}/M_s$  the perpendicular anisotropy field. The values for  $\theta_M$  and  $\phi_M$  on resonance can be determined by the condition  $\partial F/\partial \theta_M = 0$  and  $\partial F/\partial \phi_M = 0$ ;  $\theta_M$  on resonance is then given by

$$\sin(2\theta_M) = \frac{2H_r}{4\pi M_s - H_{\perp}} \sin(\theta_M - \theta_H). \quad (5.7)$$

From equation 5.6, it follows that the resonance conditions, for in-plane and out-of-plane magnetic fields, where  $\theta_M = \theta_H$ , are equal to

$$\omega = \gamma(H_r - 4\pi M_{\text{eff}}) \quad \text{out-of-plane} \quad (5.8)$$

$$\omega = \gamma\sqrt{H_r(H_r + 4\pi M_{\text{eff}})} \quad \text{in-plane.} \quad (5.9)$$

## 5.2.2 The linewidth

The linewidth of the FMR spectrum has two sources; intrinsic relaxation of the magnetization that is characterized by the Gilbert damping constant  $\alpha$  and a relaxation of the magnetization due to sample inhomogeneities. The angular dependence of the FMR spectrum helps to identify the dominant relaxation mechanisms. The in-plane peak-to-peak linewidth  $\Delta H_{\text{pp}}^{\parallel}$  and out-of-plane peak-to-peak linewidth  $\Delta H_{\text{pp}}^{\perp}$  give clear evidence of the type of damping contributions [135].

Intrinsic relaxation of the magnetization, through mechanisms that will be discussed in the next section, leads to a *homogeneous* broadening of the linewidth  $\Delta H_{\text{pp}}^{\text{homo}}$ , which is given by [134]

$$\Delta H_{\text{pp}}^{\text{homo}} = \frac{1}{\sqrt{3}} \frac{\alpha}{M_s} \left( \frac{\partial^2 F}{\partial \theta_M^2} + \frac{1}{\sin^2 \theta_M} \frac{\partial^2 F}{\partial \phi_M^2} \right) \left| \frac{d(\omega/\gamma)}{dH_R} \right|^{-1}. \quad (5.10)$$

In this case,  $\Delta H_{\text{pp}}^{\parallel}$  is equal to  $\Delta H_{\text{pp}}^{\perp}$ .

Sample inhomogeneities can contribute significantly to the damping of the ferromagnet. The extra damping due to the sample inhomogeneities can be described by the so-called local resonance model with inhomogeneous broadening due to spatial variations in the spread of the crystallographic axis in the  $\theta_H$ -direction  $\Delta(\theta_H)$  and spatial variations of the demagnetization field  $\Delta(4\pi M_{\text{eff}})$ . This case is encountered for thin films with a perpendicular surface anisotropy or for polycrystalline multilayers. The inhomogeneous linewidth broadening  $\Delta H_{\text{pp}}^{\text{inhomo}}$  can be described as [136, 137]

$$\Delta H_{\text{pp}}^{\text{inhomo}} = \frac{1}{\sqrt{3}} \left| \frac{dH_r}{d(4\pi M_{\text{eff}})} \right| \Delta(4\pi M_{\text{eff}}) + \frac{1}{\sqrt{3}} \left| \frac{dH_r}{d\theta_H} \right| \Delta(\theta_H), \quad (5.11)$$

where  $|dH_r/d(4\pi M_{\text{eff}})|$  and  $|dH_r/d\theta_H|$  are deduced from equations 5.6 and 5.7. The total measured linewidth is then the sum of the homogeneous and inhomogeneous linewidth. In this case,  $\Delta H_{\text{pp}}^{\parallel}$  is smaller than  $\Delta H_{\text{pp}}^{\perp}$ .

Finally, when  $\Delta H_{\text{pp}}^{\parallel}$  is larger than  $\Delta H_{\text{pp}}^{\perp}$ , the intrinsic Gilbert damping and an extrinsic two-magnon scattering process are sufficient to describe the experimental data. This case is usually encountered in (ultra)thin films with a good structural order.

### 5.3 Damping in thin magnetic films

The Gilbert damping is the timescale at which the magnetization aligns with the effective magnetic field  $H_{\text{eff}}$ . The relaxation can take place in two different ways as shown in Figure 5.3: either the spin angular momentum is transferred to non-magnetic degrees of freedom, which is called direct damping; or the spin angular momentum is transferred to other magnetic degrees of freedom such as spin waves, which is called indirect damping. Significant relaxation processes in thin ferromagnetic films [138] are spin-orbit relaxation damping, two-magnon scattering and eddy current damping, which will be discussed in the next sections.

The temperature dependence of the Gilbert damping  $\alpha$  is an almost unexplored area. To our knowledge, Bhagat et al. [42, 139–141] in the nineteen-sixties and -seventies measured the damping of single-crystal whiskers of Co, Fe and Ni using FMR. In the seventies, Heinrich et al. measured the low temperature damping in Ni [142]. They observed that the Gilbert damping is not a monotonously increasing or decreasing

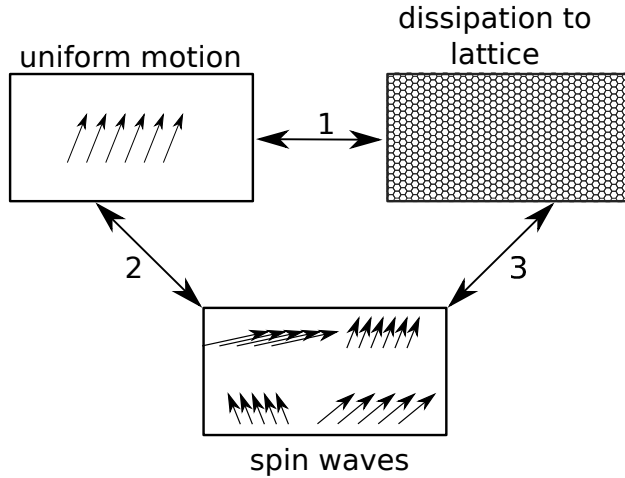


Figure 5.3: Ferromagnetic resonance excites a uniform precession mode in a ferromagnet, that can relax via a direct (path 1) and indirect (via path 2 + 3) relaxation channel. When the relaxation happens via the indirect relaxation channel, energy is transferred to spin waves.

ing function, but that a clear maximum is observed at a finite temperature.

In F/N hybrid structures, Yakata et al. studied the temperature dependence of the spin diffusion length in Cu for multilayer structures Cu/Ni<sub>80</sub>Fe<sub>20</sub>/Cu(*d*) and Cu/Ni<sub>80</sub>Fe<sub>20</sub>/Cu(*d*)/Pt [143] using the spin pumping technique. Furthermore, Czeschka et al. used also the spin pumping technique to measure the inverse spin Hall voltage of Fe/Pt and Co/Pt thin films [70] and thereby the spin mixing conductance down to low temperatures.

### 5.3.1 Spin-orbit relaxation damping

In 1967, Kamberský showed [68, 144, 145] that the intrinsic Gilbert damping can be described using a torque-correlation model. A clear introduction to the temperature dependence, which we will follow here, can be found in the thesis of Gilmore [146] and the review of Fähnle and Illg [69]. They used an effective field approach, to provide a better picture of the physical processes involved.

When the spin-orbit interaction is not negligible,  $\mathbf{S}$  and  $\mathbf{L}$  are no good quantum numbers anymore, because the spin-orbit interaction

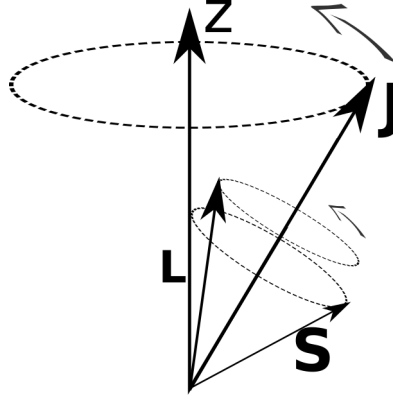


Figure 5.4: The orbital  $\mathbf{L}$  and spin  $\mathbf{S}$  angular momentum precess around the precessing total angular momentum  $\mathbf{J}$ .

is proportional to  $\mathbf{L} \cdot \mathbf{S}$ . The orbital and spin angular momenta exert a torque on each other, that cause them to precess about a resultant vector  $\mathbf{J}$ , the total angular momentum. As shown in Figure 5.4, the total angular momentum  $\mathbf{J}$  precesses and the spin and orbital momentum precesses around  $\mathbf{J}$ .

As  $\mathbf{J}$ , and therefore also the magnetization  $\mathbf{M}$  precesses, the energies of the states change through variations in the spin-orbit contribution and transitions between states take place. This creates an effective field  $\mathbf{H}^{\text{eff, damping}}$  [146]

$$\mathbf{H}^{\text{eff, damping}} = -\frac{1}{\mu_0|\mathbf{M}|} \sum_{n\mathbf{k}} \left[ \rho_{n\mathbf{k}} \frac{\partial \epsilon_{n\mathbf{k}}}{\partial \mathbf{m}} + \frac{\partial \rho_{n\mathbf{k}}}{\partial \mathbf{m}} \epsilon_{n\mathbf{k}} \right], \quad (5.12)$$

where  $\epsilon_{n\mathbf{k}}$  is the electron energy with a band index  $n$  and spin wavevector  $\mathbf{k}$ ,  $\rho_{n\mathbf{k}}$  is the occupation number and  $\mathbf{m}$  the unit direction vector of the magnetization  $\mathbf{M}$ .

The first term between brackets is the variation in the spin-orbit energies as the magnetization changes direction. This effect is normally referred to as the breathing Fermi surface model and gives rise to *intra*band scattering. The second term between brackets accounts for changes in the effective field due to transitions between states and is normally called the bubbling Fermi surface model and gives rise to the *inter*band scattering.

### 5.3.1.1 Intraband scattering

When the magnetization precesses, it generates a time-dependent spin-orbit coupling that can push some occupied states from just below the Fermi energy to above the Fermi energy and vice versa.

In the relaxation time approximation [146]  $\rho_{n\mathbf{k}}$  can be written as

$$\rho_{n\mathbf{k}} = f_{n\mathbf{k}} - \tau \frac{df_{n\mathbf{k}}}{dt}, \quad (5.13)$$

where  $f_{n\mathbf{k}}$  is the equilibrium Fermi-Dirac occupation and  $\tau$  determines how fast an electron-hole pair relaxes back to an equilibrium state. In the limit  $\tau \rightarrow 0$ , the electrons are scattered so often that the electronic system is always in the ground state. In Figure 5.5.a, this corresponds to the case where at time  $t - dt$  only states in  $S(t - dt)$  are occupied and at time  $t$  only states in  $S(t)$  are occupied.

With a finite relaxation time  $\tau$ , the scattering processes are not able at each time to create an equilibrium situation for the electronic system and the equilibrium occupation number lags behind the real occupation number. So it could happen that states that should be empty at time  $t$  are still occupied and that states that should be occupied are still empty, due to the time lag of the real occupation number. As shown in Figure 5.5.b, this time lag gives rise to the creation of electron-hole pairs.

The intraband damping rate is then equal to [146]

$$\alpha = \tau \frac{\gamma}{\mu_0 M_s} \sum_{n\mathbf{k}} \left( -\frac{df_{n\mathbf{k}}}{d\epsilon_{n\mathbf{k}}} \right) \left( \frac{\partial \epsilon_{n\mathbf{k}}}{\partial \mathbf{m}} \right)^2. \quad (5.14)$$

The damping is proportional to  $\tau$ , like the electrical Drude conductivity. The intraband scattering is therefore called conductivity-like. In Figure 5.6, the contribution of the intraband scattering for Co along different crystallographic directions is shown with dashed lines.

### 5.3.1.2 Interband scattering

When the magnetization precesses, it generates a time-dependent spin-orbit coupling. This coupling acts as a time-dependent perturbation that can cause a transition between the states  $\psi_{n\mathbf{k}}$  and  $\psi_{l\mathbf{k}}$  as shown in Figure 5.5.b. The initial and final state have the same wavevector  $\mathbf{k}$ , since in FMR experiments the uniform,  $\mathbf{k} = 0$ , mode is excited. Using Fermi's golden rule, the transition rate between states  $\psi_{n\mathbf{k}}$  and  $\psi_{l\mathbf{k}}$  can be calculated.

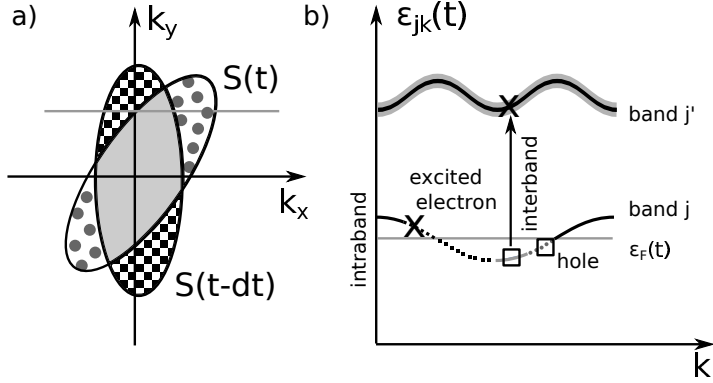


Figure 5.5: a) Sketch of the equilibrium Fermi surface  $S$ , taken to be an ellipsoid in this example, at time  $t$  ( $S(t)$ , gray dotted part + light gray center part) and time  $t - dt$  ( $S(t - dt)$ , black squares + light gray middle part). For fast relaxation, the light gray states are occupied the whole time while at time  $t$  only the dotted states are occupied and at time  $t - dt$  only the squared states are occupied. b) Sketch of the equilibrium band  $\epsilon_{jk}$  along the horizontal gray line in a). In a realistic situation, the occupation number lags behind the Fermi-Dirac distribution function and at time  $t$ , some states in the squared Fermi surface are still occupied and some states in the dotted part are still empty. The excited electron-hole pair will relax via an intraband transition. Reprinted with permission from [147]. ©(2010) by the American Physical Society.

The interband damping rate is then equal to [146]

$$\alpha = \frac{\gamma}{2\mu_0 M_s} \sum_{nk} \sum_{l \neq n} W_{ln}(\mathbf{k}) \frac{[\rho_{nk} - \rho_{lk}]}{\omega} \frac{[\epsilon_{lk} - \epsilon_{nk}]}{\omega} \quad (5.15)$$

where  $\omega$  is the precession frequency and  $W_{ln}(\mathbf{k})$  is the transition rate between states  $\psi_{nk}$  and  $\psi_{lk}$  and equal to

$$W_{ln}(\mathbf{k}) = \frac{2\pi}{\hbar} \left| 2 \left( \frac{\partial \epsilon_{nk}}{\partial \mathbf{m}} \right)^2 \right|^2 \delta(\epsilon_{lk} - \epsilon_{nk} - \hbar\omega). \quad (5.16)$$

There is an energy gap  $\Delta\epsilon$  between the states  $\psi_{nk}$  and  $\psi_{lk}$ . When  $\Delta\epsilon > \hbar/\tau$ , the Gilbert damping is proportional to  $1/\tau$  and scales as the resis-

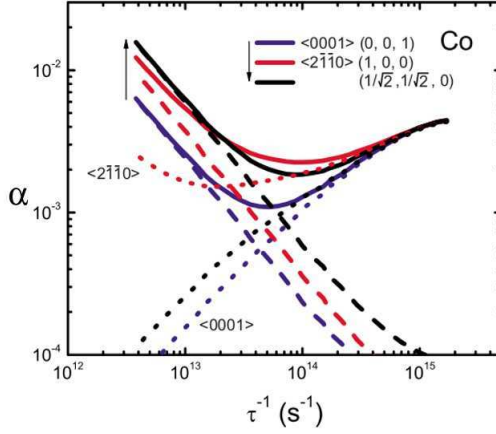


Figure 5.6: Calculated Gilbert damping  $\alpha$  for Co. The dotted lines indicate the contribution of the interband scattering to the total scattering, whereas the dashed lines indicate the contribution of the intraband scattering. Figure reprinted with permission from [148]. ©(2007) by the American Physical Society.

tivity. In Figure 5.6, the contribution of the interband scattering for Co along different crystallographic directions is shown with dotted lines.

### 5.3.2 Other mechanism

The relaxation of a uniform precession mode in a ferromagnet can also happen via indirect damping. The two-magnon process [149] is an example of an indirect damping process, as shown in Figure 5.3. Here, the uniform precession mode ( $\mathbf{k} = 0$ ) scatters into non-uniform modes ( $\mathbf{k} \neq 0$ ).

The damping can also be influenced by eddy currents [138]. Eddy current damping,  $\alpha_{\text{eddy}}$  is proportional to

$$\alpha_{\text{eddy}} \propto \gamma M_s \sigma d^2, \quad (5.17)$$

where  $\sigma$  is the electrical conductivity,  $d$  the film thickness and  $M_s$  the saturation magnetization.

## 5.4 Experimental

The Co( $d$ )/Pt(10) and Co( $d$ )/Cu(10) films, where  $d$  is varying and all thicknesses are in nm, were deposited on oxidized Si(100) in a UHV chamber (base pressure  $1 \times 10^{-9}$  mbar) using DC magnetron sputter deposition with argon as plasma at room temperature from 3N5 Co, 3N5 Cu and 3N5 Pt targets. Since the thickness of the Cu- and Pt-layers are not going to be varied and to take into account both interfaces of the Co layer, we call them SiO<sub>x</sub>/Co( $d$ )/Cu and SiO<sub>x</sub>/Co( $d$ )/Pt. The deposition rate was measured by X-ray reflectivity (XRR) using Cu-K $\alpha$  radiation and was 0.58 Å/s for Co, 1.90 Å/s for Cu and 1.54 Å/s for Pt respectively. Values of  $d$  ranged from 1.5 nm to 50 nm.

Magnetization measurements were performed in a SQUID-based magnetometer (MPMS 5S from Quantum Design). For electrical characterization, the samples were patterned into Hall bar structures,  $50 \times 1000 \mu\text{m}^2$ , using negative resist, electron beam lithography and ion beam etching. Resistivity measurements were performed using the resistivity option with an excitation current of 100  $\mu\text{A}$  in a Physical Properties Measurement System (Quantum Design).

FMR was measured using a Bruker EMXplus X-band spectrometer, see Figure 5.7.a, in a TE<sub>011</sub> cavity with a maximum DC-field of 0.6 T or with a Bruker E680 ElexSys 9.5 in a TE<sub>102</sub> cavity with a maximum DC-field of 1.5 T. The  $2.4 \times 2.4 \text{ mm}^2$  samples were glued with silverpaint

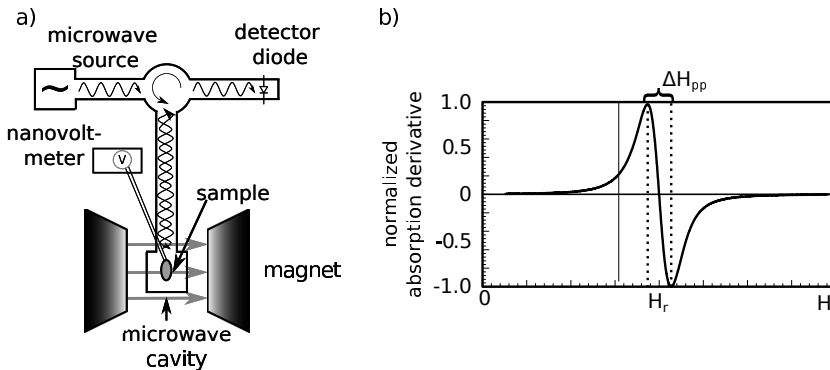


Figure 5.7: a) Schematic of an EPR/FMR measurement set-up. b) FMR spectrum where the normalized derivative absorption is plotted as a function of the applied static magnetic field  $H$ , with a resonance field  $H_r$  and a peak-to-peak linewidth  $\Delta H_{pp}$ .



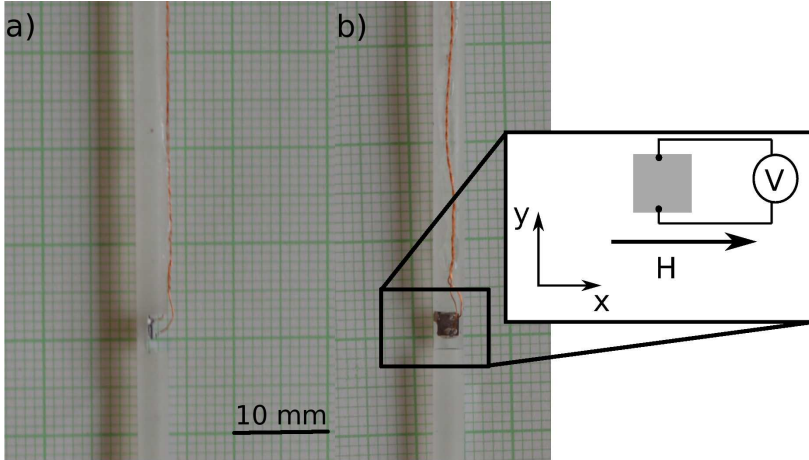


Figure 5.8: Side view (a) and front view (b) of a  $2.4 \times 2.4 \text{ mm}^2$  sample mounted on a Rexolite sampleholder with wires glued to the sample for ISHE measurements. The inset shows the orientation of the magnetic field with respect to the sample and the position of the electrical contacts to measure the ISH voltage.

in a notch of a Rexolite 1422 rod as shown in Figure 5.8. The notch was made into the rod, to align the sample on the rotation axis of the rod and in the middle of the cavity. A goniometer was used to rotate the rod in the cavity and to vary the angle  $\theta_H$  between the applied magnetic field and the film normal. Most measurements were done with 100 kHz modulation frequency and 1 Gauss modulation amplitude. For low temperature measurements, a He flow cryostat was used. The flow cryostat consist of a double walled, vacuum insulated quartz tube that fits in the microwave cavity. The sampleholder is placed into the quartz tube, where just below the sample a thermometer and heater are mounted.

Using cavity based-FMR, the frequency is fixed and the static magnetic field is swept to fulfill the resonance condition. A typical FMR spectrum is shown in Figure 5.7.b. Due to field modulation in combination with lock-in detection, not the microwave absorption is measured, but its first derivative. The peak-to-peak linewidth  $\Delta H_{pp}$  is the difference between the maximum and minimum intensity of the absorption derivative.  $\Delta H_{pp}$  is related to the full width half maximum  $\Delta H$  of the Lorentzian absorption profile as  $\sqrt{3}\Delta H_{pp} = \Delta H$  [150]. The resonance

field  $H_r$  is the applied magnetic field  $H$ , where the resonance condition is fulfilled. This is visible in the FMR spectrum as the applied field where the absorption derivative is equal to 0.

When also the inverse spin Hall (ISH) voltage was measured, twisted Cu wires were glued with silverpaint, see Figure 5.8.c, to the sample and the ISH voltage was measured using a Keithley 2182a nanovoltmeter.

## 5.5 FMR measurements

In Figure 5.9, the raw FMR spectra of a  $\text{SiO}_x/\text{Co}(2)/\text{Pt}$  bilayer are plotted for different applied field directions  $\theta_H$ . For an in-plane applied magnetic field ( $\theta_H = 90^\circ$ ), the resonance condition is fulfilled in a small magnetic field and the peak-to-peak linewidth is very narrow. When rotating the sample slowly to the out-of-plane magnetic field configuration ( $\theta_H = 0^\circ$ ), larger magnetic fields are required to fulfill the resonance condition and  $\Delta H_{\text{pp}}$  becomes larger. When the applied field direction is almost in the out-of-plane configuration ( $\theta_H = 0^\circ$ ), the peak-to-peak linewidth becomes again more narrow. As can be seen in Figure 5.9, we are not able to obtain a full FMR spectrum, for  $\theta_H$  smaller than  $2^\circ$ . The background that appears for the high-field FMR spectra is due to the magnetostriction, which modifies the cavity properties a little bit.

In Figure 5.10.a, the measured and fitted angular dependence of the resonance field of a  $\text{SiO}_x/\text{Co}(2)/\text{Pt}$  bilayer is plotted. The angu-

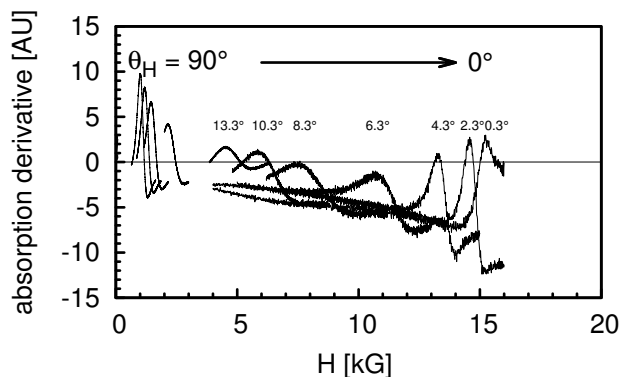


Figure 5.9: Angular dependence of the FMR spectrum of a  $\text{SiO}_x/\text{Co}(2)/\text{Pt}$  bilayer for  $\theta_H = 90^\circ$  to  $0^\circ$ . For clarity, the angular dependence from  $\theta_H = 0^\circ$  to  $-90^\circ$  is not plotted.

lar dependence has a peak at  $\theta_H = 0^\circ$ . The two dotted lines indicate the maximum DC magnetic field the two electromagnets can produce. It should be noted that the actual resonance field at  $0^\circ$  is too large for the 0.6 T and 1.5 T magnet to be measured. Using equations 5.2 and 5.6, the resonance field can be fitted as a function of  $\theta_H$ . As we are not able to measure the full angular dependence, we fit each curve with a number of g-factors between 1.8 and 2.2. From the fits we extract the average, minimum and maximum value of  $4\pi M_{\text{eff}}$  and we obtain for each g-value the angular dependence of the magnetization direction  $\theta_M(\theta_H)$ . The range for the g-value is chosen between the bulk value for Co, 2.2, and the best fitting g-value for the  $\text{SiO}_x/\text{Co}(2)/\text{Pt}$  bilayer, 1.8. A g-value of 1.8 may appear to be low, but both the induced orbital magnetization and the spin pumping effect decrease the g-value. The spin  $\mu_s$  and orbital  $\mu_l$  magnetic moments are related to the g-factor via  $|g-2|/2 = \mu_l/\mu_s$  [151]. An induced orbital magnetization will then also change the g-factor. Furthermore, Zhang et al. [152] found using FMR experiments in  $\text{Si}/\text{Ru}/20\times[\text{Co}(25 \text{ \AA}) + \text{Pt}(d)]/\text{Pt}$  multilayers, that for a varying Pt thickness  $d$ , the g-value varied between 1.83 and 2.30.

In Figure 5.10.b, the fitted angular dependence of  $\theta_M$  is plotted for the  $\text{SiO}_x/\text{Co}(2)/\text{Pt}$  bilayer with a g-value of 1.8. The magnetization direction does not follow directly the direction of the applied magnetic field. From  $\theta_H$  equal to  $90^\circ$  to almost  $10^\circ$ , the magnetization of the Co film stays in-plane. Around  $10^\circ$ , a sudden change from an in-plane to an out-of-plane magnetization takes place. In Figure 5.10.c, the measured and fitted peak-to-peak linewidth  $\Delta H_{\text{pp}}$  is shown, which exhibits sharp peaks around  $\theta_H = \pm 10^\circ$ , which corresponds to the change of magnetization direction from in-plane to out-of-plane and a minimum at  $\theta_H = 0^\circ$ . Furthermore,  $\Delta H_{\text{pp}}$  at  $\theta_H$  at  $0^\circ$  is larger than  $\Delta H_{\text{pp}}$  at  $90^\circ$ . Using the fitted values for  $H_r$  and  $\theta_M$ , and equations 5.10 and 5.11, also  $\Delta H_{\text{pp}}$  can be fitted. From the fits of  $\Delta H_{\text{pp}}$ , we extract the average, minimum and maximum values of  $\alpha$ ,  $\Delta(\theta_H)$  and  $\Delta(4\pi M_{\text{eff}})$ .

The angular dependences of the three distinct contributions to the total measured peak-to-peak linewidth are different, as can be seen in Figure 5.10.c. For an in-plane applied magnetic field ( $\theta_H = 90^\circ$ ), the contributions of the Gilbert damping and the spatial variation in the demagnetization field have almost the same size while the contribution from the spatial variation in the crystallographic axis is negligible. Around  $\theta_H = 10^\circ$ , the contribution in  $\Delta H_{\text{pp}}$  is almost completely determined by the damping due to the spatial variation in the demagnetization field.

In Table 5.1, the average, minimum and maximum fitting parameters are given for a  $\text{SiO}_x/\text{Co}(2)/\text{Pt}$  sample when the angular depen-

Table 5.1: Fitting parameters  $\alpha$ ,  $4\pi M_{\text{eff}}$ ,  $\Delta(\theta_H)$  and  $\Delta(4\pi M_{\text{eff}})$  of a  $\text{SiO}_x/\text{Co}(2)/\text{Pt}$  bilayer for angular dependent FMR measurements with electromagnets with a maximum field of 0.6 T and 1.5 T magnet. Shown are the average values of 10 fits with different g-factor and the maximum and minimum value from these fits.

	0.6 T magnet			1.5 T magnet			
	average	minimum	maximum	average	minimum	maximum	
$\alpha$	$3.5 \times 10^{-2}$	$2.0 \times 10^{-2}$	$6.3 \times 10^{-2}$	$4.1 \times 10^{-2}$	$3.3 \times 10^{-2}$	$4.54 \times 10^{-2}$	[-]
$4\pi M_{\text{eff}}$	8.5	6.7	11	10	9.3	11	[kG]
$\Delta(\theta_H)$	0.6	0.0	2	0.03	0.0	1	[°]
$\Delta(4\pi M_{\text{eff}})$	28	14	39	36	34	36	[G]

dence is measured with an electromagnet with a maximum DC field of 0.6 T or 1.5 T. Clearly visible is that the difference between the average and the minimum and maximum values for the 1.5 T magnet is much smaller than for the 0.6 T magnet, but the average values do not deviate too much.

All in all, the damping of these Co films can be described well with the local resonance model, where in addition to the Gilbert damping also the influence of the damping due to the spatial variations in the direction of the crystallographic axis and the demagnetization field should be taken into account. The Gilbert damping value for the 2 nm thick Co layer,  $3.5 - 4.1 \times 10^{-2}$ , has the right order of magnitude ( $10^{-2}$ ) for a transition-metal ferromagnet [42] and also the variations in the spatial variations in the direction of the easy axis (up to a few degrees) and the demagnetization field (0 - 100 G) show reasonable numbers [153].

In Figure 5.11.a, the normalized room temperature FMR spectra are shown for  $\text{SiO}_x/\text{Co}(d)/\text{Pt}$  bilayers with a varying Co thickness  $d$  measured with an in-plane field ( $\theta_H = 90^\circ$ ). The FMR spectra are normalized by subtracting the resonance field  $H_r$ , which is defined as the magnetic field where the derivative absorption is equal to 0. Also the absorption derivative is normalized by dividing by the maximum measured value of the absorption derivative. In Figure 5.11.b, the resonance fields  $H_r$  are plotted for the in-plane ( $\theta_H = 90^\circ$ ) magnetic field as a function of the Co thickness  $d$ .

Also in Figure 5.11.b, the peak-to-peak linewidth  $\Delta H_{\text{pp}}$  from the FMR spectra in Figure 5.11.a is plotted as a function of the Co thickness. Clearly visible is that when the Co thickness becomes smaller than 10 nm, the resonance field shifts to a higher value. For films with

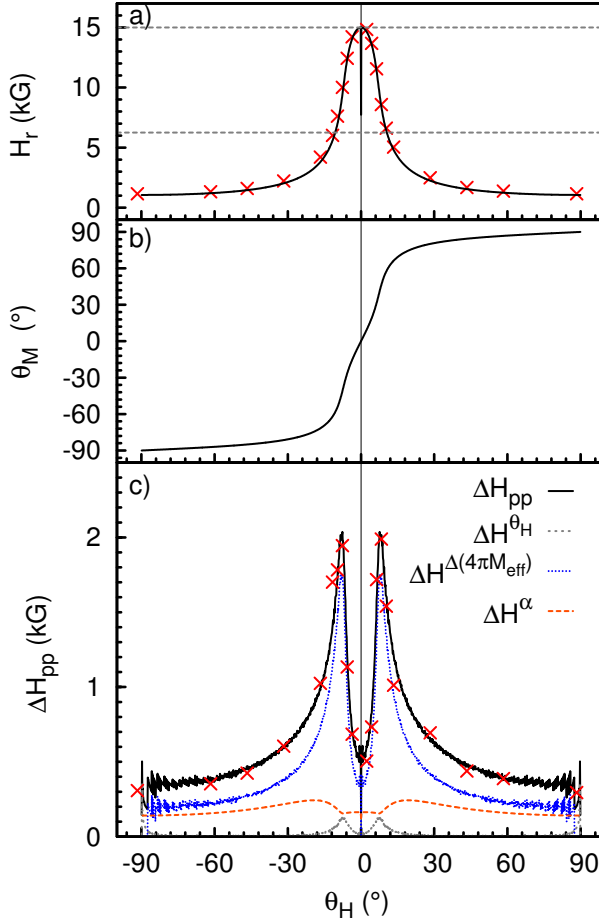


Figure 5.10: a) Angular dependence of the resonance field  $H_r$  of a  $\text{SiO}_x/\text{Co}(2)/\text{Pt}$  bilayer, where the red crosses ( $\times$ ) represent experimental data and the black line is a fit with a  $g$ -factor of 1.80 and  $M_{\text{eff}}$  of 10.8 kG. The two dotted lines indicate the maximum DC magnetic field the electromagnets can produce. b) The fitted angular dependence of the magnetization direction  $\theta_M$  as a function of the applied field  $\theta_H$ . c) Peak-to-peak linewidth of the  $\text{Co}(2)/\text{Pt}$  bilayer. The total peak-to-peak linewidth  $\Delta H_{pp}$ , black line with the experimental data as red crosses ( $\times$ ), consists of three components: intrinsic damping  $\Delta H^\alpha$  [ $\alpha = 0.034$ ] and the variation in the direction of the easy axis  $\Delta H^{\Delta(\theta_H)}$  [ $\Delta(\theta_H) = 0.15^\circ$ ] and the demagnetization field  $\Delta H^{\Delta(4\pi M_{\text{eff}})}$  [ $\Delta(4\pi M_{\text{eff}}) = 34$  G].

a Co layer thicker than 10 nm, the resonance field is nearly constant. Also  $\Delta H_{\text{pp}}$  becomes larger when the Co thickness becomes smaller. For Co thicknesses between 10 and 20 nm,  $\Delta H_{\text{pp}}$  is constant and when the Co thickness is larger than 20 nm,  $\Delta H_{\text{pp}}$  becomes again larger due to eddy current damping. So, for the Co thickness range we measure in this Chapter, we can distinguish three different regimes: for the thin Co films ( $d < 10$ ) we expect that the spin pumping damping mechanism is dominant, for the thick Co films ( $d > 20$  nm) we expect that the eddy current damping mechanism is dominant and between these two regimes there is a transition region.

Figure 5.12 shows the effective demagnetization  $M_{\text{eff}}$  and the saturation magnetization at room temperature for the  $\text{SiO}_x/\text{Co}(d)/\text{Pt}$  bilayers. As a reference, the bulk saturation magnetization of Co is indicated. The magnetization of the  $\text{SiO}_x/\text{Co}(d)/\text{Pt}$  multilayers was measured by dividing the measured magnetic moment by the measured sample volume (typical  $2.4 \text{ mm} \times 2.4 \text{ mm} \times d$ ). The error bars of the effective demagnetization field indicate the maximum and minimum values of the parameter in the fit for the range of  $g$ -factors. Clearly visible is that the effective demagnetization field becomes smaller, when the Co thickness decreases. Together with the  $\text{SiO}_x/\text{Co}(d)/\text{Pt}$  dataset which will be presented in Chapter 6, we see that the saturation magnetization stays nearly constant at a value of approximately 18.8 kG, compared with a value of 17.6 kG for bulk Co.

In Figure 5.13, the average fitting parameters are plotted as a function of the Co layer thickness  $d$ . The error bars indicate the maximum and minimum values of the parameter in the fit for the range of  $g$ -factors. A clear trend is visible for  $\alpha$ . When the Co layer thickness becomes smaller, the Gilbert damping  $\alpha$  increases. Furthermore,  $\Delta(\theta_H)$  and  $\Delta(4\pi M_{\text{eff}})$  are almost constant for Co thicknesses larger than 7.5 nm, but become somewhat larger for Co thicknesses smaller than 7.5 nm.

## 5.6 Spin pumping detected by the inverse spin Hall effect

Using the inverse spin Hall (ISH) effect, the spin current generated by the spin pumping can be electrically detected. Figure 5.8.b shows how the electrical contacts are made to the sample and the orientation of the contacts with respect to the sample and the applied magnetic field.

In Figure 5.14, the FMR spectrum and the electrically measured voltage  $V_m$  of a  $\text{SiO}_x/\text{Co}(25)/\text{Pt}$  bilayer are plotted. It is known [154] that

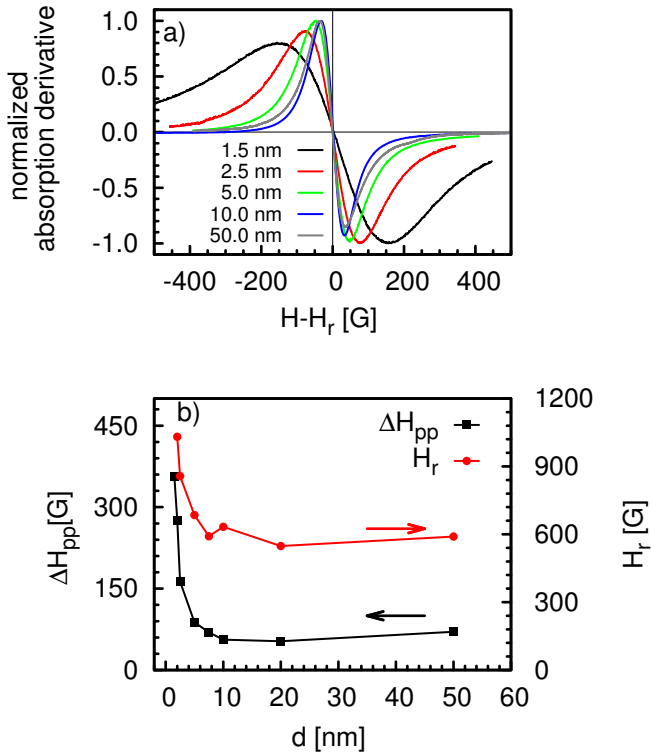


Figure 5.11: a) Normalized in-plane FMR spectra, measured at  $\theta_H = 90^\circ$ , for a  $\text{SiO}_x/\text{Co}(d)/\text{Pt}$  films, where the thickness  $d$  of the Co films was varied. The horizontal axis is the normalized dc magnetic field, where the  $H_r$ , red  $\bullet$ , for each film is shown in b). In b), also the linewidth of the FMR spectra, black  $\blacksquare$ , as a function of the Co thickness  $d$  is shown.

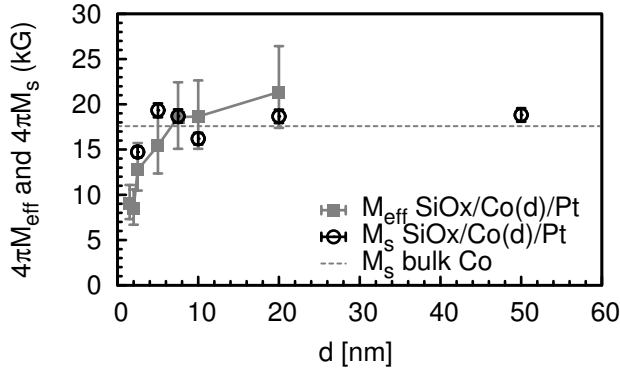


Figure 5.12: The effective demagnetization  $4\pi M_{\text{eff}}$  (gray  $\blacksquare$ ) and the saturation magnetization  $4\pi M_s$  (black  $\circ$ ), as a function of the thickness  $d$  of the Co layer in the  $\text{SiO}_x/\text{Co}(d)/\text{Pt}$  multilayer. The dotted line shows the saturation magnetization of bulk Co.

the lineshape of  $V_m$  consists of two parts. One is symmetric and a combination of the ISH voltage and the anomalous magnetoresistance effect (AMR). The other is antisymmetric and originates from the anomalous Hall effect (AHE), generated by the electric field component of the applied microwave field. By fitting a Lorentian lineshape  $V_s$  and the derivative of a Lorentian lineshape  $V_a$ , the symmetric and antisymmetric contributions can be separated. The ISH and the AMR effects in the symmetric lineshape can be distinguished by an inversion of the applied magnetic field. The ISH effect changes sign when the direction of the applied magnetic field is inverted, but the contribution due to the AMR does not change sign [70]. For the rest of the measurements, the symmetric part of the measured voltage is shown and called the ISH voltage  $V_{\text{ISH}}$ .

In Figure 5.15.a, the ISH voltage is plotted as a function of the applied magnetic field for different field angles  $\theta_H$ . Clearly visible is that for an in-plane applied field ( $\theta_H = 90^\circ$  and  $270^\circ$ ), the resonance condition is fulfilled with a small magnetic field. When rotating the sample slowly to an out-of-plane orientation ( $\theta_H = 0^\circ$  and  $180^\circ$ ), the  $V_{\text{ISH}}$  curve moves to a higher magnetic field. The value of the measured maximum ISH voltage of each curve does not change when the field angle is varied as shown in Figure 5.15.b. We cannot measure  $V_{\text{ISH}}$  close to the out-of-plane orientation, because our magnet cannot produce a large enough magnetic field to fulfill the resonance condition. This results in



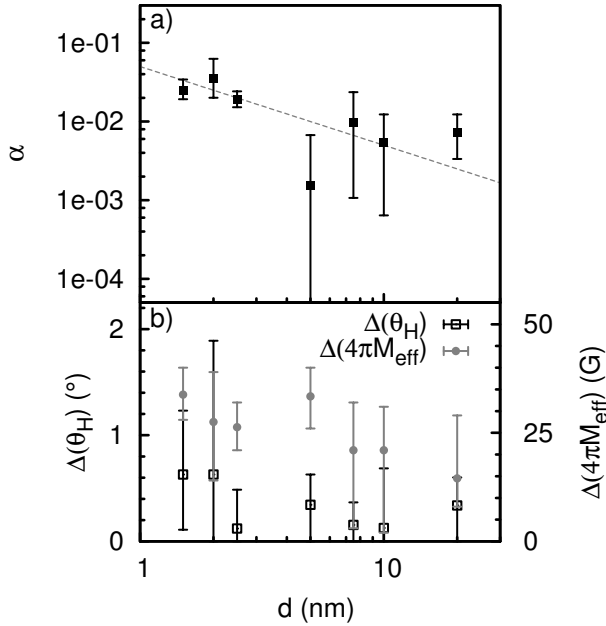


Figure 5.13: a) The damping  $\alpha$ , black  $\blacksquare$  and in b)  $\Delta(\theta_H)$ , black  $\square$ , and  $\Delta(4\pi M_{\text{eff}})$ , gray  $\bullet$ , as a function of the thickness  $d$  of the Co layer in the  $\text{SiO}_x/\text{Co}(d)/\text{Pt}$  bilayers. Shown are the average values of 10 simulations with different g-factor and the maximum and minimum value from these simulations. The dashed line shows a  $1/d$ -dependence as a guide to the eye.

an abrupt jump of  $V_{\text{ISH}}$  at angles close to the out-of-plane orientations ( $\theta_H = 0^\circ$  and  $180^\circ$ ). Furthermore, it is visible that  $V_{\text{ISH}}$  changes sign when the direction of the applied field is changed. This indicates that the measured symmetric component is only due to the ISH voltage.

The angular dependence of  $V_{\text{ISH}}$  is given by [155]

$$V_{\text{ISH}} \propto \frac{\sin \theta_M \left[ \frac{H_r}{4\pi M_s} \cos(\theta_M - \theta_H) - \cos 2\theta_M \right]}{\left[ 2 \frac{H_r}{4\pi M_s} \cos(\theta_M - \theta_H) - \cos \theta_M - \cos^2 \theta_M \right]^2}. \quad (5.18)$$

Using the fitted values of  $\theta_M$  and  $H_r$  from the angular dependent FMR fit, we plot equation 5.18 in Figure 5.15.

In Figure 5.16.a,  $V_{\text{ISH}}$  of a  $\text{SiO}_x/\text{Co}(25)/\text{Pt}$  bilayer is plotted as a function of the applied microwave power  $P_{\text{RF}}$  for  $\theta_H = 90^\circ$ . With in-

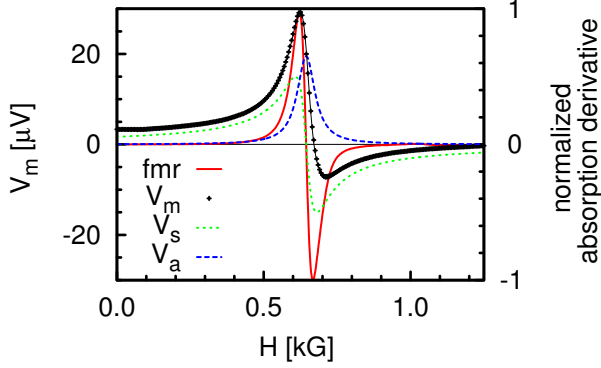


Figure 5.14: The electrically detected voltage  $V_m$  of a  $\text{SiO}_x/\text{Co}(25)/\text{Pt}$  bilayer is shown as a function of the applied magnetic field  $H$ . As a reference, also the FMR spectrum is shown. The measured voltage  $V_m$  consist of a symmetric  $V_c$  and antisymmetric  $V_a$  part, which can be obtained by fitting a Lorentzian and a derivative of a Lorentzian to the measured voltage  $V_m$ .

creasing  $P_{\text{RF}}$ ,  $V_{\text{ISH}}$  increases.  $V_{\text{ISH}}$  scales linearly with the applied microwave power, as is shown in Figure 5.16.b.

In Figure 5.16.c,  $V_{\text{ISH}}$  at 158.9 mW is plotted as a function of the thickness of the Co layer. For thin Co films,  $V_{\text{ISH}}$  increases linearly with the thickness of the Co layer. We measured a maximum voltage for the Co layer with a thickness of 25 nm and for the next measured Co thickness (50 nm), we observe a decrease. The measured  $V_{\text{ISH}}$  as a function of the thickness of the normal metal  $d_N$  and ferromagnet  $d_F$  layer is described by [156]

$$V_{\text{ISH}} = L \frac{2e/\hbar}{\sigma_N(d_N)d_N + \sigma_F(d_F)d_F} \left[ j_{1s}^z(0)\alpha_{\text{SHE},N}l_{\text{SD},N} \tanh \frac{d_N}{2l_{\text{SD},N}} + j_{2s}^z(0)\alpha_{\text{SHE},F}l_{\text{SD},F} \tanh \frac{d_F}{2l_{\text{SD},F}} \right], \quad (5.19)$$

where  $L$  is the distance between the two voltage contacts,  $\sigma_i(d_i)$  and  $\alpha_{\text{SHE},i}$  are the thickness dependent conductivity and the spin Hall angle of the normal metal or ferromagnet respectively and  $j_{1s}^z(0)$  and  $j_{2s}^z(0)$  are the spin currents at the normal and ferromagnetic side of the interface respectively. The first term in the brackets represents the backflow from the spin current from the spin sink. If the thickness of

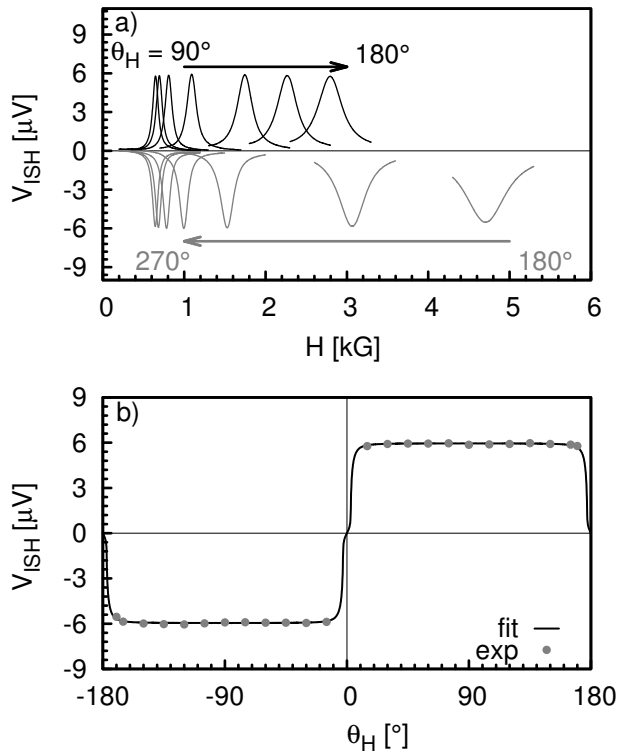


Figure 5.15: a) Field dependence of the inverse spin Hall voltage  $V_{\text{ISH}}$  of a  $\text{SiO}_x/\text{Co}(10)/\text{Pt}$  bilayer for different field angles  $\theta_H$ , where at  $90^\circ$  and  $270^\circ$  the applied magnetic field is in-plane and at  $0^\circ$  and  $180^\circ$  the applied magnetic field is out-of-plane. b) Inverse spin Hall voltage as a function of the field angle  $\theta_H$  plotted together with equation 5.18.

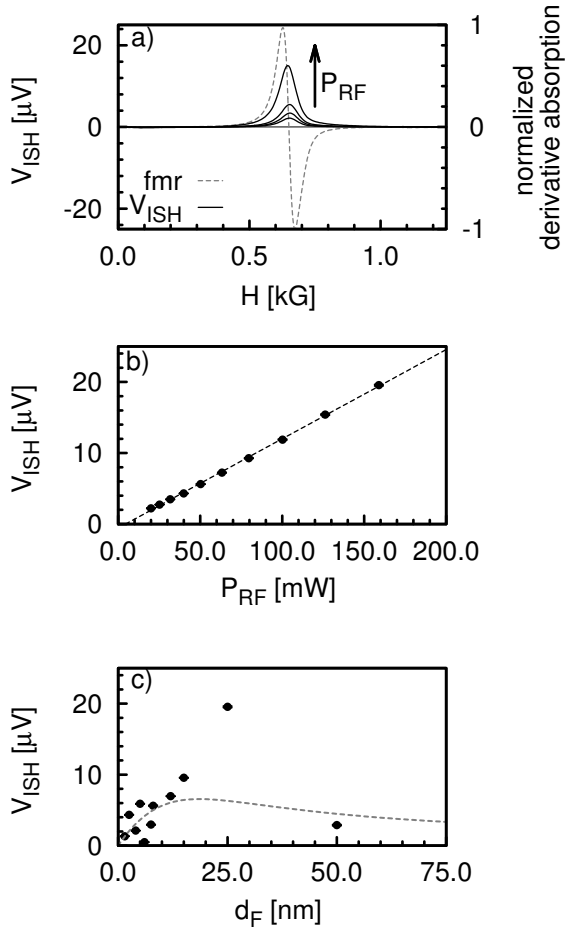


Figure 5.16: a) The inverse spin Hall voltage  $V_{\text{ISH}}$  of a  $\text{SiO}_x/\text{Co}(25)/\text{Pt}$  bilayer as a function of the applied microwave power  $P_{\text{RF}}$  for  $\theta_H = 90^\circ$ . Also the measured FMR spectrum of the  $\text{SiO}_x/\text{Co}(25)/\text{Pt}$  bilayer is shown. b) The measured  $V_{\text{ISH}}$  of the  $\text{SiO}_x/\text{Co}(25)/\text{Pt}$  bilayer as a function of the applied microwave power. c) The maximum measured  $V_{\text{ISH}}$  ( $P_{\text{RF}} = 158.9$  mW and  $\theta_H = 90^\circ$ ) as a function of the thickness of the ferromagnet  $d_F$  plotted together with equation 5.19.

the spin sink is not larger than twice the spin diffusion length, the spin sink cannot be described as ideal, since not all the spin current is absorbed. The second term in the brackets describes the spin current in the ferromagnet. When the thickness of the ferromagnet is smaller than the spin diffusion length in the ferromagnet, the spin current in the ferromagnet will vanish. In Figure 5.16.c, equation 5.19 is plotted for a set of parameters which mimics the measured behaviour of  $V_{\text{ISH}}$  as a function of the Co thickness. Clearly visible is that for small Co thicknesses,  $V_{\text{ISH}}$  increases since  $d_F < l_{\text{SD},F}$ . When the thickness of the Co increases, the  $1/d_F$  contribution becomes larger and  $V_{\text{ISH}}$  decreases again.

The measurements shown in this section demonstrate that spin pumping is present in the  $\text{SiO}_x/\text{Co}/\text{Pt}$  multilayers. However, an accurate description of the size of the measured ISH voltages is not straightforward, as many material dependent fitting parameters are not (well) known in the literature for ultrathin films and the parameters known depend strongly on how the films are grown [157, 158].

## 5.7 Low temperature electrical characterisation

Before measuring low temperature FMR spectra on the  $\text{SiO}_x/\text{Co}/\text{Pt}$  and  $\text{SiO}_x/\text{Co}/\text{Cu}$  bilayers, the electrical properties of the used metals were measured. In Figure 5.17, the normalized resistance of a 50 nm thick Co, Pt and Cu and a  $\text{SiO}_x/\text{Co}(10)/\text{Pt}$  Hall bar are plotted. No anomalies are visible and the residual resistance ratios (RRR) are 2.76, 1.96 and 1.26 for the 50 nm thick Cu, Co, Pt film and 1.50 for the  $\text{SiO}_x/\text{Co}(10)/\text{Pt}$  bilayer.

## 5.8 Low temperature spin pumping

Figure 5.18 shows the temperature dependence of the normalized peak-to-peak linewidth  $\Delta H_{\text{pp}}$  (a) and resonance field  $H_r$  (b) of a  $\text{SiO}_x/\text{Co}(10)/\text{Cu}$  and a  $\text{SiO}_x/\text{Co}(10)/\text{Pt}$  thin films that were measured with an in-plane ( $\theta_H = 90^\circ$ ) applied magnetic field. Both  $\Delta H_{\text{pp}}$  and  $H_r$  are normalized by dividing the measured values by the measured values at 290 K. The peak-to-peak linewidths of both the  $\text{SiO}_x/\text{Co}(10)/\text{Cu}$  and the  $\text{SiO}_x/\text{Co}(10)/\text{Pt}$  films increase when decreasing the temperature until the maximum is reached. For the  $\text{SiO}_x/\text{Co}(10)/\text{Cu}$  samples the maximum was measured at 40 K and  $\Delta H_{\text{pp}}$  was 1.5 times as large the one measured at 290 K. For the  $\text{SiO}_x/\text{Co}(10)/\text{Pt}$  sample the maximum was measured at 30 K and  $\Delta H_{\text{pp}}$  was 1.7 times as large as the one measured at 290 K. When decreasing the temperature even further,

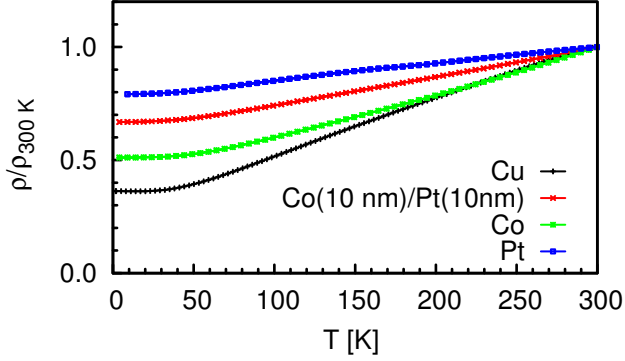


Figure 5.17: a) Normalized resistivity of Co(50), Cu(50), Pt(50) and SiO<sub>x</sub>/Co(10)/Pt Hallbar as a function of temperature. The resistivity at 300 K is 175, 30, 2315 and 927 nΩm for Cu, Co, Pt and SiO<sub>x</sub>/Co(10)/Pt respectively.

the linewidth becomes narrower again. The measured resonance field in Figure 5.18.b shows a different behaviour. For the SiO<sub>x</sub>/Co(10)/Cu samples  $H_r$  remains constant over the whole measured temperature range, whereas  $H_r$  of the SiO<sub>x</sub>/Co(10)/Pt sample increases when decreasing the temperature and becomes almost constant below 100 K.

To gauge whether the contributions of the sample inhomogeneities and the intrinsic relaxation to the total damping change, the angular dependence of a SiO<sub>x</sub>/Co(10)/Pt bilayer was measured at 30 K and 300 K. In Table 5.2, the average, minimum and maximum fitting parameters are shown. When decreasing the temperature, all four fitting parameters become larger. The three parameters involving the damping,  $\alpha$ ,  $\Delta(\theta_H)$  and  $\Delta(4\pi M_{\text{eff}})$ , all becomes approximately 1.8 times as large.

As discussed in Section 5.3.1, theoretical models calculate the damping as a function of scattering time  $\tau$  and distinguish two cases; intraband scattering which is proportional to  $\tau$  and interband scattering which is proportional to  $1/\tau$ . The temperature dependence of the scattering rate is not well known, but from the scattering rate the resistivity can be calculated straightforwardly. Gilmore [146] calculated the damping as a function of the resistivity, where he assumed that the resistivity is dominated by electron-lattice interactions and that electron-electron interactions play a minimal role. He predicts then that the

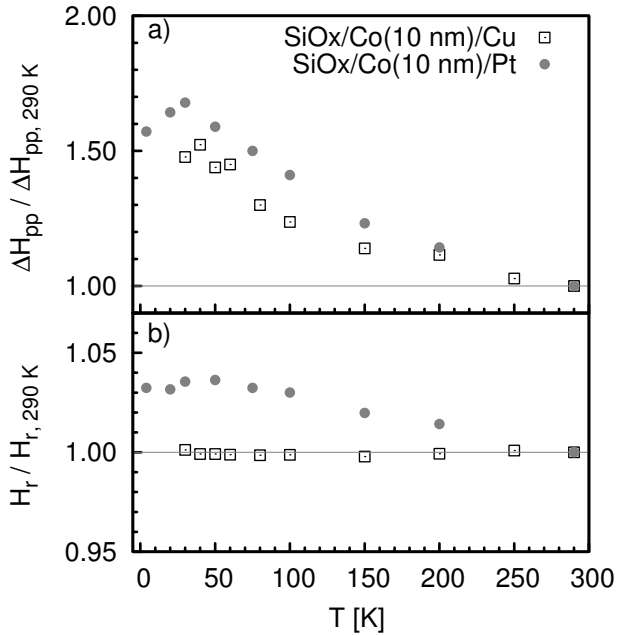


Figure 5.18: a) Normalized in-plane ( $\theta_H = 90^\circ$ ) peak-to-peak linewidth  $\Delta H_{pp}$ , for a SiO<sub>x</sub>/Co(10)/Pt (gray ●) and SiO<sub>x</sub>/Co(10)/Cu (black □) bilayer as a function of temperature.  $\Delta H_{pp}$  is normalized by dividing the measured values by the measured  $\Delta H_{pp}$  at 290 K.  $\Delta H_{pp}$  at 290 K was 35 G for the SiO<sub>x</sub>/Co(10)/Cu bilayer and 56 G for the SiO<sub>x</sub>/Co(10)/Pt bilayer respectively. b) Normalized resonance field  $H_r$  for a SiO<sub>x</sub>/Co(10)/Pt and a SiO<sub>x</sub>/Co(10)/Cu bilayer as a function of temperature.  $H_r$  is normalized by dividing the measured values by  $H_r$  at 290 K.  $H_r$  at 290 K was 572 G for the SiO<sub>x</sub>/Co(10)/Cu bilayer and 633 G for the SiO<sub>x</sub>/Co(10)/Pt bilayer respectively.

Table 5.2: Fitting values for the damping  $\alpha$ ,  $4\pi M_{\text{eff}}$ ,  $\Delta(\theta_H)$  and  $\Delta(4\pi M_{\text{eff}})$  for fitting of the measured values of a  $\text{SiO}_x/\text{Co}(10)/\text{Pt}$  bilayer at 300 K and 30 K. Shown are the average values of 10 simulations with different g-factor and the maximum and minimum value from this simulations.

	300 K			30 K			
	average	minimum	maximum	average	minimum	maximum	
$\alpha$	$6.62 \times 10^{-3}$	$3.94 \times 10^{-3}$	$1.23 \times 10^{-2}$	$1.23 \times 10^{-2}$	$8.90 \times 10^{-3}$	$1.71 \times 10^{-2}$	[-]
$4\pi M_{\text{eff}}$	18.7	15.1	22.7	19.9	16.3	24.3	[kG]
$\Delta(\theta_H)$	0.13	0	0.71	0.23	0	0.43	[°]
$\Delta(4\pi M_{\text{eff}})$	21	20	31	38	30	53	[G]

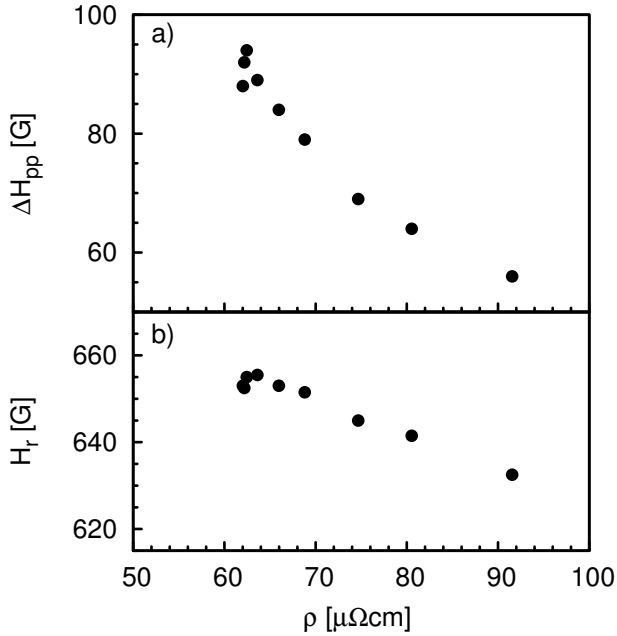


Figure 5.19: In-plane ( $\theta_H = 90^\circ$ ) peak-to-peak linewidth  $\Delta H_{\text{pp}}$  (a) and resonance field  $H_r$  (b), for a  $\text{SiO}_x/\text{Co}(10)/\text{Pt}$  bilayer as a function of the resistivity.



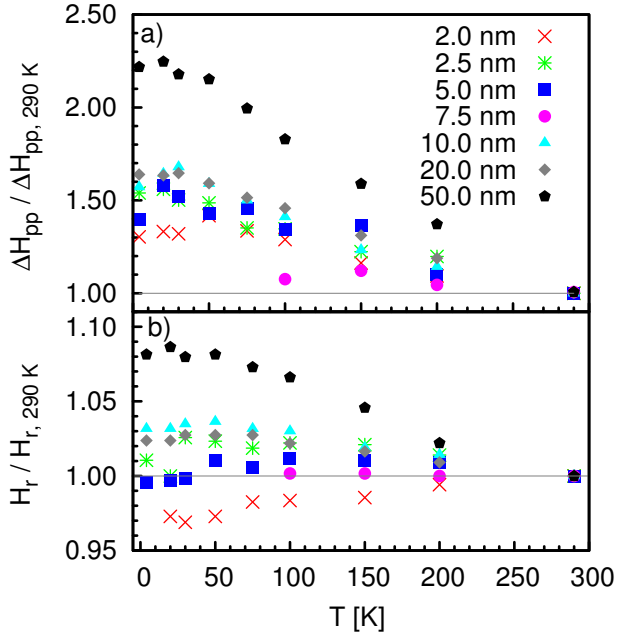


Figure 5.20: a) Normalized in-plane ( $\theta_H = 90^\circ$ ) peak-to-peak linewidth  $\Delta H_{pp}$  for  $\text{SiO}_x/\text{Co}(d)/\text{Pt}$  bilayer as a function of temperature.  $\Delta H_{pp}$  is normalized by dividing the measured values by the measured values at 290 K. b) Normalized resonance field  $H_r$  for  $\text{SiO}_x/\text{Co}(d)/\text{Pt}$  films as a function of temperature.  $H_r$  is normalized, by dividing the measured values by the measured values at 290 K.  $\Delta H_{pp}$  and  $H_r$  at 290 K can be found in Figure 5.11.b.

damping changes from the intraband to the interband scattering mechanism around a resistivity of approximately  $1\text{--}100 \mu\Omega\text{cm}$ , dependent on the lifetimes of the spin-up versus spin-down states.

By plotting  $\Delta H_{pp}$  as a function of the resistivity, experimental data can be compared with these theoretical predictions. Figure 5.19 shows how  $\Delta H_{pp}$  and  $H_r$  of the  $\text{SiO}_x/\text{Co}(10)/\text{Pt}$  bilayer vary as a function of the resistivity. The resistivity of the bilayer is measured with a different  $\text{SiO}_x/\text{Co}(10)/\text{Pt}$  bilayer, that was patterned into a Hall bar. Both show a monotonic increase with a maximum at a resistivity of  $63 \mu\Omega\text{cm}$ . Below this value, both  $\Delta H_{pp}$  and  $H_r$  decrease.

Figure 5.20.a shows how the measured and normalized  $\Delta H_{pp}$  of all

SiO<sub>x</sub>/Co(*d*)/Pt bilayers (shown in Figure 5.18 for *d* = 10 nm) changes as function of the Co layer thickness. The normalization values can be found in Figure 5.11.b. Most bilayers show similar behaviour to what was seen for the SiO<sub>x</sub>/Co(10)/Pt bilayer in Figure 5.18.a. When decreasing the temperature, the linewidth becomes broader up to a certain temperature. For the films with a Co-layer thinner than 20 nm, the maximum linewidth is approximately 1.3 to 1.7 times as large as the linewidth at 290 K and the linewidth of the sample with the 50 nm thick Co layer becomes even 2.2 times as large. For all samples that were measured in the full temperature range, the maximum  $\Delta H_{pp}$  was found around 20 to 30 K.

In Figure 5.20.b, the normalized resonance fields of the SiO<sub>x</sub>/Co(*d*)/Pt bilayers are plotted as a function of temperature. The normalization values can be found in Figure 5.11.b. Three things can be observed. First,  $H_r$  of the SiO<sub>x</sub>/Co(50)/Pt bilayer increases when the temperature is decreased and the maximum measured increase is almost 1.1 times. The maximum  $H_r$  of all the other measured samples does not become larger than 1.05 times the resonance field at 290 K. Secondly,  $H_r$  of the SiO<sub>x</sub>/Co(2.5)/Pt bilayer becomes smaller than the  $H_r$  at 290 K. This happens also for the SiO<sub>x</sub>/Co(5)/Pt bilayer, but only at low temperatures.  $H_r$  of the other bilayers show similar behaviour as the SiO<sub>x</sub>/Co(*d*)/Pt bilayer in Figure 5.18.b. When decreasing the temperature,  $H_r$  becomes larger and after a certain temperature  $H_r$  stays almost constant.

In Figure 5.21,  $\Delta H_{pp}$  is plotted for different temperatures as a function of the thickness *d* of the Co-layer in the SiO<sub>x</sub>/Co(*d*)/Pt bilayers. The thick Co film (*d* = 50 nm) shows a large increase in the damping. When decreasing the Co thickness, an increase in the peak-to-peak linewidth can be observed, as is predicted by equation 2.19. This increase in linewidth behaves the same at all the measured temperatures.

## 5.9 Discussion

The question raised in the beginning of this Chapter was whether we can show the presence of a spin pumping effect in SiO<sub>x</sub>/Co/Pt bilayers and find its temperature dependence. For this, the peak-to-peak linewidths  $\Delta H_{pp}$  in FMR experiments were measured and analyzed in order to separate intrinsic and extrinsic effects. From these data a number of conclusions can be drawn, which will be done below. We separate this in different parts. In the first part, we discuss the dependence of  $\Delta H_{pp}$  on the Co-thickness, which is a signature of spin pumping.

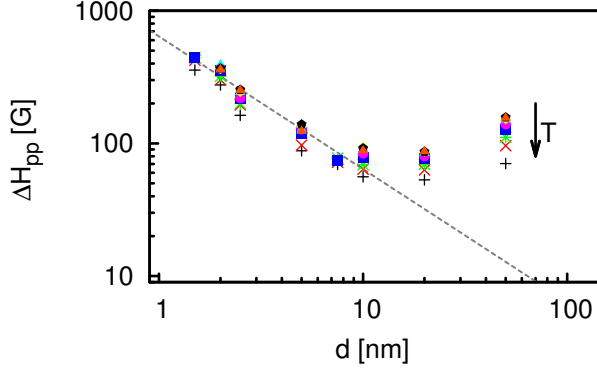


Figure 5.21: Peak-to-peak linewidth  $\Delta H_{pp}$  as a function of the thickness  $d$  of the  $\text{SiO}_x/\text{Co}(d)/\text{Pt}$  bilayers for different temperatures. The direction of the arrow indicates an increase in temperature. The dashed line shows a  $1/d$ -dependence as a guide to the eye.

Next we discuss reasons for the peculiar temperature dependence of  $\Delta H_{pp}$ . Then, in the course of the analysis, values for the saturation magnetization  $4\pi M_s$  and the effective demagnetization fields  $4\pi M_{\text{eff}}$  were extracted, which will be discussed as well.

### 5.9.1 Dependence of $\Delta H_{pp}$ on Co-thickness

The main experimental findings here are that  $\Delta H_{pp}$  at room temperature shows for thin Co thicknesses,  $d < 10$  nm, a  $1/d$  dependence (see Figure 5.11.b). Furthermore, after separating the various contributions to  $\Delta H_{pp}$ , the Gilbert damping  $\alpha$  is also found to show a  $1/d$  dependence for small Co thicknesses,  $d < 10$  nm (see Figure 5.13.a). The larger uncertainty in the latter statement is caused by uncertainty introduced in the separation procedure. The  $1/d$ -dependence is a characteristic of spin-pumping [67].

The observed angular dependence of the inverse spin Hall voltage  $V_{ISH}$  of the  $\text{SiO}_x/\text{Co}/\text{Pt}$  bilayers, as shown in Figure 5.15, gives further confirmation that the spin pumping is present. Also the observed thickness dependence of  $V_{ISH}$ , as shown in Figure 5.16.c, satisfies the expected behaviour that the measured  $V_{ISH}$  increases with a increasing thickness of the ferromagnet until a certain thickness, whereafter  $V_{ISH}$  decreases rapidly. We choose however not to use the measured  $V_{ISH}$  as a probe to study the temperature dependence of the spin pumping ef-

fect, since it depends on many temperature dependent parameters such as the conductivity, the spin diffusion length and the Gilbert damping, where the latter two have not been systematically measured as a function of temperature.

In order to characterize the low temperature behaviour, we chose to measure the in-plane ( $\theta_H = 90^\circ$ )  $\Delta H_{pp}$ . To gauge whether the ratio of intrinsic and extrinsic contributions changed at low temperatures, the angular dependence of the FMR spectra was measured for one  $\text{SiO}_x/\text{Co}(10)/\text{Pt}$  bilayer at 300 K and 30 K. In Table 5.2 it is shown that the ratio of the contribution of the intrinsic relaxation and the relaxation due to sample inhomogeneities stays the same. Figure 5.21 shows that the dependence of  $\Delta H_{pp}$  on  $d$  is the same for all temperatures. Together, it feels safe to conclude that also for  $\alpha$  there is no change in the room temperature and low temperature thickness dependence, while the value of  $\alpha$  has increased by about a factor of 1.8.

The spin pumping theory says that the change in the Gilbert damping is caused by the effective spin mixing conductance  $A_{\text{eff}}^{\uparrow\downarrow}$ , where in diffusive bilayers  $A_{\text{eff}}^{\uparrow\downarrow}$  is governed by the conductivity  $\sigma(T)$  of the normal metal layer. The data presented here confirms this picture. However, the temperature dependence of  $\Delta H_{pp}$  of the  $\text{SiO}_x/\text{Co}(d)/\text{Pt}$  bilayers as shown in Figure 5.20.a, behaves as a non-monotonously increasing function, and this cannot be explained using the spin pumping theory.

## 5.9.2 Dependence of $\Delta H_{pp}$ on temperature

The temperature dependence of  $\Delta H_{pp}$  of both the  $\text{SiO}_x/\text{Co}(10)/\text{Pt}$  and  $\text{SiO}_x/\text{Co}(10)/\text{Cu}$ , given in Figure 5.18, shows that the  $\Delta H_{pp}$  is not a monotonously increasing or decreasing function.  $\Delta H_{pp}$  increases by about a factor of 1.6 when decreasing the temperature until the maximum is reached, around 30 - 40 K.

Experiments on single crystal Co whiskers [42, 142] with a residual resistance ratio (RRR) value between 80-150 showed that  $\Delta H_{pp}$  increased when the temperature is decreased and saturates at approximately 30 K, where  $\Delta H_{pp}$  is approximately 3.5 times larger than the linewidth at 300 K. Lloyd and Bhagat [141] showed furthermore, that when alloying Ni with 5 % Cu and thereby reducing the RRR from 30 to 3, no temperature dependence was observed for the linewidth. They attribute the increase in linewidth to a possible increase of the mean free path of the conduction electrons. Also Bastian and Biller [159] measured the temperature dependence of the damping in a Ni-Fe al-

loy. Already with a Fe concentration of 6 %, the increase in linewidth at low temperatures disappeared. They attribute this disappearing of the peak at low temperatures to a decrease of  $\tau$  by approximately 1 order of magnitude, when alloying the Ni with 6 % Fe.

It is rather surprising that we observe the same behaviour in very thin polycrystalline films with a RRR of just 2 as in single crystal whiskers, since the amount of disorder (where the RRR indicates the amount of disorder) determines both the resistivity and the Gilbert damping.

Czeschka et al. [70] observed the same behaviour for  $\Delta H_{pp}$  of a  $\text{SiO}_x/\text{Co}(10)/\text{Pt}(7)$  bilayer. However, in their measurement  $H_r$  becomes smaller for temperatures below 100 K. They attribute both effects to a change in the magnetic anisotropy due to a temperature dependent strain.

In the literature, there are several theories that describe the low temperature behaviour on a phenomenological level via the magnetoelastic coupling between the magnetization and the lattice strain [160]. We choose a different explanation however, observing that the damping is closely linked to the conductivity. As explained in Section 5.3.1, in particular intraband and interband scattering have a different dependence on the conductivity. In Figure 5.19,  $\Delta H_{pp}$  is plotted as a function of the resistivity. We propose that the maximum in this plot is due to the crossover from intraband scattering at high resistivity (high temperature) to interband scattering at low resistivity (low temperature). Note that a connection to phonons is less likely, since Bastian and Biller [159] found the maximum of their Ni whisker around room temperature. Also the lack of thickness dependence of the  $\Delta H_{pp}$  as shown in Figure 5.20, makes clear that surface scattering of the Fuchs-Sondheimer type [161, 162] does not play an important role.

$\Delta H_{pp}$  in Figure 5.20.a shows for Co thicknesses thinner than 20 nm the same behaviour as the  $\text{SiO}_x/\text{Co}(10)/\text{Pt}$  bilayer.  $\Delta H_{pp}$  of the  $\text{SiO}_x/\text{Co}(50)/\text{Pt}$  sample becomes much larger when decreasing the temperature. For Co layers of this thickness, the main damping mechanism is not spin pumping anymore, but eddy current damping. Eddy current damping scales with the conductivity and the conductivity increases with a factor of 1.6 as can be seen in Figure 5.17. The total damping of the 50 nm thick film consists then of intrinsic damping, which increases approximately a factor 1.6 when going to low temperatures and the eddy current damping, that also increases a factor 1.6 when decreasing the temperature. The total damping increases then approximately a factor 2.2 when decreasing the temperature, which agrees very well with the observed broadening in Figure 5.20.a.

### 5.9.3 Comparison between Co/Pt and Co/Cu

This Chapter was mainly concerned with  $\text{SiO}_x/\text{Co}/\text{Pt}$  bilayers, and it was explained that the line broadening with decreasing Co thickness is due to the spin pumping effect, caused by the spin-flip scattering (spin-sinking) of the Pt layer. A less strong scattering material such as Cu could be expected to yield less, or no, broadening effects with decreasing Co thickness. Such a comparison was made with samples of  $\text{SiO}_x/\text{Co}(10)/\text{Pt}$  and  $\text{SiO}_x/\text{Co}(10)/\text{Cu}$ . We chose bilayers with a 10 nm thick Co layer, because the Co thickness should be far enough away from the region where we expect that the different spin-orbit torques plays an important role in the magnetization dynamics [14, 54–57]. Furthermore, the Co thickness should not be too thick, otherwise the contribution of the spin pumping effect becomes too small.

For the  $\text{SiO}_x/\text{Co}(10)/\text{Cu}$  and  $\text{SiO}_x/\text{Co}(10)/\text{Pt}$  multilayers,  $\Delta H_{\text{pp}}$  at room temperature is 35 and 56 G respectively, where we contribute the difference in linewidth due to spin pumping in a good and bad spin sink. In Figure 5.18.a, the temperature dependence of the normalized  $\Delta H_{\text{pp}}$  is plotted for both bilayers. The temperature dependence shows that  $\Delta H_{\text{pp}}$  behaves the same for the  $\text{SiO}_x/\text{Co}/\text{Pt}$  and  $\text{SiO}_x/\text{Co}/\text{Cu}$  bilayers. This is in agreement with the observation in the previous section, where we contribute the low temperature  $\Delta H_{\text{pp}}$  behaviour to a crossover from interband scattering to intraband scattering.

### 5.9.4 Saturation magnetization, effective demagnetization field and resonance field

The room-temperature saturation magnetization, as shown in Figure 5.12, shows an average saturation magnetization of 18.8 kG. This is larger than the saturation magnetization of bulk Co, 17.6 kG. On top of the Co thin film is a Pt layer. Pt is non-magnetic, but it almost satisfies the Stoner criterion for the onset of ferromagnetism. From literature, it is known that at the Co/Pt interface Co can induce a magnetic moment into Pt [163].

In particular, X-ray resonant magnetic scattering (XRMS) [163] and magnetic circular X-ray dichroism (XMCD) [164] has been used to show that magnetic moments are induced on the Pt atoms and that the orbital magnetic moment of the Co atoms at the interface increases due to the Co 3d-Pt 5d interfacial hybridization.

The data indicate that up to 0.3 nm, the induced Pt 5d magnetization is  $0.2 \mu_B$  per Pt atom, which introduces an extra magnetization of 1.2 kG. The room-temperature saturation magnetization of the Co that

we measured for the Co/Pt bilayers when corrected for the induced magnetization in the Pt layer, is then 17.6 kG, which compares well with the bulk saturation magnetization value for Co.

The saturation magnetization for the Co/Pt bilayer with a 2.5 and 10 nm thick Co layer shows a slightly lower value, which is probably due to the uncertainty in the thickness of the Co film. Another indication for uncertainty in the thickness is seen in Figure 5.11.b, where  $H_r$  of the SiO<sub>x</sub>/Co(10)/Pt bilayer is larger than  $H_r$  of the SiO<sub>x</sub>/Co(7.5)/Pt bilayer, which suggest that the 10 nm thick Co layer is thinner than the 7.5 nm thick Co layer. However,  $\Delta H_{pp}$  of the SiO<sub>x</sub>/Co(10)/Pt is not larger than  $\Delta H_{pp}$  of the SiO<sub>x</sub>/Co(7.5)/Pt, which suggest that the 10 nm Co layer is thicker than the 7.5 nm Co layer. It is not clear what causes this anomaly.

The temperature dependence of  $H_r$  (see Figure 5.18.b) of the bilayers with a Co thickness between 5 and 20 nm can be explained by a lower Curie temperature of the CoPt alloy at the interface of the Co/Pt bilayer. The behaviour of the resonance field for the SiO<sub>x</sub>/Co/Pt with a thickness of the Co layer less than 5 nm is unexpected and we tentatively attribute this decrease of the resonance field to the temperature dependence of the Rashba spin-orbit torque (see Chapter 6).

The temperature dependence of  $H_r$  of the SiO<sub>x</sub>/Co(10)/Pt(7) bilayer of Czescka et al. [70] shows a different trend, as  $H_r$  becomes smaller with decreasing temperatures. The big difference between their samples and our samples is the growth method. Their samples were grown using the evaporating technique, that should result in more sharp interfaces and a different grain size than our samples that were grown using the sputtering technique [158].

In Figure 5.12,  $4\pi M_{eff}$  becomes smaller as the Co thickness decreases. From the magnetization measurements, the saturation magnetization for the SiO<sub>x</sub>/Co( $d$ )/Pt is almost constant for decreasing thickness  $d$  of the Co layer. As  $4\pi M_{eff}$  is equal to  $4\pi M_s - H_{\perp}$ , the perpendicular anisotropy  $H_{\perp}$  increases for the thinner Co thicknesses as has been shown with magnetization [165], MCXD [164] and XRMS [163] measurements. This decrease of  $4\pi M_{eff}$  can also be observed as an increase of the resonance fields as function of the thickness of the Co layers. For very thin Co layers, also other physical mechanisms, that are discussed in Chapter 6, contribute to the increase of the resonance field.

## 5.10 Summary

We conclude this Chapter by summarizing the main results as they emerge from the discussion. We measured the temperature dependence of the FMR spectra from  $\text{SiO}_x/\text{Co}(d)/\text{Pt}$  bilayers for varying thicknesses  $d$  of the Co film. When decreasing the temperature, the saturation magnetization of the  $\text{SiO}_x/\text{Co}/\text{Pt}$  bilayer increases due to an induced magnetic moment in the Pt and we observe that the intrinsic scattering mechanism changes from the intraband to the interband transition. Our main result is that the spin pumping mechanism is a temperature independent phenomenon.



# Spin-orbit torque in $\text{SiO}_x/\text{Co}/\text{Cu}$ bilayers

Traditional spintronic devices consist of two ferromagnetic layers, the polarizer and the free layer, with a normal nonmagnetic spacer, a tunnel barrier or a domain wall in between and either in a perpendicular or lateral geometry with respect to the current. Basically, the current flowing through the first ferromagnetic layer becomes polarized and can change the magnetization direction of the second ferromagnetic layer via the spin transfer torque mechanism.

Recently, experiments and theory have shown that there are alternative mechanisms that can produce a spin torque, based on the spin-orbit interaction (SOI). The SOI transfers orbital angular momentum from the lattice to the spin system. Up to now, the spin Hall and Rashba effects, both based on the SOI, are used to exploit the coupling between the electron spin and the orbital motion. The spin-orbit torque (SOT) in ferromagnetic structures, generated by such SOIs, received a lot of attention as it shows to be an efficient electric magnetization switch mechanism that only needs one ferromagnetic layer.

Spin-orbit torques can be related to inversion symmetry either in the bulk of a material or in thin film structures, resulting in a Rashba or a Dresselhaus spin-orbit coupling, respectively. Well known systems where such a lack of bulk inversion symmetry can be found are semiconductors with the zinc blende structure such as  $(\text{Ga},\text{Mn})\text{As}$  [49–51] or crystals from the B20 space group such as  $\text{FeGe}$  [52] and  $\text{MnSi}$  [53]

which show a chiral spin-orbit interaction, described by the rotationally invariant Dzyaloshinsky-Moriya (DM) interaction. In these systems, as a consequence, non-trivial spin structures can occur.

The broken inversion symmetry in these structures gives rise to a static electric field  $\mathbf{E}$  in the laboratory frame at rest, that in turn gives rise to a magnetic field  $\mathbf{B}$  in the reference frame of an object moving with momentum  $\hbar\mathbf{k}$ . Recently, experiments and theory indicated that also in ultrathin metallic multilayers with a built-in lack of inversion symmetry, Rashba spin-orbit coupling might be present. A static electric field  $\mathbf{E} = E_0 e_z$  in the laboratory rest frame, where  $e_z$  points normal to the surface of the multilayers, produces a magnetic field  $\mathbf{B} \propto k_x e_y - k_y e_x$  in the frame of the moving object, where  $k_x e_y - k_y e_x$  is known as the Rashba spin-orbit coupling.

Up to now, the ferromagnetic layer has either been asymmetrically sandwiched between a heavy metal layer and an oxide layer, e.g. Pt/Co/ $\text{AlO}_x$  or Ta/CoFeB/MgO [14, 54–57] or in periodic crystals that lack inversion symmetry like (Ga,Mn)As [49–51].

Two different torques are found in these experiments; one torque is an even function of the unit vector of magnetization direction  $\mathbf{m}$  and the other torque is an odd function of  $\mathbf{m}$ . Up to the lowest order, the even torque  $\mathbf{T}^{\parallel} = T^{\parallel} \mathbf{m} \times [(\hat{e}_z \times \mathbf{E}) \times \mathbf{m}]$ , where  $\mathbf{E}$  is the applied electric field and  $\hat{e}_z$  is a unit vector perpendicular to the interface of the ferromagnetic heterostructure, is expected to be driven by the spin current due to the spin Hall effect (SHE) in the heavy-metal layer. The torque has the same shape as the damping term in the Landau-Lifschitz-Gilbert equation and is then also called damping-like torque. The odd torque  $\mathbf{T}^{\perp} = T^{\perp} (\hat{e}_z \times \mathbf{E}) \times \mathbf{m}$  is expected to originate from the effective magnetic field due to spin dependent scattering in combination with the Rashba interaction, which originates from the broken inversion symmetry in the ferromagnetic heterostructures. This torque has the same shape as the field term in the Landau-Lifschitz-Gilbert equation and is then also called field-like torque.

However, there are theoretical predictions that the SHE can also be induced into a light normal metal like Cu or Al, when it is sandwiched between two different oxide layers or insulators [66], due to interfacial spin-orbit coupling. In this Chapter, we use ferromagnetic resonance and Hall measurements to show that also in an ultrathin Co layer sandwiched between  $\text{SiO}_x$  and Cu more damping is present than would be expected from the Cu layer, which only has weak bulk spin-orbit coupling. We attribute this to the Rashba spin-orbit torque induced by to the broken inversion symmetry. We investigate this in a way similar to

Chapter 5, by comparing  $\text{SiO}_x/\text{Co}(d)/\text{Cu}$  bilayers with  $\text{Cu}/\text{Co}(d)/\text{Cu}$  trilayers.

## 6.1 Experiment

The following films were grown:  $\text{Co}(d)/\text{Pt}(10)$ ,  $\text{Pt}(10)/\text{Co}(d)/\text{Pt}(10)$ ,  $\text{Co}(d)/\text{Cu}(10)$  and  $\text{Cu}(10)/\text{Co}(d)/\text{Cu}(10)$ . The numbers in parentheses represent the layer thickness in nanometers. They were deposited on naturally oxidized  $\text{Si}(100)$  in a UHV chamber (base pressure  $1 \cdot 10^{-9}$  mbar) using DC magnetron sputter deposition with argon as plasma at room temperature from 3N5 Co, 3N5 Cu and 3N5 Pt targets. To take into account both interfaces of the Co layer, we call the Co/Pt and Co/Cu bilayers in this Chapter  $\text{SiO}_x/\text{Co}/\text{Cu}$  and  $\text{SiO}_x/\text{Co}/\text{Pt}$ . Also, since the thicknesses of the Cu- and Pt-layers are not going to be varied, we call them  $\text{Co}(d)/\text{Pt}$  etc. The deposition rate was measured by X-ray reflectivity (XRR) using  $\text{Cu-K}\alpha$  radiation and was  $0.58 \text{ \AA}/\text{s}$  for Co,  $1.90 \text{ \AA}/\text{s}$  for Cu and  $1.54 \text{ \AA}/\text{s}$  for Pt respectively. Magnetization measurements were performed using the reciprocating sample option (RSO) in a SQUID-based magnetometer (MPMS XL-7 from Quantum Design). Ferromagnetic resonance (FMR) was measured using a Bruker EMX-plus X-band spectrometer in a  $\text{TE}_{011}$  cavity with 100 kHz modulation frequency and 1 G modulation amplitude with a maximum DC-field of 0.65 T. The sample was fixed on a Rexolite 1422 rod and a goniometer was used to vary the angle. For electrical characterization, the samples were patterned into Hall bar structures,  $50 \times 1000 \mu\text{m}^2$ , using negative resist, electron beam lithography and ion beam etching. Resistivity measurements were performed at room temperature using the lock-in technique, with a variable ac-current modulated at 1106 Hz.

## 6.2 Results

Figure 6.1.a shows the angular dependent peak-to-peak linewidth  $H_{\text{pp}}$  of the  $\text{SiO}_x/\text{Co}(2.6)/\text{Pt}$ ,  $\text{Pt}/\text{Co}(2.6)/\text{Pt}$ ,  $\text{SiO}_x/\text{Co}(2.6)/\text{Cu}$  and  $\text{Cu}/\text{Co}(2.6)/\text{Cu}$  multilayers. Clearly visible is that  $\Delta H_{\text{pp}}$  of the  $\text{Cu}/\text{Co}/\text{Cu}$  trilayer is much smaller than  $\Delta H_{\text{pp}}$  of the  $\text{Pt}/\text{Co}/\text{Pt}$  and  $\text{SiO}_x/\text{Co}/\text{Pt}$  films, but also much smaller than  $\Delta H_{\text{pp}}$  of the  $\text{SiO}_x/\text{Co}/\text{Cu}$  bilayer. In Figure 6.1.b, the angular dependent resonant fields  $H_r$  are plotted.  $H_r$  of the  $\text{Pt}/\text{Co}/\text{Pt}$  trilayer is larger than  $H_r$  of the other multilayers, for which  $H_r$  is almost the same.

In Figure 6.2, we take a closer look to the magnetic properties of the multilayers. The effective demagnetization fields  $4\pi M_{\text{eff}}$ , obtained from

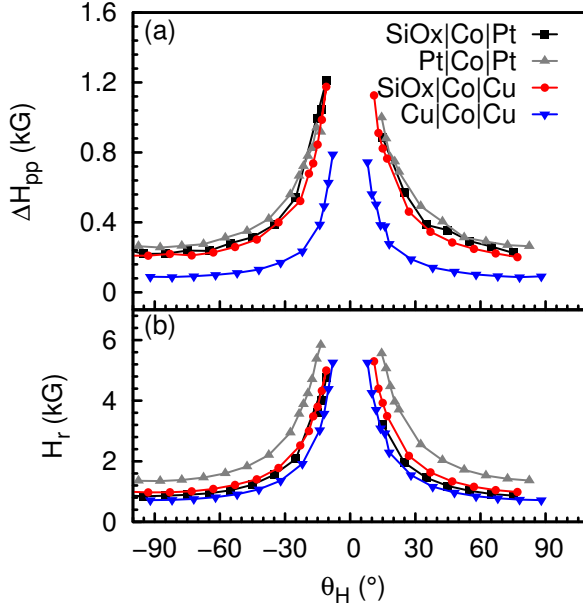


Figure 6.1: Angular dependence of the peak-to-peak linewidth  $H_{pp}$  (a) and the resonance field  $H_r$  (b) as a function of the applied field direction  $\theta_H$  for a  $\text{SiO}_x/\text{Co}(2.6)/\text{Pt}$  (black  $\blacksquare$ ),  $\text{SiO}_x/\text{Co}(2.6)/\text{Cu}$  (red  $\bullet$ ),  $\text{Cu}/\text{Co}(2.6)/\text{Cu}$  (blue  $\blacktriangledown$ ) and  $\text{Pt}/\text{Co}(2.6)/\text{Pt}$  (green  $\blacktriangle$ ) multilayers.

the analysis of the angular dependent FMR (see Chapter 5), and the saturation magnetization  $4\pi M_s$ , obtained using a magnetometer, are plotted as a function of the Co thickness  $d$ . The data for the  $\text{Pt}/\text{Co}(1.7)/\text{Pt}$  trilayer is not included in the analysis, as two resonance modes [152] are observed in this sample and the origin of this mode is not clear.

For large Co thicknesses,  $4\pi M_s$  reaches the saturation magnetization value of bulk Co in all samples, as indicated by the horizontal dotted line. In the  $\text{Pt}/\text{Co}/\text{Pt}$  and  $\text{SiO}_x/\text{Co}/\text{Pt}$  samples,  $4\pi M_s$  reaches the bulk saturation magnetization value also for small Co thicknesses. However, in the  $\text{Cu}/\text{Co}/\text{Cu}$  and  $\text{SiO}_x/\text{Co}/\text{Cu}$  samples,  $4\pi M_s$  becomes gradually smaller for thinner Co layers. For all samples,  $4\pi M_{\text{eff}}$  is lower than  $4\pi M_s$  of bulk Co. For the  $\text{Pt}/\text{Co}/\text{Pt}$  and  $\text{SiO}_x/\text{Co}/\text{Pt}$  samples,  $4\pi M_{\text{eff}}$  decreases rapidly with a decreasing Co thickness.  $4\pi M_{\text{eff}}$  decreases also for  $\text{Cu}/\text{Co}/\text{Cu}$  samples, but the change is much less than

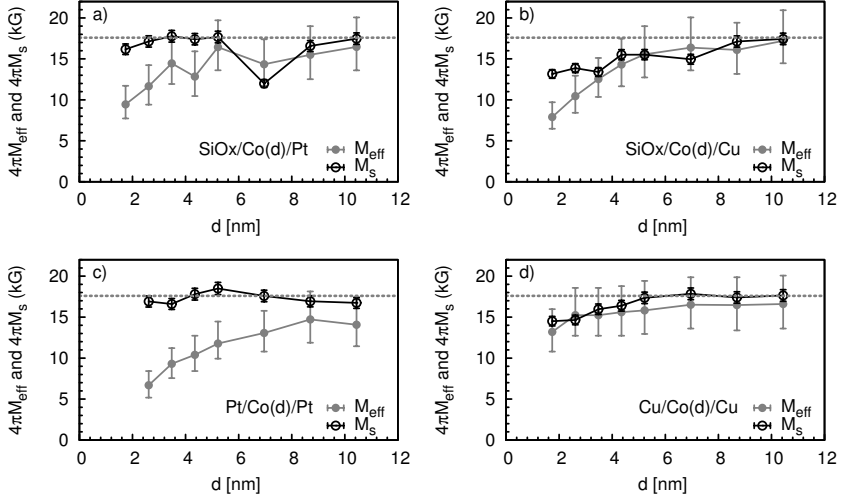


Figure 6.2: The effective demagnetization  $4\pi M_{\text{eff}}$  (closed symbols) and the saturation magnetization  $4\pi M_s$  (open symbols), as a function of the thickness  $d$  of the Co layer in (a) the  $\text{SiO}_x/\text{Co}/\text{Pt}$  bilayers; in (b) the  $\text{SiO}_x/\text{Co}/\text{Cu}$  bilayers, in (c) the  $\text{Pt}/\text{Co}(d)/\text{Pt}$  trilayers and in (d) the  $\text{Cu}/\text{Co}(d)/\text{Cu}$  trilayers.  $4\pi M_{\text{eff}}$  is the average value of 10 simulations with a  $g$ -factor between 1.8 and 2.2 [152] and the maximum and minimum value from this simulations. The dashed line indicates saturation magnetization of bulk Co.

for the  $\text{SiO}_x/\text{Co}/\text{Pt}$  and  $\text{Pt}/\text{Co}/\text{Pt}$  multilayers. The  $\text{SiO}_x/\text{Co}/\text{Cu}$  bilayers show a strong decrease in  $4\pi M_{\text{eff}}$ .

To compare  $4\pi M_{\text{eff}}$  between the different multilayers, this quantity is plotted in Figure 6.3.a for the  $\text{Cu}/\text{Co}(d)/\text{Cu}$  and  $\text{Pt}/\text{Co}(d)/\text{Pt}$  trilayers and in Figure 6.4.a for the  $\text{SiO}_x/\text{Co}(d)/\text{Pt}$  and a  $\text{SiO}_x/\text{Co}(d)/\text{Cu}$  bilayers. Clearly visible is that  $4\pi M_{\text{eff}}$  for both bilayers grown on  $\text{SiO}_x$  shows almost the same behavior. For thick Co layers,  $4\pi M_{\text{eff}}$  is lower than  $M_s$  of bulk Co. When decreasing the Co thickness  $d$ ,  $4\pi M_{\text{eff}}$  becomes smaller for both the  $\text{SiO}_x/\text{Co}/\text{Cu}$  and  $\text{SiO}_x/\text{Co}/\text{Pt}$  bilayers and both bilayers follow the same trend.

In Figure 6.3.b, the Gilbert damping  $\alpha$  is plotted for the  $\text{Cu}/\text{Co}(d)/\text{Cu}$  and  $\text{Pt}/\text{Co}(d)/\text{Pt}$  trilayers and in Figure 6.4.b for for the  $\text{SiO}_x/\text{Co}(d)/\text{Pt}$  and a  $\text{SiO}_x/\text{Co}(d)/\text{Cu}$  bilayers.  $\alpha$  in the  $\text{Pt}/\text{Co}/\text{Pt}$  trilayer increases rapidly, as Pt is a good spin sink. For the  $\text{Cu}/\text{Co}/\text{Cu}$  trilayer,  $\alpha$  is almost constant up to the lowest Co thickness, as Cu is a bad spin sink.

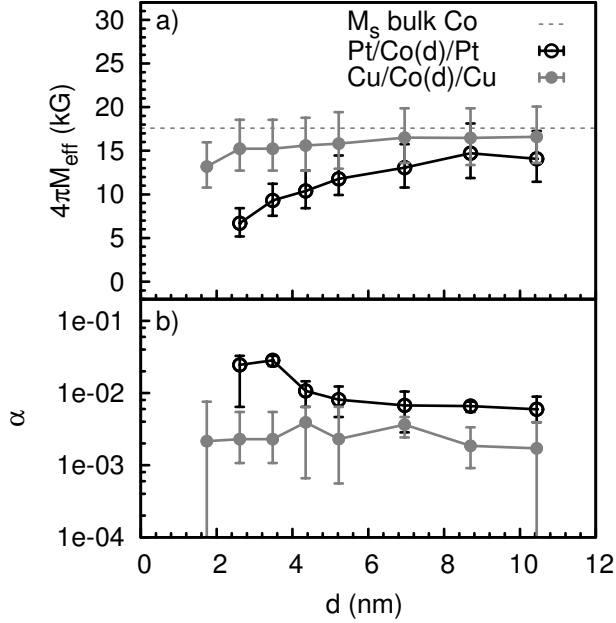


Figure 6.3: The effective demagnetization  $4\pi M_{\text{eff}}$  (a) and the damping  $\alpha$  (b), as a function of the thickness  $d$  of the Co layer in the Pt/Co( $d$ )/Pt (black  $\circ$ ) and Cu/Co( $d$ )/Cu (gray  $\bullet$ ) trilayers. Shown are the average values of 10 simulations with a  $g$ -factor between 1.8 and 2.2 [152] and the maximum and minimum value from this simulations.

The SiO<sub>x</sub>/Co/Pt bilayer shows also a rapid increase in  $\alpha$ . However, although Cu is a bad spin sink,  $\alpha$  of the SiO<sub>x</sub>/Co/Cu bilayer behaves *the same* as the SiO<sub>x</sub>/Co/Pt bilayer in contrast to what was seen in the trilayers.

Figure 6.5 shows the thickness dependence of the spatial variations in the direction of the easy axis  $\Delta(\theta_H)$  (a) and demagnetization field  $\Delta(4\pi M_{\text{eff}})$  (b) for the four multilayers, as obtained from analysis of the angular dependence of the FMR. For decreasing Co thicknesses, both  $\Delta(\theta_H)$  and  $\Delta(4\pi M_{\text{eff}})$  increase for all sets of multilayers.

In Figure 6.6.a, the perpendicular anisotropy field  $H_{\perp} = 4\pi M_s - 4\pi M_{\text{eff}}$ , where  $H_{\perp} = 2K_{\perp}/M_s$ , is plotted as a function of the inverse thickness of the Co layer. Clearly visible is that for all samples  $H_{\perp}$  is present.  $H_{\perp}$  is largest in the Pt/Co/Pt trilayer, followed by the SiO<sub>x</sub>/Co/Pt and SiO<sub>x</sub>/Co/Cu bilayers respectively while  $H_{\perp}$  of the Cu/Co/

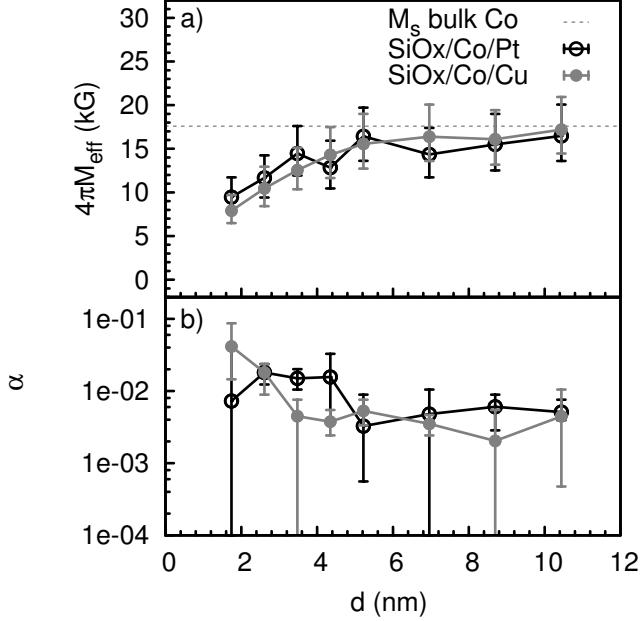


Figure 6.4: The effective demagnetization  $4\pi M_{\text{eff}}$  (a) and the damping  $\alpha$  (b), as a function of the thickness  $d$  of the Co layer in the SiO<sub>x</sub>/Co( $d$ )/Pt (black  $\circ$ ) and SiO<sub>x</sub>/Co( $d$ )/Cu (gray  $\bullet$ ) bilayers. Shown are the average values of 10 simulations with different  $g$ -factor and the maximum and minimum value from this simulations.

Cu trilayer is very small.  $K_{\perp}$  consists of a contribution of the anisotropy of the interface atoms  $K_s$  and the inner atoms of the magnetic layer  $K_v$  with thickness  $d$

$$K_{\perp} = K_v + 2\frac{K_s}{d}. \quad (6.1)$$

In Figure 6.6.b,  $K_{\perp}d$  is plotted as a function of the inverse thickness of the Co layer.  $K_{\perp}$  does not show a linear relation, as would be expected following equation 6.1. For larger Co thicknesses,  $K_{\perp}d$  is largest for the Pt/Co/Pt trilayer. When decreasing the Co thickness,  $K_{\perp}d$  increases for the Pt/Co/Pt trilayer, but decreases for the Cu/Co/Cu and SiO<sub>x</sub>/Co/Cu multilayers and varies for the SiO<sub>x</sub>/Co/Pt bilayer. For the thinnest Co layer,  $K_{\perp}d$  is almost the same for the SiO<sub>x</sub>/Co/Cu, SiO<sub>x</sub>/Co/Pt and Pt/Co/Pt multilayers.

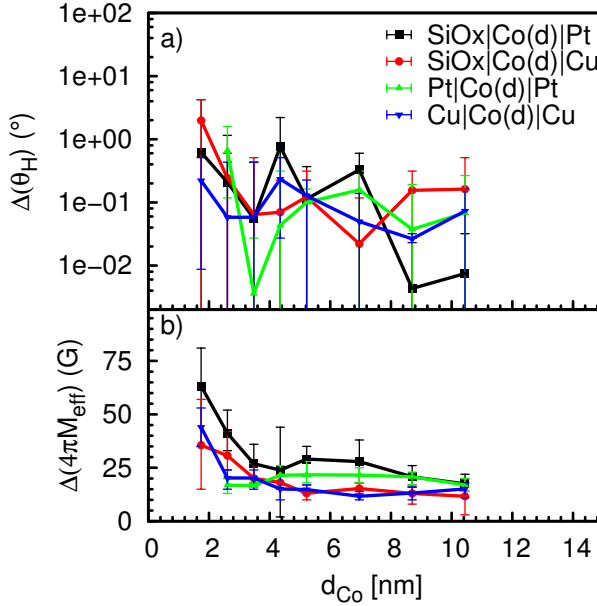


Figure 6.5: The spatial variations in the direction of the easy axis,  $\Delta(\theta_H)$  (a) and the effective demagnetization field,  $\Delta(4\pi M_{\text{eff}})$  (b), as a function of the thickness  $d$  of the Co layer in the  $\text{SiO}_x/\text{Co}(d)/\text{Pt}$  (black  $\blacksquare$ ),  $\text{SiO}_x/\text{Co}(d)/\text{Cu}$  (red  $\bullet$ ),  $\text{Cu}/\text{Co}(d)/\text{Cu}$  (blue  $\blacktriangledown$ ) and  $\text{Pt}/\text{Co}(d)/\text{Pt}$  (green  $\blacktriangle$ ) multilayers. Shown are the average values of 10 simulations with different  $g$ -factor and the maximum and minimum value from this simulations.

### 6.3 $\delta$ -doping with magnetic impurities

A possible explanation for the increased damping in the  $\text{SiO}_x/\text{Co}/\text{Cu}$  bilayers is the presence of magnetic impurities in the Cu layer. In deposition systems where magnetic materials are deposited, there is always a chance that other materials slowly become contaminated with the magnetic impurities. Adding magnetic impurities to a normal metal [22] or a superconductor [166] can dramatically change the properties of these materials. Furthermore, Niimi et al. showed that the spin Hall angle increases when Ir [63] and Bi [64] impurities are added to Cu.

To study the influence of magnetic impurities on the damping of the ferromagnetic layer, we used the  $\delta$ -doping technique as used before



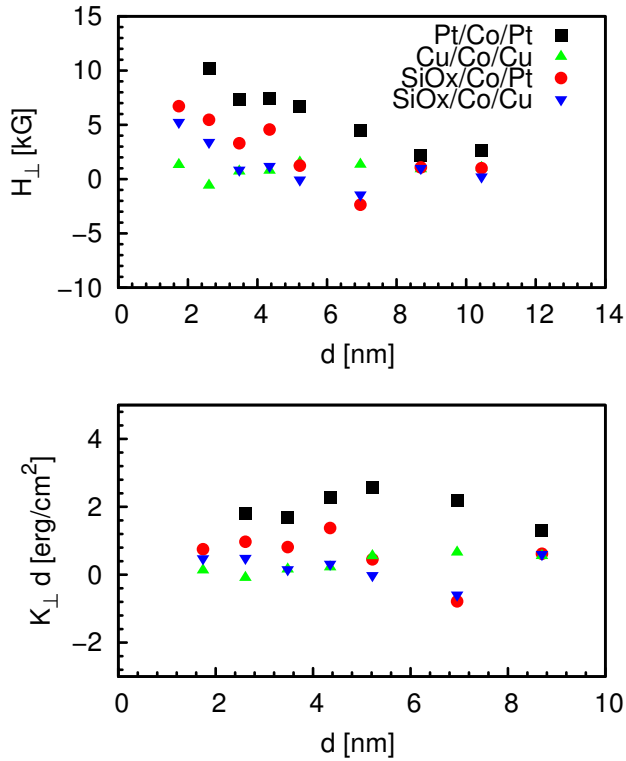


Figure 6.6: The perpendicular anisotropy field  $H_{\perp}$  (a) as a function of the Co thickness  $d$  and  $K_{\perp}d$  (b) and as a function of the inverse thickness of the Co layer for the Pt/Co( $d$ )/Pt (black  $\blacksquare$ ), SiO<sub>x</sub>/Co( $d$ )/Pt (red  $\bullet$ ), SiO<sub>x</sub>/Co( $d$ )/Cu (blue  $\blacktriangledown$ ) and Cu/Co( $d$ )/Cu (green  $\blacktriangle$ ) multilayers.

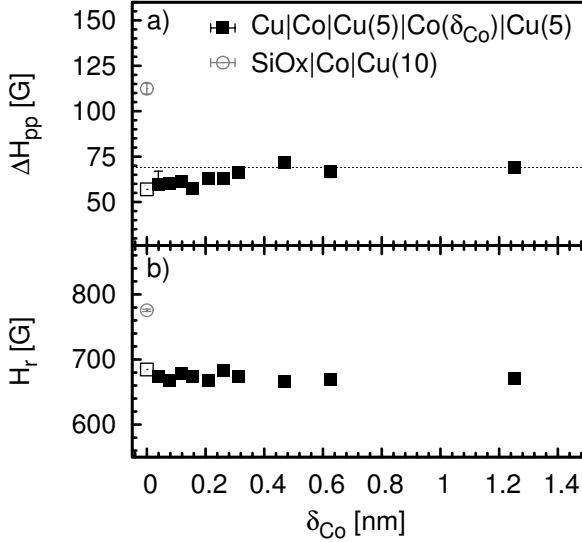


Figure 6.7: Peak-to-peak linewidth  $\Delta H_{pp}$  (a) and resonance field  $H_r$  (b) for Cu/Co(3.6)/Cu(5)Co( $\delta_{Co}$ )/Cu(5) multilayer as a function of the thickness of the Co impurity layer  $\delta_{Co}$  (black  $\blacksquare$ , with the point  $\delta_{Co} = 0$  indicated with a black  $\square$ ). As a reference, also  $\Delta H_{pp}$  and  $H_r$  of a SiO<sub>x</sub>/Co(3.6)/Cu bilayer are plotted (gray  $\circ$ ). As a guide for the eye, the grey dotted line indicates the maximum  $\Delta H_{pp}$ .

by Marrows and Hickey [167] to investigate the role of impurities in GMR systems. With the  $\delta$ -doping technique, a very thin magnetic layer is added to the multilayer. To study the effect of Co impurities on the SiO<sub>x</sub>/Co/Cu bilayer, we grew Cu/Co(3.6)/Cu(5)/Co( $\delta_{Co}$ )/Cu(5) multilayers where the thickness of the  $\delta_{Co}$  impurity layer is varied between 0 and 1.2 nm. For the growth of this very thin Co layers, a Co deposition rate of 0.13 Å/s was used.

Figure 6.7.a shows  $\Delta H_{pp}$  of Cu/Co(3.6)/Cu(5)/Co( $\delta_{Co}$ )/Cu(5) multilayers as a function of the Co impurity layer  $\delta_{Co}$ . Clearly visible is that  $\Delta H_{pp}$  increases as the thickness of the impurity layer increases and saturates already for a 0.32 nm thick impurity layer. In Figure 6.7.b,  $H_r$  of these samples is shown.  $H_r$  is almost constant for the whole impurity layer thickness range, which shows that the thickness of the 3.6 nm thick Co layer does not vary from sample to sample and the Co impurity layer does not couple to the thick Co layer. As a refer-

ence, in Figure 6.7 also  $\Delta H_{pp}$  and  $H_r$  of the  $\text{SiO}_x/\text{Co}(3.6)/\text{Cu}$  bilayer are shown. Clearly visible is that both values are much larger than for the  $\text{Cu}/\text{Co}(3.6)/\text{Cu}(5)\text{Co}(\delta_{\text{Co}})/\text{Cu}(5)$  multilayers, which indicates that magnetic impurities do not cause the large increase of the damping in  $\text{SiO}_x/\text{Co}/\text{Cu}$  bilayers.

## 6.4 Evaluation of the FMR measurements

The main point to be discussed is the observation of an unexpectedly large increase in the Gilbert damping and the resonance field in  $\text{SiO}_x/\text{Co}(d)/\text{Cu}$  bilayers with small Co thickness. This is unexpected in the sense that the Cu layer, which is supposed to be a bad spin sink, is not supposed to generate a spin pumping effect as seen by the FMR line broadening.

This is emphasized by the fact that the trilayers  $\text{Cu}/\text{Co}(d)/\text{Cu}$  and  $\text{Pt}/\text{Co}(d)/\text{Pt}$  show the difference expected for the good spin sink Pt and the bad spin sink Cu. The angular dependence of  $\Delta H_{pp}$  and  $H_r$  (Figure 6.1) and the extracted values for the damping parameter  $\alpha$  (Figure 6.3) show  $\alpha$  to be independent of  $d$  in the case of Cu, and increasing with decreasing  $d$  in the case of Pt, with more than an order of magnitude difference at the lowest thicknesses. Other parameters of the trilayer also behave in an understandable way. As shown in Figure 6.3.a,  $4\pi M_{\text{eff}}$  of the  $\text{Pt}/\text{Co}(d)/\text{Pt}$  trilayer decreases with decreasing  $d$ , due to the increasing perpendicular magnetic anisotropy (PMA). For the Cu case the decrease is smaller, as expected of the lower PMA of the Co/Cu interface.

For both types of trilayers,  $\Delta(\theta_H)$  and  $\Delta(4\pi M_{\text{eff}})$  becomes larger for very thin Co films. This is expected for very thin Co layers, as the roughness of the Cu and Pt buffer layer introduces  $\Delta(\theta_H)$  and  $\Delta(4\pi M_{\text{eff}})$  of the Co film and the exchange coupling is not strong enough to average out these variations [153]. Although for thicker Co films the roughness of the Cu and Pt buffer layer does not change, all magnetic moments in the Co film become parallel to the film plane. Furthermore, the spatial variation in both sets of trilayers shows the same order of variation as the data set of Mizukami et al. [153], that were used to derive the spin pumping theory [67].

In contrast, the behavior of the  $\text{SiO}_x/\text{Co}/\text{Cu}$  and  $\text{SiO}_x/\text{Co}/\text{Pt}$  bilayers does not show the expected behavior. The angular dependence of  $\Delta H_{pp}$  and  $H_r$  (Figure 6.1) and the extracted values for the damping parameter  $\alpha$  (Figure 6.4) show  $\alpha$  to be increasing with decreasing  $d$  in the case of both Cu and Pt.

Other parameters of the bilayer also do not behave in an understandable way. As shown in Figure 6.4.a,  $4\pi M_{\text{eff}}$  of the  $\text{SiO}_x/\text{Co}(d)/\text{Pt}$  and  $\text{SiO}_x/\text{Co}(d)/\text{Cu}$  bilayers both decrease with decreasing  $d$ . The increase of the PMA for very thin Co thicknesses in the  $\text{SiO}_x/\text{Co}/\text{Cu}$  bilayer is unexpected, as the influence of the interfacial anisotropy of the  $\text{SiO}_x/\text{Co}$  interface is negligible since  $K_s$  for a  $\text{SiO}_2/\text{Co}$  interface is of the same order as for a  $\text{Co}/\text{Cu}$  interface [168]. This shows that the huge increase in  $M_{\text{eff}}$  is probably not due to the PMA.

For both types of bilayers,  $\Delta(\theta_H)$  and  $\Delta(4\pi M_{\text{eff}})$  becomes larger for very thin Co films. The spatial variation in both sets of bilayers shows the same order of variation as the data set of the trilayers. Furthermore, the spin sink ability of the Cu can in principle be modified by adding magnetic impurities. But, the influence of magnetic impurities on the change in  $\Delta H_{\text{pp}}$  is only small, as can be seen in Figure 6.7.

The observed behaviour is not easy to explain using different magnetic anisotropies or growth related issues. The measurements suggest that there is an extra intrinsic damping mechanisms present in the bilayers. A possible candidate to furnish such a mechanism is the effect of the lack of inversion symmetry, which could give rise to Rashba- or spin Hall-like torques. From the FMR spectra, already a first estimate can be made of extra torques acting on the system. When we compare the  $\text{SiO}_x/\text{Co}/\text{Cu}$  and  $\text{Cu}/\text{Co}/\text{Cu}$  samples, and assume that the extra damping present in the  $\text{SiO}_x/\text{Co}/\text{Cu}$  bilayers is only due to the lack of inversion symmetry,  $H_r$  and  $H_{\text{pp}}$  are 262 and 113 G larger in the  $\text{SiO}_x/\text{Co}(2.6)/\text{Cu}$  bilayer than in the  $\text{Cu}/\text{Co}(2.6)/\text{Cu}$  trilayer. This indicates a field-like torque component of approximately 262 G while the spin transfer-like torque is approximately 113 G. This corresponds well with the size of the torques found very recently by Hall effect measurements in  $\text{AlO}_x(2)/\text{Co}(0.6)/\text{Pt}(3)$  trilayers [169].

In the next section, we look at the influence of the spin Hall effect on the FMR spectra, by sending a current through the Pt layer in a Co/Pt bilayer.

Furthermore, we will have a closer look at the possible existence of this Rashba spin-orbit torque. In particular, we look at the influence of the substrate and especially its dielectric properties. In the case of oxide interfaces involving  $\text{SrTiO}_3$ , which has a very high dielectric constant, it has been shown that the Rashba spin-orbit interaction can even be tuned with an electric field [170].

These extra torques can be also characterized using Hall measurements. We performed a first set of measurements of the Hall coefficients of a  $\text{SiO}_x/\text{Co}(2.6)/\text{Cu}$  bilayer and a  $\text{Cu}/\text{Co}(2.6)/\text{Cu}$  trilayer. Although the results give indications for the existence of extra torques, they are

not yet unequivocal and will be discussed in Appendix A.

## 6.5 Electric manipulation of the magnetization precession using the SHE

In Chapter 5, the spin current injected in the Pt layer was converted to an electric current using the inverse spin Hall effect. Ando et al. [58] showed that the reciprocal process is also possible. When a current is sent through the Pt layer, a spin current is generated via the spin Hall effect. This spin current  $J_s$  can manipulate the magnetization precession, which can be described as an extra torque  $\tau$

$$\tau = -\frac{\gamma J_s}{M_s A d} \mathbf{m} \times (\mathbf{m} \times \boldsymbol{\sigma}) \quad (6.2)$$

in the Landau-Lifshitz-Gilbert equation [58]. In this section, we want to know how much the spectrum of a SiO<sub>x</sub>/Co/Pt bilayer changes when a spin current is injected.

In Figure 6.8.a, the FMR spectra of a SiO<sub>x</sub>/Co(5)/Pt bilayer are shown where the magnetization relaxation is manipulated using the SHE. Using the same geometry used to measure  $V_{ISH}$ , see Figure 5.8, now a dc current is sent through the SiO<sub>x</sub>/Co(5)/Pt bilayer. The absorption derivative  $I$  is normalized by dividing the measured values by the maximum absorption derivative when no current is applied. When a current is sent through the bilayer,  $H_r$  increases. Furthermore,  $\Delta H_{pp}$  becomes smaller and the absorption derivative  $I$  becomes larger.

In Figure 6.8.b, the difference in the absorption derivative  $I$  for a positive current  $+J_c$  and negative current  $-J_c$  is shown. A clear resonance structure is visible, which demonstrates that the FMR spectra are significantly modified in response to current reversal [58]. This indicates that the magnetization relaxation depends on the current direction. When  $J_c > 0$  ( $J_c < 0$ ), the injected spin current exerts a spin torque on the magnetization that draws the magnetization towards (away) from the external magnetic field direction and thus modulates the Gilbert damping torque.

## 6.6 Substrate

In Figure 6.9,  $\Delta H_{pp}$  and  $H_r$  of a Co(3.6)/Cu bilayer grown at room-temperature on substrates of single crystal MgO (cubic,  $a = 0.421$ ), TiO<sub>2</sub> (tetragonal,  $a = b = 0.460$  nm,  $c = 0.296$ ) and Al<sub>2</sub>O<sub>3</sub> (hexagonal,  $a = 0.475$  nm,  $c = 1.299$ ) are shown for an in-plane magnetic field ( $\theta_H =$

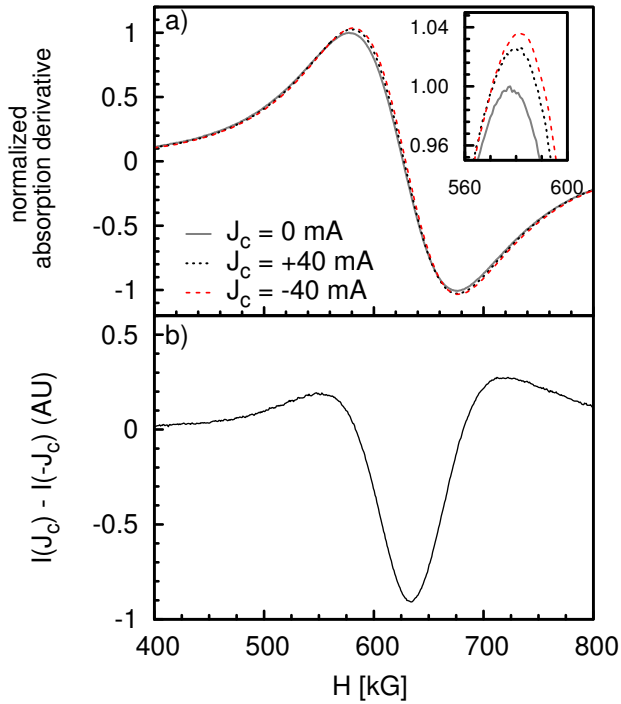


Figure 6.8: a) In-plane ( $\theta_H = 90^\circ$ ) FMR spectra of a  $\text{SiO}_x/\text{Co}(5)/\text{Pt}$  bilayer, where the relaxation is manipulated using the SHE. Using the same geometry used to measure  $V_{ISH}$ , see Figure 5.8, but now a dc current  $J_c$  is sent through the  $\text{SiO}_x/\text{Co}(5)/\text{Pt}$  bilayer. The absorption derivative is normalized by dividing the measured values by the maximum absorption derivative when no current is applied. The inset shows magnified views around the peaks of the spectra. b) The difference in the absorption derivative  $I$  for a positive current  $+J_c$  and negative current  $-J_c$  for an applied current of  $\pm 40$  mA.

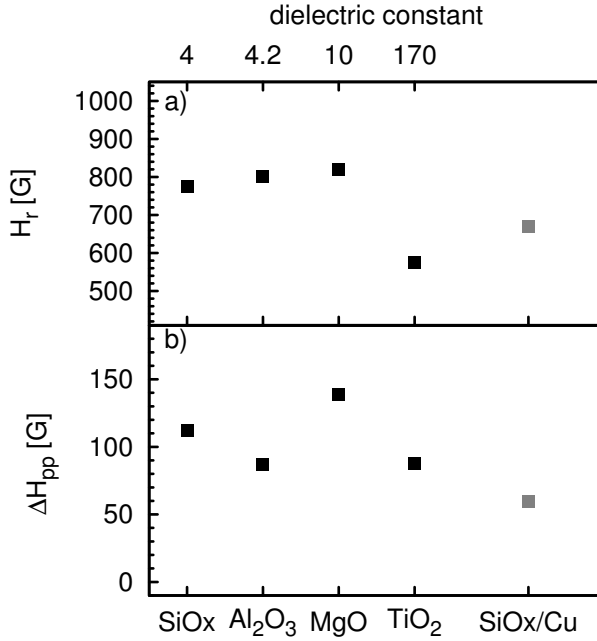


Figure 6.9: The resonance field  $H_r$  (a) and the peak-to-peak linewidth  $H_{pp}$  (b) of a Co(3.6)/Cu bilayer grown on a single crystal MgO, TiO<sub>2</sub>, Al<sub>2</sub>O<sub>3</sub> for an in-plane magnetic field ( $\theta_H = 90^\circ$ ). As a reference, also Si with a native oxide layer and a Cu buffer layer are shown.

90°). Clearly visible in Figure 6.9.a is that there is a slight variation in  $H_r$  for the SiO<sub>x</sub>, MgO and Al<sub>2</sub>O<sub>3</sub>, but  $H_r$  of the Co/Cu bilayer grown on TiO<sub>2</sub> and SiO<sub>x</sub>/Cu is much smaller.

$\Delta H_{pp}$ , as shown in Figure 6.9.b, shows however a different trend.  $\Delta H_{pp}$  of the Co/Cu bilayer grown on SiO<sub>x</sub>/Cu has the smallest linewidth, the bilayer grown on TiO<sub>2</sub> and Al<sub>2</sub>O<sub>3</sub> have almost the same linewidth and  $\Delta H_{pp}$  of the Co/Cu bilayer grown on MgO has the largest linewidth.

## 6.7 Discussion

Summarizing the experimental findings, for very thin Co thicknesses in SiO<sub>x</sub>/Co/Cu bilayers, an unexpected large increase in the Gilbert damping and resonance field is observed. In the last three sections, we also observed that the Hall measurements on a SiO<sub>x</sub>/Co/Cu bilayer

shows unexpected behavior. Furthermore, various substrates also result in a change of  $\Delta H_{pp}$  and  $H_r$ .

### **Electric manipulation of the magnetization precession using the SHE**

In Figure 6.8.a, the modified spectra of a  $\text{SiO}_x/\text{Co}(5)/\text{Pt}$  bilayer are shown. Even with a current of 40 mA, which would for a  $2.4 \times 2.4 \text{ mm}^2$  sample result in a current density of approximately  $1 \times 10^9 \text{ A/m}^2$ , only a change in  $\Delta H_{pp}$  of approximately 5 % was obtained. A small remark should be made, that the Co layer is 5 nm. When going to thinner Co films, already other mechanisms that influence the magnetization dynamics are more dominant.

Still, the influence of the electric manipulation of the magnetization precession using the SHE does not seem to be the dominant mechanism that results in a large increase of  $\Delta H_{pp}$  and  $H_r$ . Furthermore, the same large increase of  $\Delta H_{pp}$  and  $H_r$  is observed in  $\text{SiO}_x/\text{Co}/\text{Cu}$  bilayers. The spin Hall angle of Cu is much smaller than the spin Hall angle of Pt, therefore a spincurrent generated in a Cu layer due to the SHE will be much smaller than a spincurrent generated in a Pt layer due to the SHE. The change in  $H_r$  and  $\Delta H_{pp}$  are than expected to be very small in a  $\text{SiO}_x/\text{Co}/\text{Cu}$  bilayer.

### **Substrate**

When growing the  $\text{Co}(2.6)/\text{Cu}$  bilayer on different substrates, a big difference in the in-plane  $H_r$  and  $\Delta H_{pp}$  is visible, as shown in Figure 6.9. These bilayers were grown in the same deposition run, so the sample-to-sample growth variation of the  $\text{Co}(2.6)/\text{Cu}$  bilayer is very small, but no effort was made to optimize the growth to obtain epitaxial layers. However, there are a few differences between the samples. First, the  $\text{Co}/\text{Cu}$  bilayer grows probably slightly different on each substrate, because the lattice constants of each substrate is slightly different. Secondly, the interface between the Co and the substrate is different, resulting in a different interface anisotropy  $K_s$  and thus also a different PMA,  $M_{\text{eff}}$  and  $H_r$ . Monso et al. [171, 172] and Yang et al. [173] showed that despite the weak spin-orbit interaction at the interface, a PMA is observed for the substrate/Co interface that is comparable to or even larger than a  $\text{Co}/\text{Pt}$  or  $\text{Co}/\text{Pd}$  interface.  $H_r$  in Figure 6.9.b show a slow increase for a  $\text{SiO}_x$ ,  $\text{Al}_2\text{O}_3$  and  $\text{MgO}$  substrate, but a dramatic decrease (75 % of the  $H_r$  of  $\text{SiO}_x$ ) for the the  $\text{TiO}_2$  substrate. The in-plane resonance condition, equation 5.9, indicates that such a large decrease in



$H_r$  would correspond to a considerable change of either the  $g$ -factor or  $M_{\text{eff}}$ .

However, such a large change in  $M_{\text{eff}}$  or the  $g$ -factor is not likely, which suggests a negative field-like torque, due to the broken inversion symmetry. The very large dielectric constant of  $\text{TiO}_2$ , which is more than 40 times as large as the dielectric constant of  $\text{Al}_2\text{O}_3$ , might even further increase the size of this field-like torque.

Although  $H_r$  of the  $\text{TiO}_2/\text{Co}(2.6)/\text{Cu}$  bilayer is much smaller than to the  $\text{Co}(2.6)/\text{Cu}$  bilayer grown on the other substrates,  $\Delta H_{\text{pp}}$  is almost the same as the  $\text{Al}_2\text{O}_3/\text{Co}(2.6)/\text{Cu}$  bilayer as shown in Figure 6.9.a.  $\Delta H_{\text{pp}}$  of the  $\text{Co}(2.6)/\text{Cu}$  bilayer grown on  $\text{MgO}$  and  $\text{SiO}_x$  are much larger. However, without a full angular dependence analysis, the different contributions to  $\Delta H_{\text{pp}}$  cannot easily be identified.

To conclude, we observe a large increase in the damping, and a change in the resonance field, for thin Co films in asymmetric  $\text{SiO}_x/\text{Co}(d)/\text{Cu}$  bilayers. This effect is absent in symmetric  $\text{Cu}/\text{Co}/\text{Cu}$  trilayers, and therefore not attributable to spin pumping effects. We suggest that this is due to the presence of spin-orbit torques caused by the broken inversion symmetry of the ferromagnetic heterostructures. We note that the effects are not small, with a field-like torque contribution of about 250 G, and a spin-transfer-like contribution of the order of 100 G.



## Hall measurements

The presence of a spin-orbit torque (SOT) can also be investigated using Hall measurements. In Figure A.1 a schematic diagram is shown to measure the Hall voltages. When current flows through the device under test, the current can induce an effective field  $\Delta\mathbf{H}$ , which consists of the Oersted field, the STT-field and the SOT-fields. This effective field can modify the polar angle  $\theta_M$  and azimuthal angle  $\phi_M$  of the magnetization direction from the equilibrium value  $(\theta_{M0}, \phi_{M0})$  by a small angle ( $\Delta\theta_M$  and  $\Delta\phi_M \ll 1$ ), where  $\Delta\theta_M$  and  $\Delta\phi_M$  are the change in the polar and azimuthal magnetization angle. They are then equal to

$$\theta_M = \theta_{M0} + \Delta\theta_M, \quad (\text{A.1})$$

$$\phi_M = \phi_{M0} + \Delta\phi_M, \quad (\text{A.2})$$

where  $\Delta\theta_M$  and  $\Delta\phi_M$  can be derived from the total free energy  $F$  per unit volume of magnetization of the film (equation 5.3) [174].

The Hall voltage  $V_H$  in a ferromagnet contains a contribution of the anomalous Hall effect (AHE) and the planar Hall effect (PHE) [175]

$$V_H = I [R_{\text{AHE}} \cos \theta_M + R_{\text{PHE}} \sin^2 \theta_M \sin 2\phi_M], \quad (\text{A.3})$$

where  $R_{\text{AHE}}$  and  $R_{\text{PHE}}$  are the contributions in the Hall resistance due to the AHE and PHE, and  $I$  is the bias current. An oscillating current  $I_{\text{ac}} \sin \omega t$  is used to induce an effective field modulation  $\Delta\mathbf{H} \sin \omega t$  that can modify the magnetization direction. When equations A.1 and A.2

are substituted in equation A.3, the Hall voltage is equal to [174]

$$V_{XX}(\theta_H, \phi_H) = V_0(\theta_H, \phi_H) + V_\omega(\theta_H, \phi_H) \sin \omega t + V_{2\omega}(\theta_H, \phi_H) \cos 2\omega t, \quad (\text{A.4})$$

where the coefficients  $V_0(\theta_H, \phi_H)$ ,  $V_\omega(\theta_H, \phi_H)$  and  $V_{2\omega}(\theta_H, \phi_H)$  depend on the system studied [174].

The first harmonic term  $V_\omega$  relates to the equilibrium direction of the magnetization and is independent of the modulated fields. The second harmonic term  $V_{2\omega}$  measures the change from the equilibrium direction of the magnetization due to the current-induced fields. By studying the angular dependence of the harmonic terms, the symmetry of the SOI can be derived from which the physical mechanism can be reconstructed. Note that, in equation A.3, the first harmonic term is in-phase with the driving current, while the second harmonic term is out-of-phase. The measurements were performed by using two lock-in detectors for the longitudinal and transverse voltages, respectively.

Figures A.2 and A.3 show our first measurements of the Hall coefficients for the  $\text{SiO}_x/\text{Co}(2.6)/\text{Cu}$  bilayer and  $\text{Cu}/\text{Co}(2.6)/\text{Cu}$  trilayer as a function of the applied magnetic field. The current density used to measure the Hall voltages is different for both samples. For the  $\text{SiO}_x/\text{Co}/\text{Cu}$ , a much larger current density was needed to have a reasonable signal-noise ratio.

A clear difference between both samples is visible. The in-phase first harmonic term of the  $\text{Cu}/\text{Co}(2.6)/\text{Cu}$  trilayer shows parabolic behaviour (Figure A.3.a and c) and when the first harmonic term is split

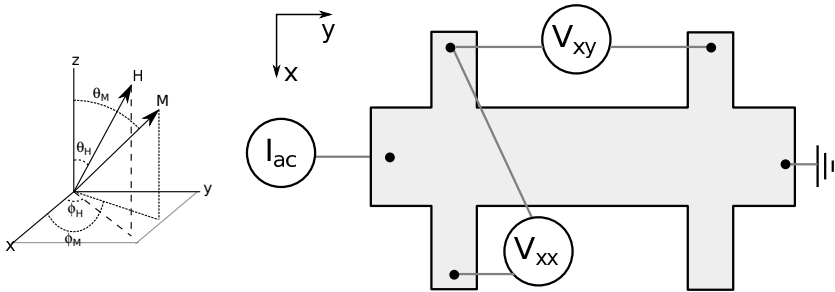


Figure A.1: Coordinate system used for the Hall measurements. A current  $I_{ac}$  is applied along the  $y$ -direction and a magnetic field is applied along the  $x$ -direction ( $\theta_M = 90^\circ$ ,  $\phi_M = 0^\circ$ ), and the Hall voltage  $V_{xx}$  is measured along the  $x$ -direction.

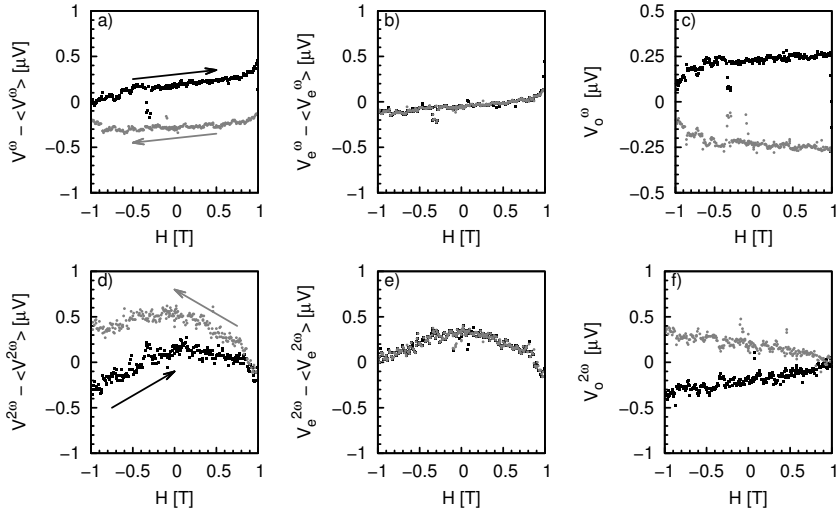


Figure A.2: Hall measurements on the  $\text{SiO}_x/\text{Co}(2.6)/\text{Cu}$  bilayer with  $I_{ac} = 40$  mA (current density is  $6 \cdot 10^{10}$  A/m<sup>2</sup>). The in-phase first harmonic term  $V^\omega$  is shown in a), where b) is the even part  $V_e^\omega$  and d) the odd part  $V_o^\omega$  of the first harmonic term respectively. d–f) show the out-of-phase component of the second harmonic term  $V^{2\omega}$ , which can also be split in an even and odd part. The arrows indicate the direction of the magnetic field sweep. For clarity, a constant offset  $\langle V \rangle$  is subtracted from the harmonic terms.

into even and odd parts, the even term shows also a parabola while the odd term is virtually absent. The  $\text{SiO}_x/\text{Co}/\text{Cu}$  bilayer shows different behaviour for the first harmonic term. First, there is a large offset present, which is removed in Figure A.2. Secondly, no parabola is visible, but the first harmonic term is linear and there is an offset between the measured voltage for the up and down magnetic sweep. Furthermore, at -1 T the measured voltage of the up and down sweep bend to each other which is clearly visible in Figures A.2.c, whereas at +1 T both sweeps bent in the same direction.

For both samples the out-of-phase second harmonic term shows behaviour very similar to the first harmonic term. The  $\text{Cu}/\text{Co}/\text{Cu}$  trilayer again shows a parabola. The  $\text{SiO}_x/\text{Co}/\text{Cu}$  bilayer again shows linear behaviour, but there is now a clear bend visible around 0 T as is shown in Figures A.2.d. When the second harmonic term is split into an odd and even part, the even part now also looks like a parabola (see Fig-

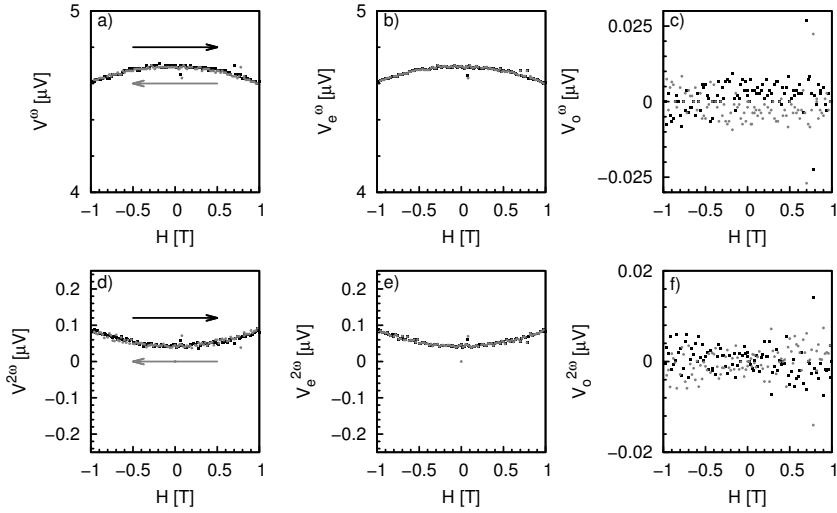


Figure A.3: Hall measurements on the Cu/Co(2.6)/Cu trilayer with  $I_{ac} = 1$  mA (current density  $9 \cdot 10^8$  A/m<sup>2</sup>). The in-phase first harmonic term  $V_x^\omega$  is shown in a), where b) is the even part  $V_e^\omega$  and c) the odd part  $V_o^\omega$  of the first harmonic term respectively. d–f) show the out-of-phase component of the second harmonic term  $V_x^{2\omega}$ , which can also be split in an even and odd part. The arrows indicate the direction of the magnetic field sweep.

ure A.2.e) and the odd part is linear while both branches appear to cross each other at approximately +1 T (see Figures A.2.f), which happens to be the maximum field of the sweep.

## A.1 Discussion

Summarizing the provisional experimental findings, the Hall measurements of a SiO<sub>x</sub>/Co(2.6)/Cu bilayer and a Cu/Co(2.6)/Cu trilayer show very different behaviour. The spin Hall angle of Cu is very small, so no influence of the SHE and Rashba effect is expected for the Cu/Co(2.6)/Cu trilayer. This was already confirmed in Chapter 6 using FMR measurements on Cu/Co/Cu trilayers. However, in the SiO<sub>x</sub>/Co(2.6)/Cu bilayer, broken inversion symmetry is present which resulted in an unexpected large damping in FMR measurements.

In Figure A.3.a the in-phase first harmonic coefficient of the Cu/Co(2.6)/Cu trilayer shows parabolic behaviour. The first harmonic co-

efficient is due to the equilibrium magnetization. Figures A.3.b and c show that the measured in-phase first harmonic coefficient consist mostly of an even, planar Hall, term. In contrast the in-phase first harmonic coefficient of the  $\text{SiO}_x/\text{Co}(2.6)/\text{Cu}$  bilayer now consists now of an even, planar Hall, term and an odd, anomalous Hall, term. We do not yet fully understand the behaviour of this bilayer with a built-in lack of inversion symmetry and although both samples were glued on the same sample holder, a small misalignment could be present.

Pi et al. [176] measured the in-phase first and out-of-phase second harmonic coefficients of a  $\text{Ta}(5)/\text{Pt}(3)/\text{Co}(0.6)/\text{AlO}_x(1.8)$  and a  $\text{Ta}(5)/\text{Pt}(3)/\text{Co}(0.6)/\text{Pt}(3)$  multilayer and they noticed a clear difference between the symmetric  $\text{Pt}/\text{Co}/\text{Pt}$  trilayer and asymmetric  $\text{Pt}/\text{Co}/\text{AlO}_x$  trilayer. Whereas the out-of-phase second harmonic coefficient of the asymmetric trilayer shows a parabolic shape, the measured out-of-phase second harmonic coefficient of the symmetric trilayer shows a negligible signal. They contribute the difference between the symmetric and asymmetric trilayer to the presence of a Rashba field in the asymmetric trilayer.

Hall measurements done on other metallic asymmetric multilayers [59, 169, 176, 177] suggest that beside the Rashba SOT also a spin Hall SOT exists. Kim et al. [59] showed for a  $\text{Si}/\text{Ta}(d)/\text{CoFeB}(1)/\text{MgO}(2)/\text{Ta}(1)$  multilayer that the odd part of the second harmonic coefficient consists of two linear signals, lines, where each line corresponds to an initial perpendicular magnetization orientation, that cross each other at a certain field. For a Ta bottom layer of 1 nm, the lines cross each other at zero field. When decreasing the thickness of the Ta bottom layer to 0.1 nm, they observe that both lines cross each other now at -0.1 T. They attribute this change in crossing field to a change from the spin Hall SOT for larger Ta thicknesses to the Rashba SOT for very small Ta thicknesses. In our  $\text{SiO}_x/\text{Co}(2.6)/\text{Cu}$  multilayer, we observe that the lines cross at a finite field although we did not create a well-defined initial magnetization orientation. The non-zero crossing suggests that a Rashba SOT is present in our  $\text{SiO}_x/\text{Co}(2.6)/\text{Cu}$  bilayer. However, the crossing of the up- and down-sweep happens around the maximum field of our magnet (+1 T) so that a full crossing cannot be observed, and the hysteresis present in the second harmonic shows similarity with the hysteresis present in the first harmonic coefficient.

The presence of a second harmonic coefficient indicates that there is a current induced field present. Beside the SOT, the applied current can also produce an Oersted field and heating. Ohmic heating is independent of external field and current directions and increases the temperature of the sample. The increase in temperature decreases the magnetic

anisotropy field and the saturation magnetization of the magnetic layer. Garelo et al. [169] showed that heating effects are most clearly visible in the third harmonic coefficient, which is not measured in our experiment. Heating also appears as a contribution to the second harmonic coefficient, but heating effects have only a minor influence on the spin torque measurements [169]. The resistance of the  $50 \times 1000 \mu\text{m}^2$  Cu/Co(2.6)/Cu Hallbar is approximately  $90 \Omega$ , so current of 1 mA generates approximately 0.1 mW of heat, well below the 40 mW that was dissipated in a  $10 \times 60 \mu\text{m}^2$  Ta(1)/CoFeB(1)/MgO(2)/Ta(1) Hallbar used in the experiments of Kim et al. [59], that gave rise to a temperature increase of the wire of approximately 10 K. For the Cu/Co/Cu and SiO<sub>x</sub>/Co/Cu multilayers, the Oersted fields are approximately 0.1 G and 5 G respectively, smaller than the values of the SOT fields from the FMR data and other experiments [59, 169]. So we expect that the influence of the current induced heating and Oersted field are small.

Ryu et al. [178] and Emori et al. [177] showed that domain walls in Ta(3)/Pt(3)/CoFeB(0.6)/MgO(1.8)/Ta(2), Ta(5)/CoFeB(0.6)/MgO(1.8)/Ta(2) and TaN(2)/Pt(1.5)/Co(0.3)/Ni(0.7)/Co(0.15)/TaN(5) multilayers flow against the electron flow. Although the multilayers are asymmetric and contain heavy metals, the direction of the induced Rashba and spin Hall torque cannot explain the movement of the domain walls against the electron flow. The Dzyaloshinskii-Moriya interaction (DMI) needs to be taken into account to explain this observation. Moon et al. [179] and Cortés-Ortuño and Landeros [180] calculated how the DMI would change the spin-wave dispersion. An et al. [181] measured using the Brillouin light scattering technique the spin wave spectrum of a CoFeB/Ta bilayer and showed that the spin wave amplitude can be attenuated or amplified depending on the direction of the applied current and magnetic field. Still, with FMR only the  $k = 0$  wavevector is probed and the DMI should not have effect on the measured FMR spectrum. Nonetheless, the DMI can play an important role in the Hall measurements. It does not explain the huge increase in  $\Delta H_{pp}$  in the FMR spectra of the SiO<sub>x</sub>/Co(*d*)/Cu and SiO<sub>x</sub>/Co(2.6)/Pt multilayers.

To conclude, we tentatively attribute the observed odd out-of-phase second harmonic coefficient in the SiO<sub>x</sub>/Co(2.6)/Cu bilayer to the Rashba SOT.



# Bibliography

- [1] <http://www.mv.helsinki.fi/aphalo/photobio/lamps.html>.
- [2] N. Zheludev. The life and times of the led — a 100-year history. *Nat Photon* **1**, 189 (2007).
- [3] H. Round. A note on carborundum. *Electr. World* **49**, 309 (1907).
- [4] O. Lossev. Luminous carborundum detector and detection effect and oscillations with crystals. *Philosophical Magazine Series 7* **6**, 1024 (1928).
- [5] R. N. Hall, G. E. Fenner, J. D. Kingsley, T. J. Soltys and R. O. Carlson. Coherent light emission from GaAs junctions. *Phys. Rev. Lett.* **9**, 366 (1962).
- [6] M. I. Nathan, W. P. Dumke, G. Burns, J. F. H. Dill and G. Lasher. Stimulated emission of radiation from GaAs p-n junctions. *Applied Physics Letters* **1**, 62 (1962).
- [7] T. M. Quist, R. H. Rediker, R. J. Keyes, W. E. Krag, B. Lax, A. L. McWhorter and H. J. Zeigler. Semiconductor maser of GaAs. *Applied Physics Letters* **1**, 91 (1962).
- [8] J. N. Holonyak and S. F. Bevacqua. Coherent (visible) light emission from Ga(As<sub>1-x</sub>P<sub>x</sub>) junctions. *Applied Physics Letters* **1**, 82 (1962).
- [9] <http://en.wikipedia.org/wiki/File:PnJunction-LED-E.svg>.
- [10] [http://upload.wikimedia.org/wikipedia/commons/0/09/Stimulated\\_-\\_Emission.svg](http://upload.wikimedia.org/wikipedia/commons/0/09/Stimulated_-_Emission.svg).
- [11] M. Tonouchi. Cutting-edge terahertz technology. *Nat Photon* **1**, 97 (2007).
- [12] L. Berger. Emission of spin waves by a magnetic multilayer traversed by a current. *Phys. Rev. B* **54**, 9353 (1996).
- [13] J. Slonczewski. Current-driven excitation of magnetic multilayers. *Journal of Magnetism and Magnetic Materials* **159**, L1 (1996).
- [14] I. M. Miron, K. Garello, G. Gaudin, P.-J. Zermatten, M. V. Costache, S. Auffret, S. Bandiera, B. Rodmacq, A. Schuhl and P. Gambardella. Perpendicular switching of a single ferromagnetic layer induced by in-plane current injection. *Nature* **476**, 189 (2011).
- [15] J. E. Hirsch. Spin Hall effect. *Phys. Rev. Lett.* **83**, 1834 (1999).

- [16] K. Uchida, S. Takahashi, K. Harii, J. Ieda, W. Koshibae, K. Ando, S. Maekawa and E. Saitoh. Observation of the spin seebeck effect. *Nature* **455**, 778 (2008).
- [17] K. Uchida, H. Adachi, D. Kikuchi, S. Ito, Z. Qiu, S. Maekawa and E. Saitoh. Plasmonic generation of spin currents. *ArXiv e-prints* (2013). 1308.3532.
- [18] A. Kadigrobov, Z. Ivanov, T. Claeson, R. I. Shekhter and M. Jonson. Giant lasing effect in magnetic nanoconductors. *EPL (Europhysics Letters)* **67**, 948 (2004).
- [19] A. Kadigrobov, R. I. Shekhter and M. Jonson. Novel laser based on magnetic tunneling. *Low Temperature Physics* **31**, 352 (2005).
- [20] S. Blundell. *Magnetism in condensed matter*. Oxford University Press (2001).
- [21] R. O’Handley. *Modern magnetic materials*. John Wiley & Sons, Ltd (2000).
- [22] J. Kondo. Resistance minimum in dilute magnetic alloys. *Progress of Theoretical Physics* **32**, 37 (1964).
- [23] T. Jungwirth, J. Wunderlich and K. Olejnik. Spin Hall effect devices. *Nat Mater* **11**, 382 (2012).
- [24] W. Pauli. Zur quantenmechanik des magnetischen elektrons. *Zeitschrift fur Physik* **43**, 601 (1927).
- [25] S. Maekawa and S. Takahashi. *Spin Current*. Oxford University Press (2012).
- [26] S. Zhang. Spin Hall effect in the presence of spin diffusion. *Phys. Rev. Lett.* **85**, 393 (2000).
- [27] J. Bass and W. P. Pratt. Spin-diffusion lengths in metals and alloys, and spin-flipping at metal/metal interfaces: an experimentalist’s critical review. *Journal of Physics: Condensed Matter* **19**, 183201 (2007).
- [28] S. Murakami, N. Nagaosa and S.-C. Zhang. Dissipationless quantum spin current at room temperature. *Science* **301**, 1348 (2003).
- [29] M. N. Baibich, J. M. Broto, A. Fert, F. N. Van Dau, F. Petroff, P. Etienne, G. Creuzet, A. Friederich and J. Chazelas. Giant magnetoresistance of (001)Fe/(001)Cr magnetic superlattices. *Phys. Rev. Lett.* **61**, 2472 (1988).
- [30] G. Binasch, P. Grünberg, F. Saurenbach and W. Zinn. Enhanced magnetoresistance in layered magnetic structures with antiferromagnetic interlayer exchange. *Phys. Rev. B* **39**, 4828 (1989).
- [31] T. Valet and A. Fert. Theory of the perpendicular magnetoresistance in magnetic multilayers. *Phys. Rev. B* **48**, 7099 (1993).
- [32] A. Brataas, G. E. Bauer and P. J. Kelly. Non-collinear magnetoelectronics. *Physics Reports* **427**, 157 (2006).
- [33] A. Brataas, Y. V. Nazarov and G. E. W. Bauer. Finite-element theory of transport in ferromagnet-normal metal systems. *Phys. Rev. Lett.* **84**, 2481 (2000).

- [34] M. Zaffalon. *Spin Accumulation in Ferromagnetic/Normal and Ferromagnetic/Superconducting Systems*. Ph.D. thesis, Rijksuniversiteit Groningen (2006).
- [35] M. Tsoi, A. G. M. Jansen, J. Bass, W.-C. Chiang, M. Seck, V. Tsoi and P. Wyder. Excitation of a magnetic multilayer by an electric current. *Phys. Rev. Lett.* **80**, 4281 (1998).
- [36] E. Myers, D. Ralph, J. Katine, R. Louie and R. Buhrman. Current-induced switching of domains in magnetic multilayer devices. *Science* **285**, 867 (1999).
- [37] S. I. Kiselev, J. C. Sankey, I. N. Krivorotov, N. C. Emley, R. J. Schoelkopf, R. A. Buhrman and D. C. Ralph. Microwave oscillations of a nanomagnet driven by a spin-polarized current. *Nature* **425**, 380 (2003).
- [38] L. Landau and E. Lifshitz. On the theory of the dispersion of magnetic permeability in ferromagnetic bodies. *Physikalische Zeitschrift der Sowjetunion* **8**, 153 (1935).
- [39] T. L. Gilbert. A Lagrangian formulation of the gyromagnetic equation of the magnetization fields. *Phys. Rev.* **100**, 1243 (1955). The original reference in Physical Review is only an abstract for an APS Meeting. The full report was written published as "Armor Research Foundation Project No. A059, Supplementary Report, May 1, 1956".
- [40] T. Gilbert. A phenomenological theory of damping in ferromagnetic materials. *Magnetics, IEEE Transactions on* **40**, 3443 (2004).
- [41] B. Heinrich. Spin relaxation in magnetic metallic layers and multilayers. In J. Bland and B. Heinrich, editors, *Ultrathin Magnetic Structures III*, pages 143–210–. Springer Berlin Heidelberg (2005).
- [42] S. M. Bhagat and P. Lubitz. Temperature variation of ferromagnetic relaxation in the 3d transition metals. *Phys. Rev. B* **10**, 179 (1974).
- [43] Y. Tserkovnyak, A. Brataas, G. E. W. Bauer and B. I. Halperin. Nonlocal magnetization dynamics in ferromagnetic heterostructures. *Rev. Mod. Phys.* **77**, 1375 (2005).
- [44] K. Xia, P. J. Kelly, G. E. W. Bauer, A. Brataas and I. Turek. Spin torques in ferromagnetic/normal-metal structures. *Phys. Rev. B* **65**, 220401 (2002).
- [45] D. Ralph and M. Stiles. Spin transfer torques. *Journal of Magnetism and Magnetic Materials* **320**, 1190 (2008).
- [46] V. Galitski and I. B. Spielman. Spin-orbit coupling in quantum gases. *Nature* **494**, 49 (2013).
- [47] H.-A. Engel, E. I. Rashba and B. I. Halperin. *Theory of Spin Hall Effects in Semiconductors*, chapter Theory of Spin Hall Effects in Semiconductors. John Wiley & Sons, Ltd (2007). ISBN 9780470022184.
- [48] E. van der Bijl and R. A. Duine. Current-induced torques in textured Rashba ferromagnets. *Phys. Rev. B* **86**, 094406 (2012).

- [49] A. Chernyshov, M. Overby, X. Liu, J. K. Furdyna, Y. Lyanda-Geller and L. P. Rokhinson. Evidence for reversible control of magnetization in a ferromagnetic material by means of spin-orbit magnetic field. *Nat Phys* **5**, 656 (2009).
- [50] M. Endo, F. Matsukura and H. Ohno. Current induced effective magnetic field and magnetization reversal in uniaxial anisotropy (Ga,Mn)As. *Applied Physics Letters* **97**, 222501 (2010).
- [51] H. Kurebayashi, J. Sinova, D. Fang, A. C. Irvine, J. Wunderlich, V. Novak, R. P. Campion, B. L. Gallagher, E. K. Vehstedt, L. P. Zarbo, K. Vyborny, A. J. Ferguson and T. Jungwirth. Observation of a Berry phase anti-damping spin-orbit torque. *ArXiv e-prints* (2013). 1306.1893.
- [52] X. Z. Yu, N. Kanazawa, Y. Onose, K. Kimoto, W. Z. Zhang, S. Ishiwata, Y. Matsui and Y. Tokura. Near room-temperature formation of a skyrmion crystal in thin-films of the helimagnet FeGe. *Nat Mater* **10**, 106 (2011).
- [53] F. Jonietz, S. Mühlbauer, C. Pfleiderer, A. Neubauer, W. Münzer, A. Bauer, T. Adams, R. Georgii, P. Böni, R. A. Duine, K. Everschor, M. Garst and A. Rosch. Spin transfer torques in MnSi at ultralow current densities. *Science* **330**, 1648 (2010).
- [54] I. M. Miron, T. Moore, H. Szambolics, L. D. Buda-Prejbeanu, S. Auffret, B. Rodmacq, S. Pizzini, J. Vogel, M. Bonfim, A. Schuhl and G. Gaudin. Fast current-induced domain-wall motion controlled by the Rashba effect. *Nat Mater* **10**, 419 (2011).
- [55] C. O. Avci, K. Garello, I. M. Miron, G. Gaudin, S. Auffret, O. Boulle and P. Gambardella. Magnetization switching of an MgO/Co/Pt layer by in-plane current injection. *Applied Physics Letters* **100**, 212404 (2012).
- [56] K.-W. Kim, S.-M. Seo, J. Ryu, K.-J. Lee and H.-W. Lee. Magnetization dynamics induced by in-plane currents in ultrathin magnetic nanostructures with Rashba spin-orbit coupling. *Phys. Rev. B* **85**, 180404 (2012).
- [57] L. Liu, C.-F. Pai, Y. Li, H. W. Tseng, D. C. Ralph and R. A. Buhrman. Spin-torque switching with the giant spin Hall effect of tantalum. *Science* **336**, 555 (2012).
- [58] K. Ando, S. Takahashi, K. Harii, K. Sasage, J. Jeda, S. Maekawa and E. Saitoh. Electric manipulation of spin relaxation using the spin Hall effect. *Phys. Rev. Lett.* **101**, 036601 (2008).
- [59] J. Kim, J. Sinha, M. Hayashi, M. Yamanouchi, S. Fukami, T. Suzuki, S. Mitani and H. Ohno. Layer thickness dependence of the current-induced effective field vector in Ta|CoFeB|MgO. *Nat Mater* **12**, 240 (2013).
- [60] C. Kittel. *Introduction to solid state physics, 7th edition*. John Wiley & Sons, Ltd (1996).
- [61] M. D'Yakonov and V. Perel'. Current-induced spin orientation of electrons in semiconductors. *Physics Letters A* **35**, 459 (1971).
- [62] M. I. D'Yakonov and V. I. Perel'. Possibility of orienting electron spins with current. *Soviet Journal of Experimental and Theoretical Physics Letters* **13**, 467 (1971).

- [63] Y. Niimi, M. Morota, D. H. Wei, C. Deranlot, M. Basletic, A. Hamzic, A. Fert and Y. Otani. Extrinsic spin Hall effect induced by iridium impurities in copper. *Phys. Rev. Lett.* **106**, 126601 (2011).
- [64] Y. Niimi, Y. Kawanishi, D. H. Wei, C. Deranlot, H. X. Yang, M. Chshiev, T. Valet, A. Fert and Y. Otani. Giant spin Hall effect induced by skew scattering from bismuth impurities inside thin film CuBi alloys. *Phys. Rev. Lett.* **109**, 156602 (2012).
- [65] C.-F. Pai, L. Liu, Y. Li, H. W. Tseng, D. C. Ralph and R. A. Buhrman. Spin transfer torque devices utilizing the giant spin Hall effect of tungsten. *Applied Physics Letters* **101**, 122404 (2012).
- [66] X. Wang, J. Xiao, A. Manchon and S. Maekawa. Spin-Hall conductivity and electric polarization in metallic thin films. *Phys. Rev. B* **87**, 081407 (2013).
- [67] Y. Tserkovnyak, A. Brataas and G. E. W. Bauer. Enhanced Gilbert damping in thin ferromagnetic films. *Phys. Rev. Lett.* **88**, 117601 (2002).
- [68] B. Heinrich, D. Fraitová and V. Kamberský. The influence of s-d exchange on relaxation of magnons in metals. *physica status solidi (b)* **23**, 501 (1967).
- [69] M. Fähnle and C. Illg. Electron theory of fast and ultrafast dissipative magnetization dynamics. *Journal of Physics: Condensed Matter* **23**, 493201 (2011).
- [70] F. D. Czeschka. *Spin Currents in Metallic Nanostructures*. Ph.D. thesis, Walther-Meißner-Institut für Tieftemperaturforschung der Bayerischen Akademie der Wissenschaften (2011).
- [71] N. Viglin, V. Ustinov and V. Osipov. Spin injection maser. *JETP Letters* **86**, 193 (2007).
- [72] M. Holub and P. Bhattacharya. Spin-polarized light-emitting diodes and lasers. *Journal of Physics D: Applied Physics* **40**, R179 (2007).
- [73] S. M. Watts and B. J. van Wees. A solid state paramagnetic maser device driven by electron spin injection. *Phys. Rev. Lett.* **97**, 116601 (2006).
- [74] Y. G. Naidyuk, O. P. Balkashin, V. V. Fisun, I. K. Yanson, A. Kadigrobov, R. I. Shekhter, M. Jonson, V. Neu, M. Seifert, S. Andersson and V. Korenivski. Stimulated emission and absorption of photons in magnetic point contacts. *New Journal of Physics* **14**, 093021 (2012).
- [75] L. Berger. Generation of dc voltages by a magnetic multilayer undergoing ferromagnetic resonance. *Phys. Rev. B* **59**, 11465 (1999).
- [76] Y. V. Sharvin. A possible method for studying Fermi surfaces. *Sov. Phys.-JETP* **21**, 655 (1965). [*Zh. Eksp. Teor. Fiz.* **48**, 984-985 (1965)].
- [77] G. Deutscher. Andreev-Saint-James reflections: A probe of cuprate superconductors. *Rev. Mod. Phys.* **77**, 109 (2005).
- [78] D. Daghero and R. S. Gonnelli. Probing multiband superconductivity by point-contact spectroscopy. *Superconductor Science and Technology* **23**, 043001 (2010).

- [79] R. J. Soulen, J. M. Byers, M. S. Osofsky, B. Nadgorny, T. Ambrose, S. F. Cheng, P. R. Broussard, C. T. Tanaka, J. Nowak, J. S. Moodera, A. Barry and J. M. D. Coey. Measuring the spin polarization of a metal with a superconducting point contact. *Science* **282**, 85 (1998).
- [80] M. A. Reed, C. Zhou, C. J. Muller, T. P. Burgin and J. M. Tour. Conductance of a molecular junction. *Science* **278**, 252 (1997).
- [81] I. K. Yanson, Y. G. Naidyuk, D. L. Bashlakov, V. V. Fisun, O. P. Balkashin, V. Korenivski, A. Konovalenko and R. I. Shekhter. Spectroscopy of phonons and spin torques in magnetic point contacts. *Phys. Rev. Lett.* **95**, 186602 (2005).
- [82] J. R. Tucker and M. J. Feldman. Quantum detection at millimeter wavelengths. *Rev. Mod. Phys.* **57**, 1055 (1985).
- [83] I. K. Yanson. Nonlinear effects in the electric conductivity of point junctions and electron-phonon interaction in normal metals. *Zh. Eksp. Teor. Fiz.* **66**, 1035 (1974). [*Sov. Phys.-JETP* 39 (1974) 506–513].
- [84] A. G. M. Jansen, F. M. Mueller and P. Wyder. *Superconductivity in d- and f-band metals*. Plenum, New York (1976).
- [85] Y. J. Song, A. F. Otte, V. Shvarts, Z. Zhao, Y. Kuk, S. R. Blankenship, A. Band, F. M. Hess and J. A. Stroscio. Invited review article: A 10 mk scanning probe microscopy facility. *Review of Scientific Instruments* **81**, 121101 (2010).
- [86] K. Besocke. An easily operable scanning tunneling microscope. *Surface Science* **181**, 145 (1987).
- [87] J. Frohn, J. F. Wolf, K. Besocke and M. Teske. Coarse tip distance adjustment and positioner for a scanning tunneling microscope. *Review of Scientific Instruments* **60**, 1200 (1989).
- [88] S. H. Pan, E. W. Hudson and J. C. Davis.  $^3\text{He}$  refrigerator based very low temperature scanning tunneling microscope. *Review of Scientific Instruments* **70**, 1459 (1999).
- [89] attocube systems AG. [www.attocube.com](http://www.attocube.com).
- [90] Y. Uehara, T. Fujita, M. Iwami and S. Ushioda. Superconducting niobium tip for scanning tunneling microscope light emission spectroscopy. *Review of Scientific Instruments* **72**, 2097 (2001).
- [91] A. F. Otte. *Magnetism of a single atom*. Ph.D. thesis, Leiden University (2008).
- [92] Y. G. Naidyuk and I. K. Yanson. *Point-Contact Spectroscopy*. Springer (2005).
- [93] F. J. Cadieu. Selectively thermalized sputtering for the deposition of magnetic films with special anisotropes. *Journal of Vacuum Science & Technology A: Vacuum, Surfaces, and Films* **6**, 1668 (1988).
- [94] V. Neu and S. A. Shaheen. Sputtered Sm–Co films: Microstructure and magnetic properties. *Journal of Applied Physics* **86**, 7006 (1999).

- [95] R. Andreescu and M. J. O'Shea. Temperature dependence of coercivity and magnetic reversal in SmCo<sub>x</sub> thin films. *Journal of Applied Physics* **97**, 10F302 (2005).
- [96] T. Speliotis and D. Niarchos. Microstructure and magnetic properties of SmCo films. *J. Magn. Magn. Mater.* **290-291**, Part 2, 1195 (2005). Proceedings of the Joint European Magnetic Symposia (JEMS' 04).
- [97] E. E. Fullerton, C. H. Sowers, J. P. Pearson, S. D. Bader, X. Z. Wu and D. Lederman. A general approach to the epitaxial growth of rare-earth-transition-metal films. *Appl. Phys. Lett.* **69**, 2438 (1996).
- [98] L. Zhang, J. Hu, J. Chen and J. Ding. Nanostructured SmCo<sub>5</sub> thin films with perpendicular anisotropy formed in a wide range of Smco compositions. *Journal of Nanoscience and Nanotechnology* **11**, 2644 (2011).
- [99] L. N. Zhang, J. S. Chen, J. Ding and J. F. Hu. High-coercivity SmCo<sub>5</sub> thin films deposited on glass substrates. *J. Appl. Phys.* **103**, 113908 (2008).
- [100] Periodic report 3 : Fp7-fet-open : Stele : August 2012.
- [101] K. Buschow. Rare earth compounds. In E. Wohlfarth, editor, *Handbook of Ferromagnetic Materials*, volume Volume 1, pages 297–414. Elsevier (1980).
- [102] K. Strnat. Rare earth-cobalt permanent magnets. In E. Wohlfarth and K. Buschow, editors, *Handbook of Ferromagnetic Materials*, volume Volume 4, pages 131–209. Elsevier (1988).
- [103] K. Kumar. RETM<sub>5</sub> and RE<sub>2</sub>TM<sub>17</sub> permanent magnets development. *Journal of Applied Physics* **63**, R13 (1988).
- [104] K. Buschow and A. Van Der Goot. Intermetallic compounds in the system samarium-cobalt. *Journal of the Less Common Metals* **14**, 323 (1968).
- [105] Y. Khan. A contribution to the Sm-Co phase diagram. *Acta Crystallographica Section B* **30**, 861 (1974).
- [106] H. Okamoto. Co-Sm (cobalt-samarium). *Journal of Phase Equilibria* **20**, 535 (1999).
- [107] U. Varetto. Molekel 5.4.0. Swiss National Supercomputing Centre, Lugano (Switzerland).
- [108] Y. Khan. Variation of period with valence electron concentration in RT<sub>y</sub> one-dimensional long-period superstructures. *physica status solidi (a)* **23**, 425 (1974).
- [109] M. Q. Huang, W. E. Wallace, M. McHenry, Q. Chen and B. M. Ma. Structure and magnetic properties of SmCo<sub>7-x</sub>Zr<sub>x</sub> alloys (x = 0–0.8). *Journal of Applied Physics* **83**, 6718 (1998).
- [110] K. Strnat. The hard-magnetic properties of rare earth-transition metal alloys. *Magnetics, IEEE Transactions on* **8**, 511 (1972).
- [111] A. Singh, R. Tamm, V. Neu, S. Fahler, C.-G. Oertel, W. Skrotzki, L. Schultz and B. Holzapfel. Epitaxial growth of highly coercive Sm–Co thin films using pulsed laser deposition. *Journal of Applied Physics* **97**, 093902 (2005).

- [112] A. Singh, V. Neu, R. Tamm, K. Rao, S. Faehler, W. Skrotzki, L. Schultz and B. Holzapfel. Pulsed laser deposited epitaxial Sm–Co thin films with uniaxial magnetic texture. *Journal of Applied Physics* **99**, 08E917 (2006).
- [113] Y. D. Yao, Y. Liou, J. C. A. Huang, S. Y. Liao, I. Klik, W. T. Yang, C. P. Chang and C. K. Lo. Enhancement of magnetoresistance in Co(1 $\bar{1}$ 00)/Cr(211) bilayered films on MgO(110). *Journal of Applied Physics* **79**, 6533 (1996).
- [114] A. Singh, V. Neu, R. Tamm, K. S. Rao, S. Fähler, W. Skrotzki, L. Schultz and B. Holzapfel. Growth of epitaxial SmCo<sub>5</sub> films on Cr/MgO(100). *Appl. Phys. Lett.* **87**, 072505 (2005).
- [115] A. Singh, V. Neu, S. Fähler, L. Schultz and B. Holzapfel. Effect of composition on phase formation and magnetic properties of highly coercive Sm-Co films. *Journal of Magnetism and Magnetic Materials* **290-291**, Part 2, 1259 (2005). Proceedings of the Joint European Magnetic Symposia (JEMS' 04).
- [116] R. Tamm, K. S. Rao, S. Fähler, V. Neu, A. Singh, C.-G. Oertel, L. Schultz, B. Holzapfel and W. Skrotzki. Texture formation in epitaxial hard magnetic Sm<sub>2</sub>Co<sub>7</sub> thin films. *Phys. Status Solidi A* **207**, 106 (2010).
- [117] F. J. Cadieu, R. Rani, T. Theodoropoulos and L. Chen. Fully in plane aligned SmCo based films prepared by pulsed laser deposition. *Journal of Applied Physics* **85**, 5895 (1999).
- [118] G. Zangari, B. Lu, D. E. Laughlin and D. N. Lambeth. Structure and magnetic properties of SmCo thin films on Cr/Ag/Si templates. *Journal of Applied Physics* **85**, 5759 (1999).
- [119] L. Peng, H. Zhang, Q. Yang, Y. Li, Y. Song and J. Shen. Correlation between sputtering parameters and composition of SmCo-based films for microelectromechanical system applications. *Journal of Applied Physics* **105**, 063915 (2009).
- [120] J. Wang, M. Ghantasala and R. McLean. Bias sputtering effect on ultra-thin SmCo<sub>5</sub> films exhibiting large perpendicular coercivity. *Thin Solid Films* **517**, 656 (2008).
- [121] G. Xue, L. Peng and H. Zhang. Effect of sputtering parameters on film composition, crystal structure, and coercivity of SmCo based films deposited on Si (100) substrates. *Chinese Physics Letters* **27**, 017501 (2010).
- [122] F. J. Cadieu, H. Hegde and K. Chen. High-energy product Sm-Co-based sputtered films, crystal texturing, and magnetic properties. *Journal of Applied Physics* **67**, 4969 (1990).
- [123] A. Singh, V. Neu, S. Fähler, K. Nenkov, L. Schultz and B. Holzapfel. Mechanisms of coercivity in epitaxial smco<sub>5</sub> thin films. *Phys. Rev. B* **77**, 104443 (2008).
- [124] E. E. Fullerton, J. S. Jiang, C. Rehm, C. H. Sowers, S. D. Bader, J. B. Patel and X. Z. Wu. A general approach to the epitaxial growth of rare-earth-transition-metal films. *Appl. Phys. Lett.* **69**, 2438 (1996).
- [125] B. L. Gordon and M. S. Seehra. Magnetic susceptibility of Mn<sup>2+</sup> ions in MgO and evidence of clustering. *Phys. Rev. B* **40**, 2348 (1989).



- [126] J. van Wieringen and J. Rensen. Influence of lattice imperfections on the paramagnetic resonance of  $V^{2+}$  and  $Cr^{3+}$  in MgO. In W. Low, editor, *Paramagnetic resonance vol 1*, pages 105–112. Academic Press New York (1963).
- [127] M. Bartashevich, A. Andreev, E. Tarasov, T. Goto and M. Yamaguchi. Magnetic properties and spontaneous magnetostriction of a  $Sm_2Co_7$  single crystal. *Physica B* **183**, 369 (1993).
- [128] C. H. Chen, S. J. Knutson, Y. Shen, R. A. Wheeler, J. C. Horwath and P. N. Barnes. The effect of particle size on coercivity and crystallinity of  $SmCo_5$ . *Applied Physics Letters* **99**, 012504 (2011).
- [129] L. Zhang, J. Hu, J. Chen and J. Ding. Microstructure and magnetic properties studies of  $SmCo_5$  thin films grown on MgO and glass substrates. *Journal of Magnetism and Magnetic Materials* **321**, 2643 (2009).
- [130] S. Prucnal, A. Shalimov, M. Ozerov, K. Potzger and W. Skorupa. Magnetic and optical properties of virgin arc furnace grown MgO crystals. *J. Cryst. Growth* **339**, 70 (2012).
- [131] K. Baberschke. *Handbook of Magnetism and Advanced Magnetic Materials*, chapter Investigation of Ultrathin Ferromagnetic Films by Magnetic Resonance. John Wiley & Sons, Ltd (2007). ISBN 9780470022184.
- [132] M. Farle. Ferromagnetic resonance of ultrathin metallic layers. *Reports on Progress in Physics* **61**, 755 (1998).
- [133] J. Smit and H. G. Beljers. Ferromagnetic resonance absorption in  $BaFe_{12}O_{10}$ , a highly anisotropic crystal. *Philips Res. Rep.* **10**, 113 (1955).
- [134] H. Suhl. Ferromagnetic resonance in nickel ferrite between one and two kilomegacycles. *Phys. Rev.* **97**, 555 (1955).
- [135] J. Dubowik, K. Załęski, H. Głowiński and I. Gościńska. Angular dependence of ferromagnetic resonance linewidth in thin films. *Phys. Rev. B* **84**, 184438 (2011).
- [136] C. Chappert, K. L. Dang, P. Beauvillain, H. Hurdequint and D. Renard. Ferromagnetic resonance studies of very thin cobalt films on a gold substrate. *Phys. Rev. B* **34**, 3192 (1986).
- [137] W. Platow, A. N. Anisimov, G. L. Dunifer, M. Farle and K. Baberschke. Correlations between ferromagnetic-resonance linewidths and sample quality in the study of metallic ultrathin films. *Phys. Rev. B* **58**, 5611 (1998).
- [138] B. Heinrich, R. Urban and G. Woltersdorf. Magnetic relaxation in metallic films: Single and multilayer structures. *Journal of Applied Physics* **91**, 7523 (2002).
- [139] S. M. Bhagat and L. L. Hirst. Ferromagnetic resonance in nickel at low temperatures. *Phys. Rev.* **151**, 401 (1966).
- [140] S. M. Bhagat, J. R. Anderson and L. L. Hirst. Ferromagnetic resonance in pure iron at low temperatures. *Phys. Rev. Lett.* **16**, 1099 (1966).

- [141] J. N. Lloyd and S. Bhagat. Ferromagnetic resonance linewidths in Ni-Cu alloys. *Solid State Communications* **8**, 2029 (1970).
- [142] B. Heinrich, D. J. Meredith and J. F. Cochran. Wave number and temperature dependent Landau-Lifshitz damping in nickel. *Journal of Applied Physics* **50**, 7726 (1979).
- [143] S. Yakata, Y. Ando, T. Miyazaki and S. Mizukami. Temperature dependences of spin-diffusion lengths of Cu and Ru layers. *Japanese Journal of Applied Physics* **45**, 3892 (2006).
- [144] J. Kuneš and V. Kamberský. First-principles investigation of the damping of fast magnetization precession in ferromagnetic 3d metals. *Phys. Rev. B* **65**, 212411 (2002).
- [145] V. Kamberský. Spin-orbital Gilbert damping in common magnetic metals. *Phys. Rev. B* **76**, 134416 (2007).
- [146] K. Gilmore. *Precession damping in itinerant ferromagnets*. Ph.D. thesis, Montana state university (2007).
- [147] K. Gilmore, M. D. Stiles, J. Seib, D. Steiauf and M. Fähnle. Anisotropic damping of the magnetization dynamics in Ni, Co, and Fe. *Phys. Rev. B* **81**, 174414 (2010).
- [148] K. Gilmore, Y. U. Idzerda and M. D. Stiles. Identification of the dominant precession-damping mechanism in Fe, Co, and Ni by first-principles calculations. *Phys. Rev. Lett.* **99**, 027204 (2007).
- [149] J. Lindner, I. Barsukov, C. Raeder, C. Hassel, O. Posth, R. Meckenstock, P. Landeros and D. L. Mills. Two-magnon damping in thin films in case of canted magnetization: Theory versus experiment. *Phys. Rev. B* **80**, 224421 (2009).
- [150] C. P. Poole and H. A. Farach. *The theory of magnetic resonance*. Wiley-Interscience (New York) (1972).
- [151] C. Kittel. On the gyromagnetic ratio and spectroscopic splitting factor of ferromagnetic substances. *Phys. Rev.* **76**, 743 (1949).
- [152] Z. Zhang, P. E. Wigen and S. S. P. Parkin. Pt layer thickness dependence of magnetic properties in Co/Pt multilayers. *Journal of Applied Physics* **69**, 5649 (1991).
- [153] S. Mizukami, Y. Ando and T. Miyazaki. The study on ferromagnetic resonance linewidth for NM/80NiFe/NM (NM = Cu, Ta, Pd and Pt) films. *Japanese Journal of Applied Physics* **40**, 580 (2001).
- [154] O. Mosendz, J. E. Pearson, F. Y. Fradin, G. E. W. Bauer, S. D. Bader and A. Hoffmann. Quantifying spin Hall angles from spin pumping: Experiments and theory. *Phys. Rev. Lett.* **104**, 046601 (2010).
- [155] K. Ando, Y. Kajiwara, S. Takahashi, S. Maekawa, K. Takemoto, M. Takatsu and E. Saitoh. Angular dependence of inverse spin-Hall effect induced by spin pumping investigated in a Ni<sub>81</sub>Fe<sub>19</sub>/Pt thin film. *Phys. Rev. B* **78**, 014413 (2008).
- [156] H. Jiao and G. E. W. Bauer. Spin backflow and ac voltage generation by spin pumping and the inverse spin Hall effect. *Phys. Rev. Lett.* **110**, 217602 (2013).

- [157] L. Liu, R. A. Buhrman and D. C. Ralph. Review and analysis of measurements of the spin Hall effect in platinum. *ArXiv e-prints* (2011). 1111.3702.
- [158] M. T. Johnson, P. J. H. Bloemen, F. J. A. den Broeder and J. J. de Vries. Magnetic anisotropy in metallic multilayers. *Reports on Progress in Physics* **59**, 1409 (1996).
- [159] D. Bastian and E. Biller. Damping of ferromagnetic resonance in Ni-Fe alloys. *Physica status solidi (a)* **35**, 113 (1976).
- [160] C. Vittoria, S. D. Yoon and A. Widom. Relaxation mechanism for ordered magnetic materials. *Phys. Rev. B* **81**, 014412 (2010).
- [161] K. Fuchs and N. F. Mott. The conductivity of thin metallic films according to the electron theory of metals. *Proceedings of the Cambridge Philosophical Society* **34**, 100 (1938).
- [162] E. H. Sondheimer. The mean free path of electrons in metals. *Advances in Physics* **1**, 1 (1952).
- [163] J. Geissler, E. Goering, M. Justen, F. Weigand, G. Schütz, J. Langer, D. Schmitz, H. Maletta and R. Mattheis. Pt magnetization profile in a Pt/Co bilayer studied by resonant magnetic x-ray reflectometry. *Phys. Rev. B* **65**, 020405 (2001).
- [164] N. Nakajima, T. Koide, T. Shidara, H. Miyauchi, H. Fukutani, A. Fujimori, K. Iio, T. Katayama, M. Nývlt and Y. Suzuki. Perpendicular magnetic anisotropy caused by interfacial hybridization via enhanced orbital moment in Co/Pt multilayers: Magnetic circular X-ray dichroism study. *Phys. Rev. Lett.* **81**, 5229 (1998).
- [165] Z. S. Shan, J. X. Shen, R. D. Kirby, D. J. Sellmyer and Y. J. Wang. Temperature-dependent interface magnetism and magnetization reversal in Co/Pt multilayers. *Journal of Applied Physics* **75**, 6418 (1994).
- [166] A. A. Abrikosov and L. P. Gor'kov. *Zh. Eksp. Teor. Fiz.* **39**, 1781 (1960). [*Sov. Phys. JETP* **12** (1961) 1243].
- [167] C. H. Marrows and B. J. Hickey. Impurity scattering from  $\delta$ -layers in giant magnetoresistance systems. *Phys. Rev. B* **63**, 220405 (2001).
- [168] J.-G. Zhu, V. Sokalski, Y. Wang and D. Laughlin. Noise mechanisms in small grain size perpendicular thin film media. *Magnetics, IEEE Transactions on* **47**, 74 (2011).
- [169] K. Garello, I. M. Miron, C. O. Avci, F. Freimuth, Y. Mokrousov, S. Blugel, S. Auffret, O. Boulle, G. Gaudin and P. Gambardella. Symmetry and magnitude of spin-orbit torques in ferromagnetic heterostructures. *Nat Nano* **8**, 587 (2013).
- [170] A. D. Caviglia, M. Gabay, S. Gariglio, N. Reyren, C. Cancellieri and J.-M. Triscone. Tunable Rashba spin-orbit interaction at oxide interfaces. *Phys. Rev. Lett.* **104**, 126803 (2010).
- [171] S. Monso, B. Rodmacq, S. Auffret, G. Casali, F. Fettar, B. Gilles, B. Dieny and P. Boyer. Crossover from in-plane to perpendicular anisotropy in Pt/CoFe/AlO<sub>x</sub> sandwiches as a function of Al oxidation: A very accurate control of the oxidation of tunnel barriers. *Applied Physics Letters* **80**, 4157 (2002).

- [172] B. Rodmacq, S. Auffret, B. Dieny, S. Monso and P. Boyer. Crossovers from in-plane to perpendicular anisotropy in magnetic tunnel junctions as a function of the barrier degree of oxidation. *Journal of Applied Physics* **93**, 7513 (2003).
- [173] H. X. Yang, M. Chshiev, B. Dieny, J. H. Lee, A. Manchon and K. H. Shin. First-principles investigation of the very large perpendicular magnetic anisotropy at Fe|MgO and Co|MgO interfaces. *Phys. Rev. B* **84**, 054401 (2011).
- [174] M. Hayashi. Analytical expression for the harmonic Hall voltages in evaluating spin orbit torques. *ArXiv e-prints* (2013). 1307.5603.
- [175] K. Okamoto. A new method for analysis of magnetic anisotropy in films using the spontaneous Hall effect. *Journal of Magnetism and Magnetic Materials* **35**, 353 (1983).
- [176] U. H. Pi, K. W. Kim, J. Y. Bae, S. C. Lee, Y. J. Cho, K. S. Kim and S. Seo. Tilting of the spin orientation induced by Rashba effect in ferromagnetic metal layer. *Applied Physics Letters* **97**, 162507 (2010).
- [177] S. Emori, U. Bauer, S.-M. Ahn, E. Martinez and G. S. D. Beach. Current-driven dynamics of chiral ferromagnetic domain walls. *Nat Mater* **12**, 611 (2013).
- [178] K.-S. Ryu, L. Thomas, S.-H. Yang and S. Parkin. Chiral spin torque at magnetic domain walls. *Nat Nano* **8**, 527 (2013).
- [179] J.-H. Moon, S.-M. Seo, K.-J. Lee, K.-W. Kim, J. Ryu, H.-W. Lee, R. D. McMichael and M. D. Stiles. Spin-wave propagation in the presence of interfacial Dzyaloshinskii-Moriya interaction. *ArXiv e-prints* (2013). 1308.3341.
- [180] D. Cortés-Ortuño and P. Landeros. Influence of the Dzyaloshinskii-Moriya interaction on the spin-wave spectra of thin films. *Journal of Physics: Condensed Matter* **25**, 156001 (2013).
- [181] K. An, D. R. Birt, C.-F. Pai, K. Olsson, D. C. Ralph, R. A. Buhrman and X. Li. Control of propagating spin waves via spin transfer torque in a metallic bilayer waveguide. *ArXiv e-prints* (2013). 1308.6357.

# Summary

During the last 30 years, the number of both fundamental and applied studies of heterostructures of ferromagnets and normal metals has grown impressively. The attraction of studying these heterostructures lies in the fact that already at room temperature their charge transport properties can be strongly influenced by even small magnetic fields. This is nowadays applied in different integrated circuits like magnetic read heads for hard disks, magnetic memory and sensors.

Since the 1960s, studies in the field of semiconductor heterostructures showed that it is possible to fabricate light emitting devices (more specifically light emitting diodes, or LED's), which can emit visible, infrared and ultraviolet light. A LED consists of a semiconductor with an excess of electrons combined with a semiconductor with an excess of holes. When flowing a current through the semiconductor heterostructure, a non-equilibrium distribution of electrons and holes is created. Relaxation of this non-equilibrium state occurs by the recombination of an electron and a hole, whereby a photon is emitted.

Recently, it was proposed by Kadigrobov to combine both approaches and build a ferromagnetic LED, which has the special property that it can emit radiation within the so-called terahertz gap. The terahertz gap is the part of the electromagnetic spectrum between roughly 300 gigahertz and 30 terahertz, where it is very hard to generate radiation with conventional sources. In this PhD thesis we investigated the feasibility to build such a device.

In the ferromagnetic LED, it is not a non-equilibrium distribution of electrons and holes, but a non-equilibrium distribution of electrons with spin-up and spin-down which needs to be created. This distribution can relax by a spin-flip process and the emission of a photon. As we use a spin-flip process, the device can be called a spin-flip LED or laser. In **Chapter 1** and **Chapter 2**, the theory and recent developments in this field are described.

One way to create such a spin-flip laser is to inject a very high current density of electrons from a ferromagnet into a normal metal leading to a local excess of spin-up or spin-down electrons. When at the same time an external magnetic field is applied, with the field direction opposite to the magnetization of the ferromagnet, the injected spins are now in a non-equilibrium distribution. There is a finite probability that such spins relax by a spin-flip process where also a photon is emitted. In **Chapter 3** we describe point contact spectroscopy experiments which were meant as a first step to the final observation of radiation coming from the point contact. It did not prove possible, however, to observe signatures of the desired spin accumulation in the point contact.

The ferromagnet used in our spin-flip laser is  $\text{SmCo}_5$ , a hard ferromagnet with a very large coercive field. This is needed in order to allow the magnetic field to be opposite to the magnetization direction of the external magnetic field. In **Chapter 4**, we describe the sputter growth of thin films of Sm-Co. The thin films grown have a coercive field of approximately 3 T, although not all of them reach such large values. One of the main problems of growing Sm-Co films is the complexity of the phase diagram, which results in a large amount of different Sm-Co phases on the Co-rich side. Small variations in the Sm concentration results in a significant change of magnetic properties of the films.

One of the main problems of building a spin-flip laser is the issue of spin current injection and the relaxation of the spin current in an adjacent layer. In **Chapter 5** and **Chapter 6**, we use the ferromagnetic resonance technique (FMR) to study how the spin currents behave at the interface of a ferromagnet and a normal metal with large spin-orbit coupling, such as Pt or Pd. When spins are injected in such a metal, they are efficiently removed, which leads to a net spin current and is visible in the FMR spectrum as a broadening of the line. However, if a normal metal with a small spin-orbit coupling is used, as Cu or Al, the spins are removed less efficiently and almost no increase of the linewidth can be observed.

In **Chapter 5** we use FMR and electrical measurements to study spin current injection from thin Co films into a Pt capping layer. When varying the thickness of the Co layer and the angular dependence of the external magnetic field with respect to the normal of the thin film, we show that a spin current is indeed present. Next, we study the temperature dependence of the injection of this spin current. Going down in temperature we find that the basic injection efficiency does not change. The observed variation in FMR linewidth is due to changes in the intrinsic scattering mechanism in the ferromagnetic layer.

While studying the spin injection in Co/Pt sandwiches, also Co/Cu sandwiches were investigated for reference purposes. It was found that for very thin Co layers, the line broadening in Co/Cu is larger than could be expected, as Cu is a normal metal with weak spin-orbit coupling. In **Chapter 6** this system is studied in more detail. It is shown that measurements done on trilayers, where the ferromagnetic layer is covered on both sides with the normal metal, does not show this large broadening. The large difference between bilayers and trilayers shows that the extra broadening is a property of the bilayer, which we tentatively attribute to a Rashba spin-orbit torque, provided not by the interface between the ferromagnet and the normal metal, but by the interface between the ferromagnet and the substrate.





# Samenvatting

Gedurende de laatste dertig jaar is er een enorme toename geweest in fundamenteel en toegepast onderzoek naar zeer dunne gestapelde lagen van ferromagneten en normale metalen. Deze dunne lagen worden veelvuldig bestudeerd, omdat in deze systemen al bij kamertemperatuur grote veranderingen meetbaar zijn in de elektrische transporteigenschappen onder invloed van kleine magnetische velden. Dit wordt tegenwoordig toegepast in geïntegreerde schakelingen, zoals een magnetische uitleeskop van harde schijven, magnetisch geheugen en sensoren.

Sinds de jaren zestig heeft onderzoek in het veld van dunne gestapelde lagen van halfgeleiders laten zien, dat het mogelijk is structuren te creëren (licht-emitterende diodes of LEDs) die zichtbaar, infrarood of ultraviolet licht kunnen uitzenden. Een LED is een miniatuur schakeling waar een halfgeleider met een overschot aan elektronen is gecombineerd met een halfgeleider met een overschot aan gaten. Door hier een stroom door te sturen, ontstaat een niet-evenwichtsverdeling van de elektronen en gaten. Relaxatie van deze niet-evenwichts toestand vindt plaats door recombinatie van een elektron en een gat, waarbij een foton wordt uitgezonden.

Recent heeft Kadigrobov voorgesteld om bovenstaande twee ontwikkelingen te combineren en een ferromagnetische LED te bouwen, die als eigenschap heeft dat het ook straling kan uitzenden in het zogenaamde terahertz-gat. Het terahertz-gat is het deel van het elektromagnetische spectrum van 300 gigahertz tot ongeveer 30 terahertz, waarin het met bestaande technieken zeer lastig is om straling te genereren. In dit proefschrift wordt onderzocht of het mogelijk is om zo'n schakeling te bouwen.

In de ferromagnetische LED brengen we geen niet-evenwichtsverdeling van elektronen en gaten, maar een niet-evenwichtsverdeling van elektronen met spin-*op* en spin-*neer*. Deze verdeling kan relaxeren

door het omdraaien of flippen van de spin en het uitzenden van een foton. Deze schakeling kan dan ook een spin-flip LED of laser genoemd worden. In **hoofdstuk 1** en **hoofdstuk 2** worden de theorie en recente ontwikkelingen in dit veld beschreven.

Een manier om een spin-flip laser te maken is door middel van het injecteren van een hele hoge stroomdichtheid van elektronen vanuit een ferromagneet in een normaal metaal. Als er nu ook een extern magneetveld wordt ingeschakeld, waarvan de veldrichting tegenovergesteld is aan de richting van de magnetisatie van de ferromagneet, dan bevinden de spins zich in een niet-evenwichtsverdeling. Er is een kans dat er spins relaxeren door middel van het uitzenden van een foton. In **hoofdstuk 3** worden een aantal puntcontact-spectroscopie experimenten beschreven, die uitgevoerd zijn als de eerste stappen voor het waarnemen van straling die in het puntcontact gegenereerd wordt. Experimenteel bleek het echter niet mogelijk te zijn om signalen van de gewenste spin ophoping te zien in het puntcontact.

De ferromagneet die gebruikt is bij de spin-flip laser experimenten is

$\text{SmCo}_5$ , een harde ferromagneet met een groot coërcief veld. Dit is nodig omdat het externe magnetische veld tegen de magnetisatie van de ferromagneet in staat. In hoofdstuk 4 beschrijven we hoe we dunne lagen van de Sm-Co ferromagneet groeien. De dunne lagen die voor dit proefschrift gegroeid zijn, hebben een coërcief veld van ongeveer 3 T, hoewel niet alle films zo'n grote waarde halen. De groei van goede dunne lagen wordt bemoeilijkt door de grote hoeveelheid verschillende Sm-Co fases die zich bevinden in de buurt van de  $\text{SmCo}_5$  fase, die allemaal net wat andere magnetische eigenschappen hebben. Een kleine variatie in de Sm concentratie leidt al tot een significante verandering van de magnetische eigenschappen van de dunne lagen.

Een van de grootste problemen bij het bouwen van een spin-flip laser is de injectie van de spinstroom in een aanliggende dunne laag, en de relaxatie van de spinstroom in de aanliggende laag. In **hoofdstuk 5** en **hoofdstuk 6** onderzoeken we met behulp van de ferromagnetische resonantie techniek (FMR) hoe deze spinstromen zich gedragen op een interface tussen een ferromagneet en een normaal metaal met een grote spin-baan koppeling, zoals Pt en Pd. Wanneer er een spins worden geïnjecteerd in zo'n normaal metaal wordt de spinstroom efficiënt verwijderd; dit leidt tot een netto spinstroom die zichtbaar is in het FMR spectrum als een verbreding van de lijn. Wordt er echter een normaal metaal met een kleine spin-baan koppeling gebruikt, zoals Cu of Al, dan worden de spins veel minder efficiënt verwijderd en is er nauwelijks verbreding zichtbaar in het FMR spectrum.

In **hoofdstuk 5** gebruiken we FMR en elektrische metingen om de injectie van een spinstroom te bestuderen van dunne Co lagen in de aanliggende Pt laag. Met behulp van de dikte afhankelijkheid van de ferromagneet en de hoek-afhankelijkheid van het externe magnetische veld ten opzichte van de normaal van de dunne lagen, wordt er aangetoond dat er inderdaad een spinstroom aanwezig is. Wij hebben ook de temperatuur afhankelijkheid van de injectie van een spinstroom bestudeerd. We vinden dat wanneer de temperatuur wordt verlaagd, de efficiëntie van de spinstroom injectie niet verandert. De waargenomen verandering van de FMR lijnbreedte wordt blijkbaar veroorzaakt door een verandering in de intrinsieke verstrooiings mechanisme in de ferromagnetische laag.

Bij het bestuderen van de spinstroom injectie in dunne Co/Pt dubbel lagen, zijn daarnaast ook dunne Co/Cu lagen bestudeerd als referentie monsters. Voor heel dunne Co lagen vonden we dat de lijnverbreding veel groter is dan voor Cu, een normaal metaal met een zwakke spin-baan koppeling, verwacht kon worden. In **hoofdstuk 6** bestuderen we deze systemen in meer detail. Metingen aan drielagen, waar de ferromagneet aan beide zijden is bedekt met een normale metaallaag, laten geen extra lijnverbreding zien. Het grote verschil tussen de dubbellaag en drielagen geeft aan dat de extra demping een eigenschap van de dubbellaag is. Wij denken hierbij aan een Rashba spin-baan koppeling die niet wordt veroorzaakt bij het grensvlak tussen de ferromagneet en het normale metaal, maar aan het grensvlak van de ferromagneet en het substraat.



# Curriculum Vitae

**Timotheus Guillaume Albertus Verhagen**

26 - 2 - 1985 Born in Roosendaal en Nispen, The Netherlands

## **Education**

2003 - 2007 B.Sc Applied Physics  
Delft University of Technology, The Netherlands

2007 - 2009 M.Sc Applied Physics  
Delft University of Technology, The Netherlands

2009 - 2013 Ph.D. research  
Leiden University, The Netherlands  
Supervisors: Prof. dr. J. Aarts and Prof. dr. J. M. van Ruitenbeek

11-2013 - Postdoctoral research  
Fyzikální ústav Akademie ved Česká republika



# Publications

1. I. T. M. Usman, K. A. Yates, J. D. Moore, K. Morrison, V. K. Pecharsky, K. A. Gschneidner, T. Verhagen, J. Aarts, V. I. Zverev, J. W. A. Robinson, J. D. S. Witt, M. G. Blamire, and L. F. Cohen, *Evidence for spin mixing in holmium thin film and crystal samples*, Physical Review B **83**, 144518 (2011).
2. N. Vercruyssen, T. G. A. Verhagen, M. G. Flokstra, J. P. Pekola, and T. M. Klapwijk, *Evanescent states and nonequilibrium in driven superconducting nanowires*, Physical Review B **85**, 224503 (2012).
3. E. Tartaglioni, T. G. A. Verhagen, F. Galli, M. L. Trouwborst, R. Müller, T. Shiota, J. Aarts and J. M. van Ruitenbeek, *New directions in point-contact spectroscopy based on scanning tunneling microscopy techniques*, Fizika Nizkikh Temperatur **39** 249-260 (2013).
4. T. G. A. Verhagen, D. B. Boltje, J. M. van Ruitenbeek, J. Aarts, *Sputter gas pressure effects on the properties of Sm-Co thin films deposited from a single target*, arXiv:1210.2240 (2012).
5. P. G. van Rhee, P. Zijlstra, T. G. A. Verhagen, J. Aarts, M. I. Katsnelson, J. C. Maan, M. Orrit, and P. C. M. Christianen, *Giant magnetic susceptibility of gold nanorods detected by magnetic alignment* Physical Review Letters **111**, 127202 (2013).





# Acknowledgments

Bijna op het einde van dit proefschrift, of voor vele het begin, wil ik alle collega's en studenten van LION en partners van het STELE project bedanken die op een of andere manier bijgedragen hebben aan dit proefschrift. In het bijzonder wil ik de volgende personen noemen.

Voor de punt contact experimenten waren de inserts ontwikkeld door Simon Kelly en Christiaan Pen, de electronica door Bert Crama, en was de experimentele hulp van Sven Visser, Stefano Voltan en Yurii Naidyuk onmisbaar.

De  $\text{SmCo}_5$  dunne lagen zouden zonder bijdragen van Daan Boltje aan de sample karakterisatie, de X-ray sample houder van Arjen Geluk en de zeldzame-aarde kennis van Klára Uhlířová nooit zulke goede eigenschappen gehad hebben.

Voor de introductie in ferromagnetische resonantie (FMR) en elektronspinresonantie, het maken en doormeten van de enorme hoeveelheid FMR samples, de interpretatie van de data en de ontwikkeling van sample houders voor de FMR metingen ben ik veelvuldig uitstekend geholpen door Gé van Albada, Martina Huber, Martin van Son, Peter Gast, Jos Disselhorst, Bert Crama, Christiaan Pen, Hiske Overweg, Inge Leermakers, Lennart de Bruin en vooral Holly Tinkey.

Mijn begeleiders Jan Aarts en Jan van Ruitenbeek, die mij 4 jaar lang alle ruimte en vrijheid hebben gegeven om dit onderzoek uit te voeren en behulpzaam waren bij het inbouwen van de spin-pomp back-up route.

En als laatste de mensen die misschien wel het allerbelangrijkste zijn geweest de afgelopen 4 jaar; mijn familie, volleybalvrienden, amateursterrenkundevrienden en studievrienden. Bedankt voor alles!